Characterisation of host-guest complexes of supramolecular self-assembled cages using EPR spectroscopy

James Daniel Nicholas

MSc by Research

University of York

Chemistry

December 2018

Abstract

Supramolecular self-assembled cages are interesting and useful structures that have a variety of different potential applications including catalysis, reaction control, and chemical transport and storage. It is therefore important to understand in detail how guest molecules interact with these cage structures and determine the characteristics of the host-guest complexes formed in order to develop these cages and their uses further. Previous studies into supramolecular assemblies such as cucurbiturils, cyclodextrins and resorcinarene capsules have demonstrated that EPR spectroscopy is particularly suitable for characterisation of the host-guest complexes of these structures with paramagnetic radical probes as guests, and this work aimed to extend these studies to cage structures.

In this thesis, a number of different radical probes were investigated qualitatively with host cage structures of the form $[M_8L_{12}][X]_{16}$, M = Cd or Co, L = $C_{28}H_{22}N_6$ and X = ClO_4 or Cl, comparing EPR spectra of radical in neat solvent to radical+cage solution to identify if binding had occurred. Competing guest molecules were used to confirm binding effects by displacing the radical probes and observing the effect on the EPR spectrum.

Three nitroxide radical guests were identified for detailed binding studies: 4-oxo-TEMPO, 4-carboxy-TEMPO and 3-carboxy-PROXYL, and titrations of solutions of guest with cage solution were carried out. Simulations of the EPR spectra revealed the contributions of two components, bound and unbound radical, to the radical@cage complex spectra, allowing characteristics of the complex to be determined. The ratio between bound and unbound component allowed calculation of association constants for the complexes, whilst comparison between bound and unbound rotational diffusion rates showed that binding of radical led to restricted motion of the probe, and hence slower tumbling rates. Finally, changes in the hyperfine values were used to determine changes in the polarity of the environment of the radical.

Contents

List of figures

List of schemes

List of tables

List of equations

Acknowledgements

Firstly, I would like to thank my supervisor, Dr Victor Chechik for his guidance, support and advice during the course of my MSc project, and for giving me the opportunity to research with the group.

I'd also like to thank the whole of the VC group for their help and friendship, especially Jonathan and Peter for putting up with my questions, helping me out and making it an enjoyable year.

Special thanks goes to Will and Pete for giving me a place to stay whilst I finished off lab work and started writing up.

I'd also like to thank the whole E002 office/E014 lab for making the place such a pleasant place to work and spend the past year.

Thank you also to my family and friends for their support, especially my parents Angela and Christian, and my brothers Thomas, Mark and Christopher for being supportive throughout, and a special thanks to Olivia for always being there for me.

Author's Declaration

I declare that this thesis is a presentation of original work and I am the sole author. This work has not previously been presented for an award at this, or any other, University. All sources are acknowledged as References.

1 Introduction

1.1 Development of supramolecular structures

The synthesis and characterisation of supramolecular assemblies has been an area of great interest over the past few decades with many different groups working on the development of new structures and investigating their properties and potential applications. In 2016, the Nobel Prize in Chemistry was awarded to Sauvage,[1,2] Stoddart[3,4] and Feringa[5,6] "for the design and synthesis of molecular machines", demonstrating the importance and relevance of self-assembly and supramolecular structures in the chemical field. Self-assembled cages are an equally important development, with many useful applications being investigated, including transport and storage of molecules – for example dangerous or drug-like molecules – as well as the use of cages to enable catalysis or control reaction dynamics through host-guest interactions. Examples of many of these potential uses will be explored in this introduction, alongside discussion of the design, synthesis and characterisation of the structures, and investigation of host-guest complexes that they may form.

Some of the first self-assembled structures of particular relevance and interest to this project were first reported in 1997 by Caulder and Raymond who described the synthesis and characterisation of helical structures that are self-assembled when bis(catecholamide) ligands are reacted with [M(acac)$_3$] compounds in the presence of KOH in methanol.[7] The structure of the ligands is shown in Figure 1 and the general reaction scheme for the formation of the helices is shown in Scheme 1.

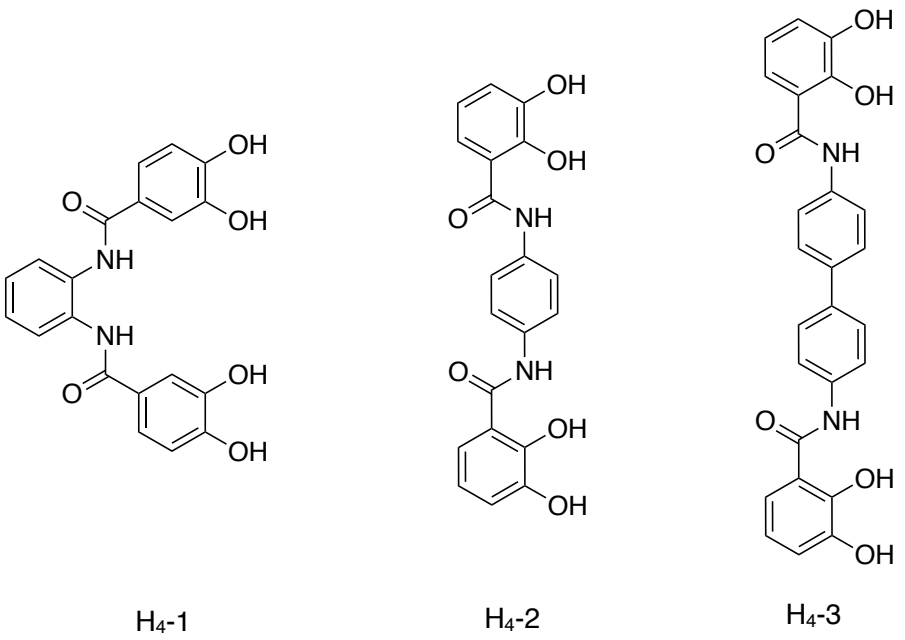

Figure 1 - Structures of the three bis(catecholamide) ligands, H_4-1, H_4-2 and H_4-3 used for synthesis of helices by Caulder and Raymond.[7]

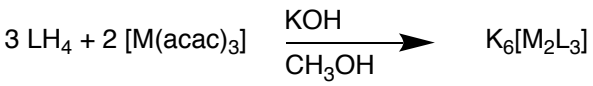

Scheme 1 - General reaction scheme for synthesis of the helices by Caulder and Raymond.[7]

These supramolecular helices were an important development, showing how using specific, suitably designed ligands, and choosing metals which would form strong metal-ligand interactions with them, could lead reproducibly to formation of a distinct supramolecular structure. Using ligands of a similar nature, the studies were extended to cages formed of bis- and tris(catecholamide) ligands, with metal ions such as Fe(III), Ti(IV) and Sn(IV) at the cage vertices.[8] This led to a demonstration of how mass spectrometry could be used to characterise the cage structures.[9] The $[Ti_4L_4]^{8-}$ cluster (synthesis and structure shown in Figure 2) gives 4 peaks in the negative ESI mass spectrum corresponding to multiply charged structures of the form $\{[Ti_4L_4]^{8-} . (8\text{-}X)H^+\}^{X-}$, X= 1-4, whilst in the positive ESI a total of 11 singly and multiply charged structures are seen, with appropriate numbers of associated H^+ and Na^+ ions.

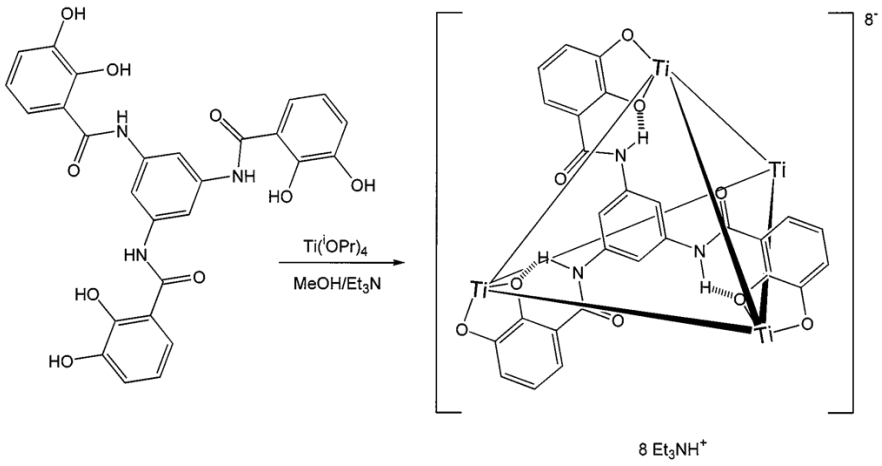

Figure 2: Synthesis and structure of $[Ti_4L_4]^{8-}$ structure. Reproduced from reference.[9]

It is beneficial to use mass spectrometry as a technique for characterisation of cage structures in this way, as it provides another solution state characterisation option that can confirm stability of the cage structure, demonstrated by the lack of fragmentation of the cage itself. It can also provide support for observed X-ray crystallographic structures, or be used as an alternative, albeit less detailed, structure confirmation if X-ray quality single crystals cannot be formed.

This cage structure demonstrates the use of "face-directed self-assembly" as described by Seidel and Stang,[10] where the linker molecule forms the faces of the polyhedral cage structure, and the resultant combination of these 'face-fragments' leads to the formation of the whole cage structure.

In contrast to this, in 2003, Ward and co-workers explored the reaction of a flexible bis-bidentate ligand (general structure shown in Figure 3) with pyrazolyl-pyridine terminal groups together with Co(II) and Zn(II) salts to yield a complex of the form M_8L_{12},[11] following on from tetrahedral M_2L_3 and M_4L_6 complexes that were synthesised using a similar ligand in 1998.[12]

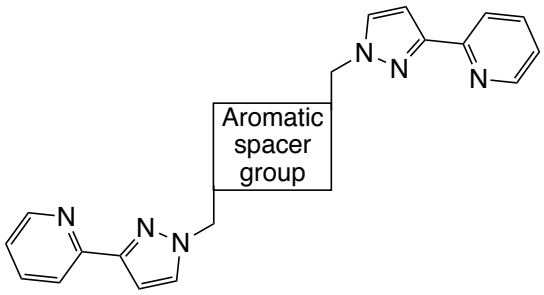

Figure 3: General structure of the ligands used by Ward and co-workers.

This work demonstrates the use of "edge-directed self-assembly", as the linker molecules join with the metal atoms to form fragments that combine to become the edges of the cage structures. The flexible nature of the ligands means that in contrast to the work of Caulder and Raymond, and others using more rigid ligands, the conformations and shapes of the structures formed were not predesigned, and instead could only be confirmed after synthesis.

Mass spectrometry was again used to confirm the structures, although this time in positive ion mode, with loss of BF_4^- anions leading to successive peaks in the spectrum corresponding to multiply charged cage structures that result from this loss. The group investigated the effects that different structures of similar ligands had on the stability of a cage structure, noting that, for example, a ligand with a naphthalene spacer produced a cage that is indefinitely stable in polar solvents, compared to a cage synthesised using a ligand with an anthracene spacer, which was observed to dissociate in the same solvents. This indicates that the greater amount of π-stacking present in the naphthalene-ligand cage gives it greater structural integrity and is likely part of the driving force for its formation from the subcomponents.

The work has also more recently been extended to investigate the same structure with Fe(II) metal vertices by Li et al.[13] to study the spin-crossover behaviour of the cage, using similar methods as described above to confirm successful synthesis.

Meanwhile, Nitschke and co-workers reported the synthesis of a new tetrahedral metal-organic cage complex in 2008.[14] This structure forms through reaction of 4,4'-diamonobiphenyl-2.2'-disulfonic acid and 2-formylpyridine with iron(II) in a basic aqueous solution, as shown in Figure 4.

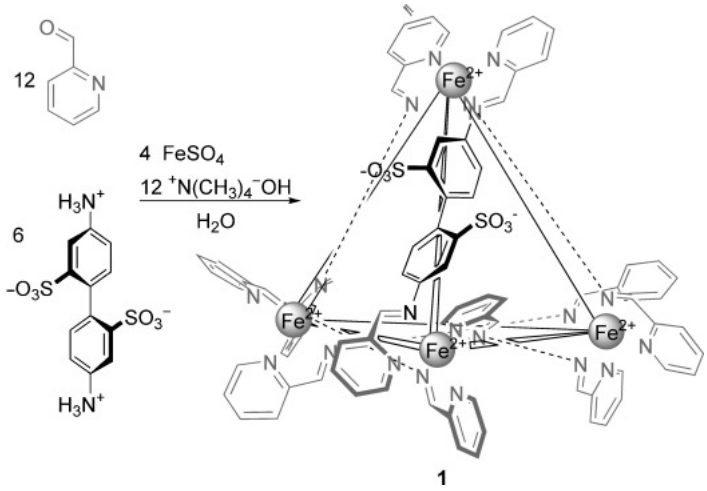

Figure 4 - Preparation of the tetrahedral M_4L_6 cage reported by Nitschke and co-workers. Reproduced from reference.[14]

They further developed this work in 2013,[15] by additionally using the transition metals Co and Ni, to increase the cavity size of the cage, due to the increased metal-ligand bond lengths and more flexible coordination sphere. The group confirm successful synthesis of the cage structures again using mass spectrometry, observing peaks for the $[M_4L_6]^{4-}$ species for Co and Ni. Investigations were also carried out using bis(pyridylimine) ligands, with metals Fe, Co and Cd, to examine the possibility of synthesising asymmetric M_4L_6 tetrahedral cages.[16] Investigations into the guest binding abilities of these cages are described in Section 1.2.1.

In later work, Nitschke et al. demonstrate the ability to control the solubility of the cage structures using anion exchange techniques.[17] Here they describe replacing less hydrophilic trifluoromethanesulfonate anions, associated with hydrophobic cages, with more hydrophilic sulfate anions, which led to the cage structure becoming soluble in water. Ward et al. also used a similar process with their cage structures, replacing BF_4^- anions with Cl^- anions to yield a water soluble form of their cage structure,[18] which previously had only been soluble in organic solvent, unless the ligand was modified as described below (Section 1.2.1).

The work of Fujita et al. is also significant in the field of supramolecular cages, as they have aimed to develop larger and larger supramolecular structures, reporting, in 2016, the synthesis of an $M_{30}L_{60}$ molecular icosidodecahedron[19] with an interior cavity size of 157,000 Å^3. This follows on from their successful syntheses of an M_6L_{12} octahedron[20], an $M_{12}L_{24}$ cuboctahedron[21] and an $M_{24}L_{48}$ rhombicuboctahedron.[22] All of these structures have the general formula M_nL_{2n} and use Pd^{2+} ions at the vertices but contain ligands which have been carefully altered between structures – specifically altering the ligand bend angles - within this M_nL_{2n} series to allow the formation of progressively larger structures. Some of these structures are shown in Figure 5.

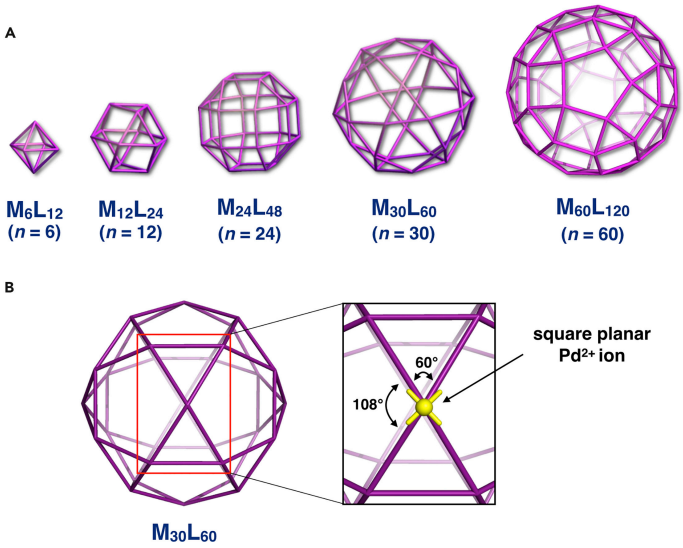

Figure 5 - Schematic representations of the M_nL_{2n} assemblies synthesised by Fujita and co-workers. Reproduced from reference.[19]

This clearly highlights the capabilities of self-assembly of components into well-defined supramolecular structures and emphasises the importance that careful ligand design plays in forming these structures, and the ability to predict the possible structures given knowledge of the metal ion used and its coordination properties.

1.2 Previous binding studies with supramolecular structures

Once supramolecular structures have been assembled, a logical progression in the investigation is to study how guest molecules bind to the structure to form host-guest complexes, allowing understanding of the binding mechanisms and providing insight into potential uses of the cage structures. The ability of a cage to selectively bind and release molecules upon change of external stimuli for example could be a useful feature for protecting and delivering drug-like molecules to their intended destination within the body, or could be useful for controlling reaction dynamics, binding a reactant to prevent reactivity, and then subsequently releasing it to allow the reaction to proceed.[23]

There are many examples of studies that investigate these complexes, and a number of techniques are employed, the most common being NMR spectroscopy. However, whilst appearing to be relatively uncommon for supramolecular cage structures specifically, there has been a variety of other supramolecular assemblies that have been investigated using EPR spectroscopy.

1.2.1 Investigating host-guest binding and catalysis applications using NMR spectroscopy

In their work, Caulder and Raymond investigated the binding of guests inside a gallium tetrahedral cluster with the form M_4L_6 using NMR spectroscopy.[24] They found that this cage structure shows a preferential binding for Et_4N^+ over Me_4N^+ or Pr_4N^+, demonstrating how supramolecular assemblies can be used to selectively encapsulate specific guests. Equilibrium constants were calculated by comparing NMR spectra of different host-guest complexes. The ability to calculate these constants quantitatively show the power of the NMR monitoring technique, allowing better characterisation of the cage binding properties in a quantitative way.

NMR titrations were used by Ward and co-workers with the cage structures mentioned above to investigate guest binding,[25] using the paramagnetic nature of the cobalt cage to their advantage. The presence of the paramagnetic cobalt introduces an additional magnetic field contribution that the sample experiences, due to the magnetic anisotropy of the paramagnetic centre, and this results in what is known as a pseudocontact shift effect. This effect causes the signals in the NMR spectrum to be shifted, and in this case has the effect of separating out the signals. This enables changes in the NMR spectrum, upon addition of guest molecule, to be seen more clearly, allowing the binding constants of the different guests to be determined quantitatively through NMR titrations.[26] The group also investigated alteration of the ligand through functionalisation, to allow the M_8L_{12} cage structure to become soluble in water, in order to investigate how guest binding was dictated by hydrophobic and solvent effects.[27] They found that whilst the dominant binding force for the MeCN-soluble cage was the H-bond acceptor nature of the guest, allowing strong interactions between the guest and H-bond donor sites of the internal cavity of the cage, for the H_2O-soluble cage, the driving force for binding was the hydrophobic nature of the cavity, and the desolvation energy released when the guest was bound inside the cage and removed from the free solution. These studies into host-guest binding with the cage structure led to investigations into the catalytic possibilities of the cage, and it was demonstrated that binding of benzisoxazole inside the cage allowed efficient catalysis of the Kemp elimination due to accumulation of hydroxide anions around the highly positively charged cage.[27,28] The scheme for the catalysis is shown in Figure 6.

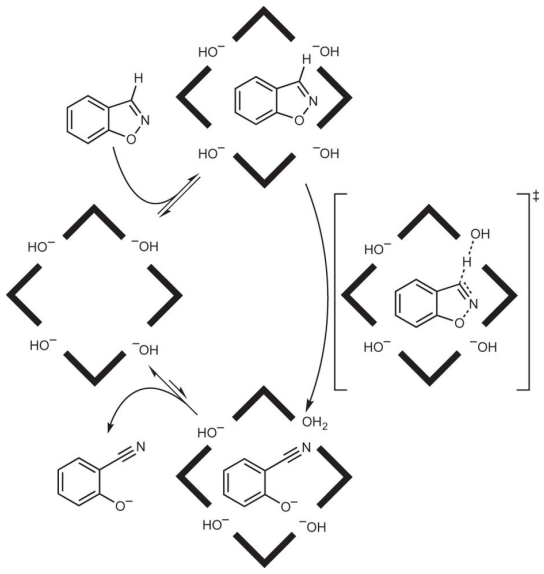

Figure 6 - Diagram showing the catalysis of the Kemp elimination reaction, enabled by binding of hydrophobic benzisoxazole inside the cage, reduction due to the close proximity of the hydroxide anions, and release of the newly formed more hydrophilic, and therefore less strongly bound, guest. Reproduced from reference.[28]

This work of Nitschke and co-workers is interesting as it again shows the possibility of selective guest binding based upon cage structure, this time with the cage described in Section 1.1 showing preference for binding hydrophobic guest molecules such as cyclohexane or cyclopentane, whilst showing no binding for alcohols or organic cations of sizes similar to the hydrocarbon guests. This highlights the importance that chemical properties play on encapsulation inside a cage, confirming it is not just dependent on guest size. The work also demonstrates the reversibility of this binding, since the cage can be opened and the guest recovered; either through an imine exchange reaction, or by changing the pH of the complex solution by addition of acid. The group went on to demonstrate the usefulness of this cage as a container molecule by incorporating P_4 as a guest, showing that it could be made air-stable and water-soluble as a result.[29] They demonstrate in a 2012 paper[30] how the cage may be used to control Diels-Alder reactivity by encapsulating the furan reactant, and controlling its release by adding a competing benzene guest, thus allowing control over the reaction by separating the reagents from each other, as shown in Scheme 2.

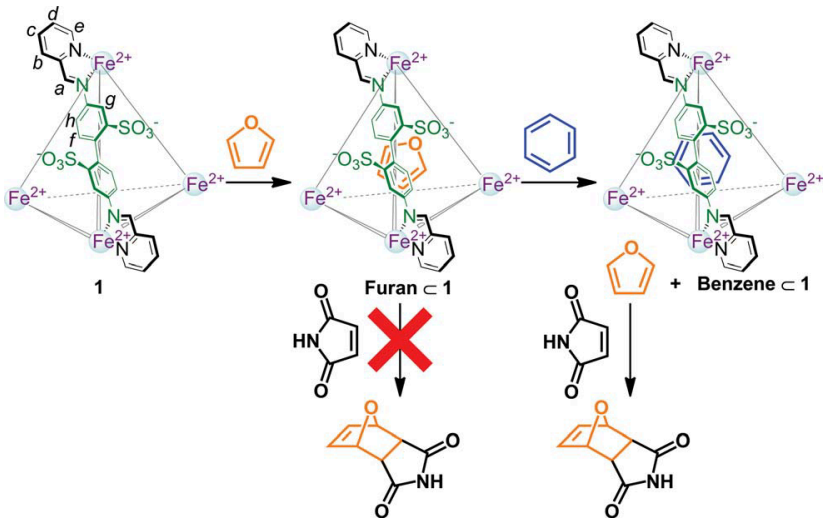

Scheme 2 - Schematic representation of the binding of furan inside the cage structure, preventing reaction with maleimide, and subsequent release upon addition of benzene as competing guest, allowing the reaction to proceed. Reproduced from reference[30] with permission from The Royal Society of Chemistry.

With a change in metal from Fe to Co, the group observed the ability to bind guests up to 30 % larger than previously possible, demonstrating how host characteristics could be altered to change the environment.[15] As before, these binding studies were monitored using NMR spectroscopy, where new signals appearing in the NMR spectra of the cage structures could be assigned to the guest@host structures, and if no changed was observed, encapsulation of the guest was presumed to not have occurred.

1.2.2 Investigating host-guest binding using EPR spectroscopy

As noted, EPR spectroscopy (a theoretical explanation of the technique is given in Section 1.3) has not been widely used to study cages structures specifically, likely due to the necessity for paramagnetic species to be present, requiring either stable radical guests to be used, or for the metal ions in the cage structures to be in a suitable oxidation state. The latter approach has limitations, as it is likely that the resulting EPR spectra from paramagnetic cage structure will either be complex and difficult to simulate, due to multiple metal environments within the structure, or that the spectra will be too broad, such that any changes upon addition of non-radical guest may not be distinguishable. However, the former approach has been used to good effect with several different supramolecular assemblies, as described below, thanks to a number of parameters which may reveal information about the binding of radicals in these host-guest complexes.

1.2.2.1 Effect of binding on hyperfine splitting

The sensitivity of EPR spectroscopy of nitroxide radicals to the polarity of the local environment is a useful feature of the technique, making it easy to study binding by observing

how the hyperfine splitting in the spectrum changes, as a measure of the change in polarity of the environment around the radical. This is due to the change in distribution of charge density in the N-O group, the effect of which is described in Section 1.3.2. This effect is demonstrated well by Mezzina et al.[31] who used EPR spectroscopy to study the host-guest complexes of cucurbit[7]uril (**CB7**) with the radicals benzyl *tert*-butyl nitroxide (**BTBN**) and **TEMPO** (Figure 7).

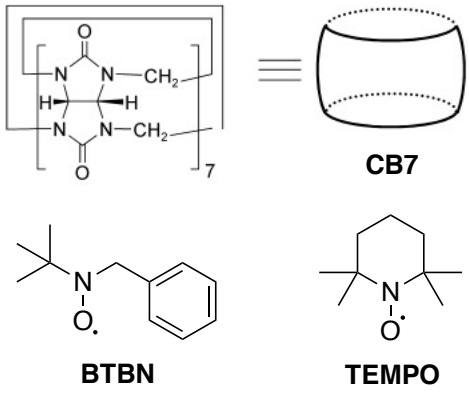

*Figure 7 - Diagram showing a representation of the cucurbit[7]uril (**CB7**) structure and the radical guests benzyl tert-butyl nitroxide (**BTBN**) and **TEMPO** studied by Mezzina et al. Adapted from reference.[31]*

In this paper the EPR spectra of both BTBN and TEMPO were shown to change upon addition of **CB7**, with the change in hyperfine splitting apparent in the spectrum, indicating that a change in polarity between bound and unbound radical was present. The spectra for these host-guest complexes are shown in Figure 8.

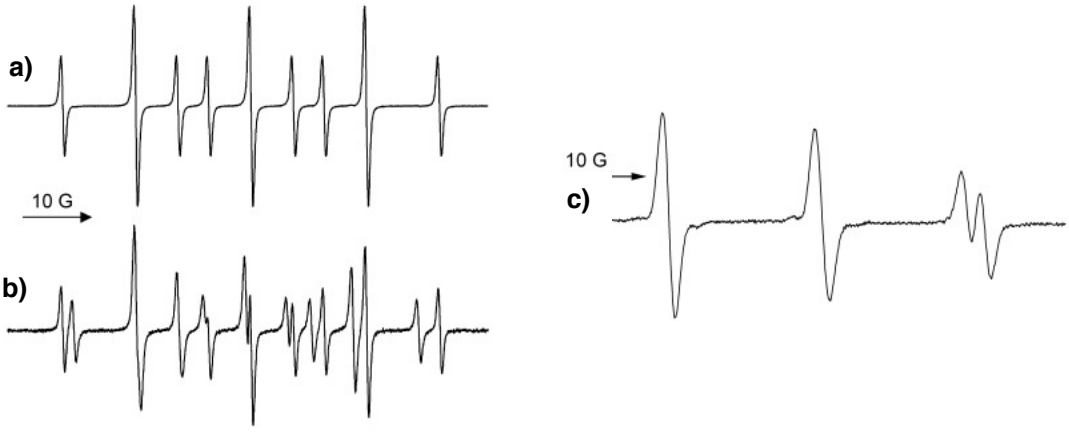

*Figure 8 - EPR spectra of a) **BTBN** b) **BTBN**+**CB7** c) **TEMPO**+**CB7** all recorded in water at 298 K. Reproduced from reference.[31]*

A similar effect was observed by Ionita et al.[32,33] investigating the host-guest complexes of cyclodextrins, in papers reporting room temperature solution studies and low temperature frozen and viscous solution studies of these complexes.

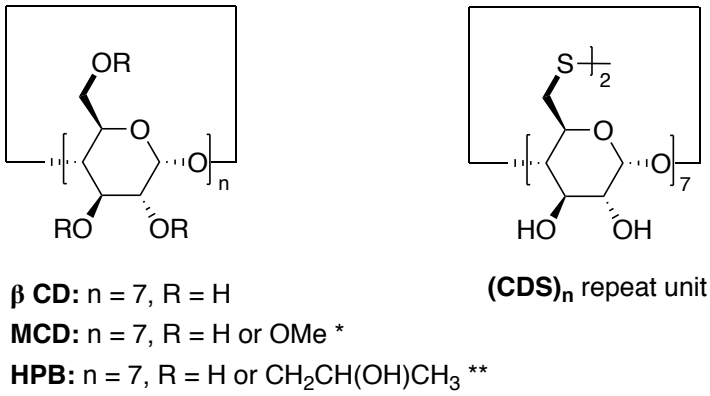

*Figure 9 - Structures of the functionalised cyclodextrins (CDs), **β-CD**, hydroxypropyl-β-CD (**HPB**), methyl β-CD (**MCD**) and polymeric β-CD-based, disulfide-crosslinked nanocapsules **(CDS)n** studied by Ionita et al.[32] *(Avg. M_W =1310) ***(Avg. M_W =1460)*

These studies built on previous work by Kotake and Janzen,[34,35] and found that binding of the guests to the hosts leads to decreased hyperfine constants due to a more hydrophobic environment around the radical. The effects for TEMPO with the various cyclodextrins are shown in Figure 10, and illustrate that the effect of binding on the hyperfine splitting is less pronounced than for the studies with **CB7**.

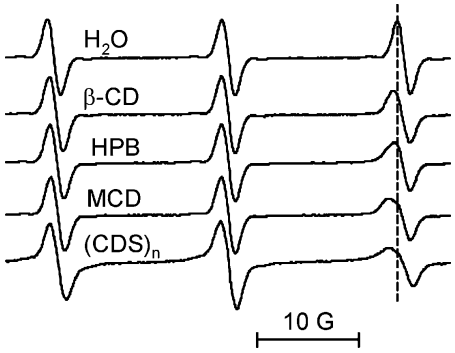

*Figure 10 - EPR spectra of TEMPO in neat H_2O and with cyclodextrin (**CD**) guests showing how the hyperfine splitting changes for the radical bound to the **CD** guests. Reproduced from reference.[32]*

Changes in hyperfine splitting were also observed in studies by Ayhan et al. in 2015.[36] into host-guest complexes of a water-soluble resorcinarene capsule, first developed by Rebek and co-workers,[37] with different nitroxides as guests, shown in Figure 11.

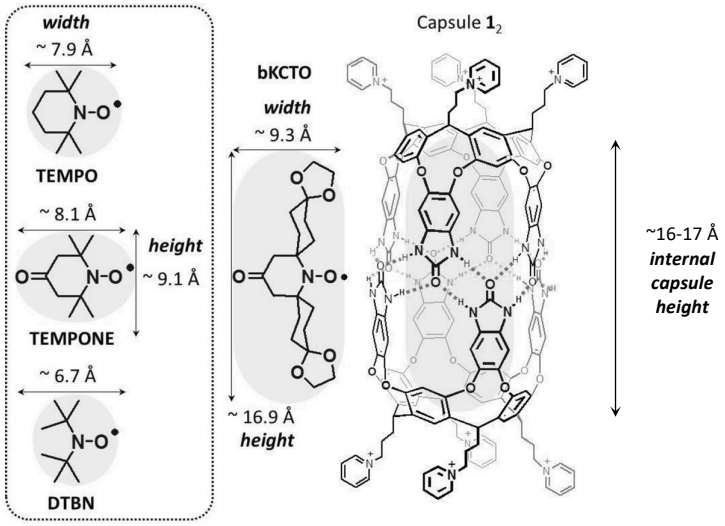

Figure 11 - Structures of some of the nitroxide radical guests and the resorcinarene capsule used by Ayhan et al. Reproduced from reference.[36]

Their work shows that binding is possible in two ways with this structure, either 1:1 host:guest, where host is the cavitand, or 2:1 host:guest where host is the cavitand H-bonded to another cavitand to form the capsule shown in Figure 11. Binding of di-*tert*-butyl nitroxide (DTBN) in the capsule led to changes in the hyperfine splitting constants due to change in polarity inside the capsule compared to DTBN in neat solvent. This is contrasted with their investigations with 4-hydroxy-TEMPO, 3-carboxy-PROXYL and 4-amino-TEMPO, which show no significant change in the EPR spectrum upon addition of the resorcinarene capsule, likely due to the presence of highly polar groups on the nitroxides which prevent binding.

Studies by Garel et al.[38] also identified changes in hyperfine splittings for four TEMPO derivatives, shown in Figure 12, with a water-soluble cryptophane structure shown in Figure 13.

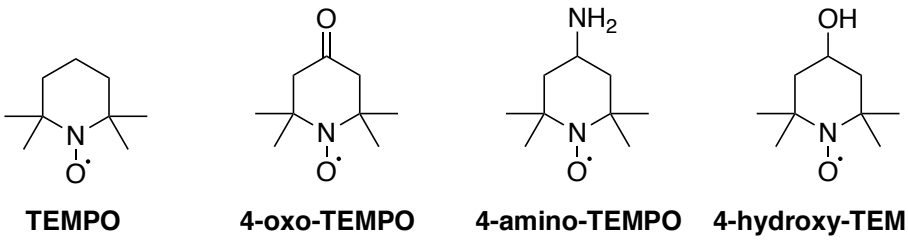

Figure 12 - Four TEMPO derivatives studied by Garel et al. as guests for the host cryptophane structure. L-R: TEMPO, 4-oxo-TEMPO, 4-amino-TEMPO, 4-hydroxy-TEMPO.

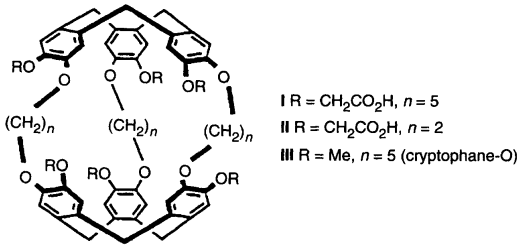

Figure 13 - Structure of the cryptophane studied by Garel et al. Adapted from reference[38] with permission from The Royal Society of Chemistry.

The hyperfine splittings observed for the radicals bound inside the cavity were smaller than those of the radicals in H_2O solution, due to the decreased polarity of the cavity. Comparison of the splitting values obtained to those of the radicals in other neat solvents revealed that the cavity had a polarity similar to bulk chloroform or dichloromethane.

1.2.2.2 Effect of binding on tumbling rate and exchange dynamics

EPR spectroscopy is not only sensitive to changes in polarity, but also to the rotational motion of the radical probe, and hence can provide good evidence of binding or inclusion in a host cavity when the rotational parameters for radical@host are compared to that of unbound radical. This is due to the anisotropic nature of the EPR parameters as described below in Section 1.3.4.

The cryptophane developed by Garel et al. was found to restrict the motion of the radicals investigated by factors of between 16 and 20, when compared to the tumbling rates in free solution. The effects of this restricted motion are visible in the spectra for **TEMPO**@cryptophane and **4-oxo-TEMPO**@cryptophane, shown in Figure 14.

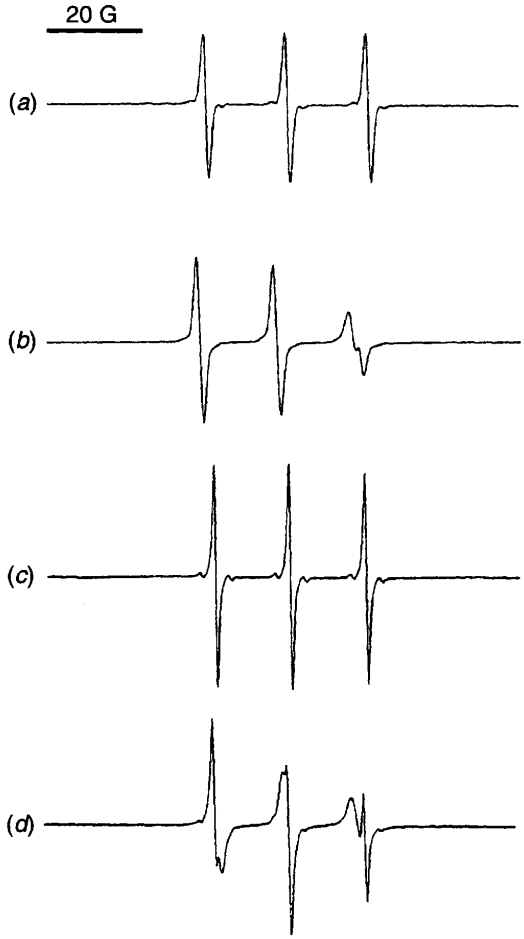

Figure 14 - EPR spectra of: a) 5×10^{-4} M TEMPO and b) in the presence of 5×10^{-4} M cryptophane; c) 5×10^{-4} M 4-oxo-TEMPO and d) in the presence of 5×10^{-4} M cryptophane. Reproduced from reference[38] with permission from The Royal Society of Chemistry.

The studies by Ionita et al. described in the previous section also found that binding of the radicals to the **CD** restricted their motion. They describe how functionalisation of the **CD** with groups that slow down tumbling rate of the whole complex allows accurate simulation and determination of the tumbling rate of the guest inside the cavity, as the tumbling effects of the host are effectively removed, in contrast to studies using unfunctionalised **CD**s. This is necessary due to the relatively small size of the **CD** structures in contrast to the larger sizes of other supramolecular assemblies like the cryptophanes, which means that tumbling of the unfunctionalised **CD** will not be slow on the EPR timescale. In addition to these findings, the low temperature studies reveal that in viscous aqueous glycerol solutions, the **TEMPO** radical spin probes tumble faster inside the host cavity than in the free solution. This is attributed to the increasing viscosity of the solution outside the cavity, which restricts motion of the radicals, whilst the inside of the cavity does not experience this increase in viscosity, and hence the radical may continue to tumble more freely.

Whilst broadening of the EPR spectrum will occur due to decreased tumbling, the spectrum may also be broadened due to exchange between the bound and unbound radical guests. In

previous work by Lucarini et al.[39] with cyclodextrins (**CD**s) and **BTBN**, they found that line broadenings observed were due to an exchange time similar to that of the EPR timescale, in contrast to the work described above for **BTBN** with **CB7** which shows that exchange between bound and unbound guest is slow on the EPR timescale as the radical remains bound for >10 μs, and thus line broadening does not result as a consequence of this exchange.

1.2.2.3 Determination of binding constants

In a similar way to NMR characterisation of host-guest complexes, EPR spectroscopy may provide an alternative option for calculating binding strength of guests to the host structure. In NMR characterisation this is achieved by observing the appearance of additional peaks in the spectrum as a solution of guest molecule is titrated with a solution of host structure, and the intensity of the peaks used to determine concentrations and hence calculating association constants as described above. In EPR spectroscopy, radical guest molecule solutions are titrated against a solution of host molecule, but instead of change in host spectrum being observed, a change in the guest EPR spectrum is observed, comparing that of guest@host to free guest in neat solvent. The spectrum obtained for guest@host is a combination of two components, one from bound radical guest and one from unbound guest, provided dynamic exchange of the guest from its bound to unbound state is slow on the EPR timescale. By simulating the spectra, the weighting of these components may be obtained, and related to the concentration of the components in the sample, and hence association constant may be calculated.

This technique is used by Ayhan et al. to calculate the binding constants for the radical guests inside the cavitand and capsule studied in their work, with values of the order ~10^3 M^{-1} obtained for 1:1 radical@cavitand binding, and values ~10^7 M^{-2} obtained for the 1:2 radical@capsule complexes. By comparing the different binding constants, the most stable complexes could be determined, providing useful information for future studies with the structure.

Similar methods were used by Ionita et al. to calculate the binding constants for the nitroxide guests studied in their work with CDs, finding that TEMPO itself formed relatively weak binding with the structure, as did the DOXYL spin probes used, but that amphiphilic probes with TEMPO units at the head were bound strongly, suggesting that in the latter case, it was the hydrophobic chain group that was being bound to the cavity of the CD. Alongside the small changes in other parameters like the hyperfine splitting values for the amphiphilic probes in this work, compared to larger changes for the TEMPO and DOXYL probes, this enabled confident characterisation of the different binding sites of the radical probes, demonstrating

the usefulness of the technique, but also the importance of all of the parameters contributing to a full understanding of radical@host binding.

1.2.2.4 Using binding to study spin-spin interactions

One example where radical guests were used to investigate a supramolecular cage structure is reported in papers by Fujita and co-workers[40,41] the structure of which is illustrated in Figure 15, alongside the structures of the radicals.

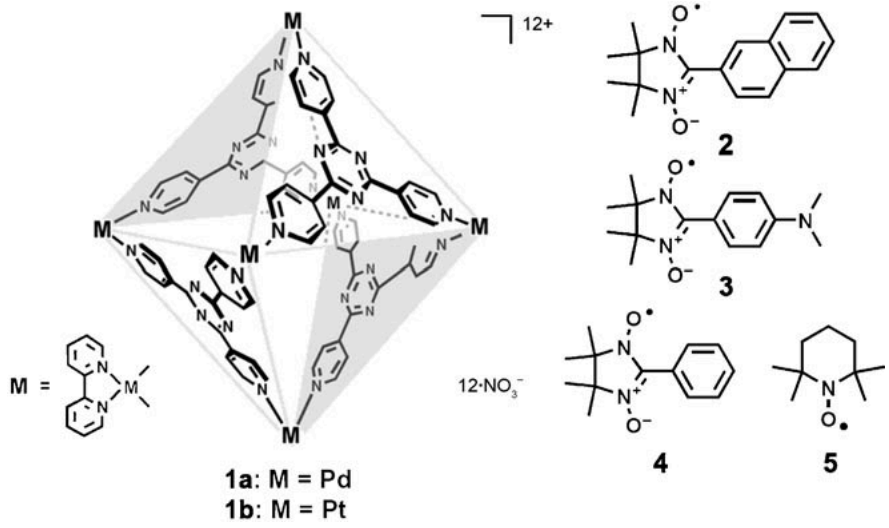

Figure 15 – Structure of the cage synthesised by Fujita and co-workers, and the radicals investigated. Reproduced from reference.[40]

In this study intermolecular through-space spin-spin interactions between the radical species are observed, resulting from the encapsulation of two radicals in close proximity inside the cage. This is in contrast to the radical in solution, for which no interactions between molecules are observed. This provides information about the position of the guests inside the cage, and how they arranged as part of the host-guest complex. They also show how the interaction may be manipulated through both thermal and pH control, in a reversible way, demonstrating the control that may be achieved in guest binding interactions.

1.3 Electron paramagnetic resonance theory

Electron paramagnetic resonance (EPR) spectroscopy is a magnetic resonance technique used to study systems containing unpaired electrons by observing the transition between the two electron spin states that is induced by the absorption of the applied electromagnetic radiation – in this case microwave radiation.

Electrons may be characterised by their spin angular momentum S = ½, and spin magnetic quantum number $m_s = \pm ½$. The two possible spin states are defined as 'spin-up' ($m_s = + ½$) or

'spin-down' ($m_s = -½$), and in the absence of any external magnetic field, these two spin states have the same energy, and are therefore degenerate. However, if an external magnetic field is applied, this degeneracy is removed due to the Zeeman effect. This effect arises since the electrons have their own magnetic moment which will align either parallel or antiparallel to an external magnetic field, splitting the two energy levels of the electron, known as the *electron Zeeman levels*, and leading to loss of degeneracy of the spin states. The energy of these states may be defined by Equation 1, where g_e is the free-electron g-factor ($g_e = 2.0023$), μ_B is the Bohr magneton, and B is the is the magnetic field strength of the applied magnetic field.

$$E = g_e m_s \mu_B B$$

Equation 1 - Energy of electron states

The effect of the splitting by an external magnetic field is shown in Figure 16.

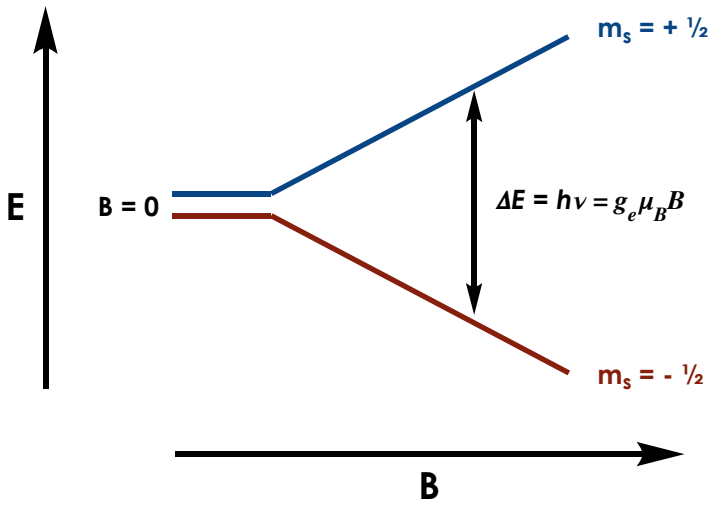

Figure 16 - Diagram showing the splitting of the two electron Zeeman levels in the presence of an external magnetic field due to the Zeeman effect.

Upon application of electromagnetic radiation with an energy ΔE, the sample will absorb the radiation, and an electron in the lower state will be excited to the upper state. In an EPR experiment, the applied electromagnetic radiation will be microwave radiation, typically 9.5 GHz for X band. Whilst the microwave frequency is kept constant, the magnetic field is swept. The absorption of the microwave energy may then be recorded by the EPR spectrometer to give the signals in the spectra. In continuous wave (CW) mode, the EPR spectra are recorded and presented in first derivative mode.

1.3.1 *g*-values

Although the electron will experience the external magnetic field B, the environment around the electron will also have local magnetic fields, and as such, the electron will experience an *effective magnetic field*, which may be defined as $B_{eff} = B + B_{local}$. However, since it is possible to measure B easily, g_e is replaced by an *effective g-factor*, and instead B_{eff} may be defined as $B_{eff} = (g/g_e)B$. The g-value may then be obtained for a signal in the spectrum by either direct measurement or by referencing to a known standard. The g-value is an important parameter in EPR spectroscopy, as it may provide information about the exact chemical environment of the electron, and is therefore sensitive to any changes in environment that may occur, for example when comparing bound and unbound radical guest.

1.3.2 Nuclear spin and hyperfine interactions

Additional splittings are observed in EPR spectra as a result of interactions between nuclei with spin angular momentum where $I \neq 0$ (for example ^{1}H, ^{13}C or ^{14}N) and the external magnetic field, leading to nuclear Zeeman interaction. The effect of the nuclear Zeeman is similar to the electron Zeeman effect, in that the external magnetic field introduces degeneracy between energy states, this time defined by the magnetic quantum number, m_I, where m_I may take values -I, -I+1… I-1, I. In addition to this, there is an interaction between the unpaired electron and the $I \neq 0$ nucleus, known as the hyperfine interaction. The splitting pattern due to hyperfine interactions may be defined by the formula 2nI+1 where n is the number of equivalent nuclei with spin angular momentum I. The hyperfine interaction causes a perturbation of the nuclear Zeeman levels, either raising or lowering them in energy slightly. The energy of the levels may then be defined by Equation 2.

$$E = g_e m_s \mu_B B - g_N m_I \mu_N B + a m_s m_I$$

Equation 2 - Energy of the electron states, including the contributions from electron Zeeman splitting, nuclear Zeeman splitting and hyperfine interactions.

In the case of a nitroxide, significant hyperfine coupling will be observed between the unpaired electron and the ^{14}N nucleus with a spin angular momentum I = 1, leading to the energy levels shown in Figure 17.

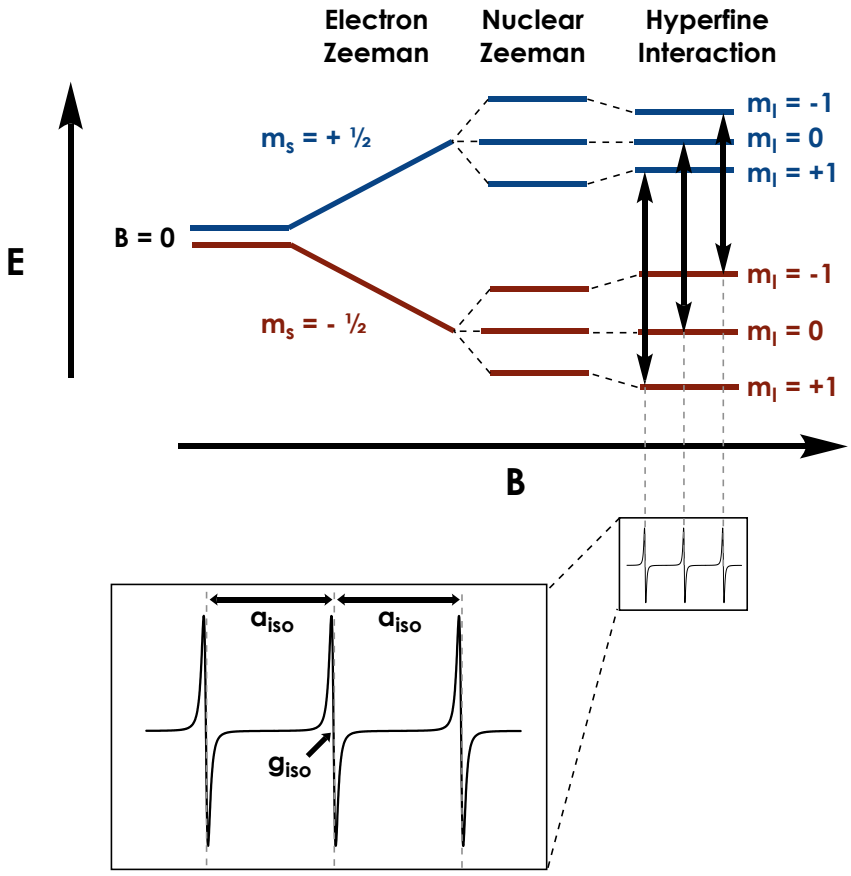

Figure 17 - Diagram showing splitting of the energy levels due to the effects of nuclear Zeeman splitting and the hyperfine interaction between the electron and an I = 1 nucleus (e.g. ^{14}N) in the presence of an external magnetic field B, in addition to the splitting due to the electronic Zeeman effect. An isotropic nitroxide EPR spectrum is shown below, with the signals in the spectrum assigned to the each of the three transitions. The positions of g_{iso} and a_{iso} are indicated on the enlarged spectrum.

Due to the selection rules for the transitions, $\Delta m_s = \pm 1$ and $\Delta m_I = 0$, only three transitions are allowed, and so the EPR spectrum is expected to have three signals, as expected based upon the 2nI+1 rule.

These hyperfine interactions are another important parameter in EPR spectroscopy as the interaction is very sensitive to the environment of the unpaired electron and the $I \neq 0$ nucleus, with variations expected due to conformational changes, as well as changes in solvent polarity for example, which in nitroxides can change the charge density distribution on the N-O bond, and hence influence the hyperfine interaction between the unpaired electron on the oxygen atom and the ^{14}N nucleus.[42–46]

1.3.3 Line broadening of EPR spectra

In theory, EPR spectra resulting from these absorptions should contain lines which are infinitely sharp. However, this is not the case, as there are a number of different effects which may broaden the signal either homogeneously or inhomogeneously. Homogenous broadening is caused by effects such as spin-spin interactions, or Heisenberg exchange and leads to

Lorentzian broadening of the signal. Inhomogeneous broadening is caused by effects such as unresolved hyperfine structures, non-uniformities in the magnetic field or dipolar interactions between unlike spins, and leads to Gaussian broadening of the signal, which results due to the individual resonant lines arising from these effects combining into a single broadening envelope.[47] The different lineshapes are shown for the first derivative and absorption form in Figure 18.

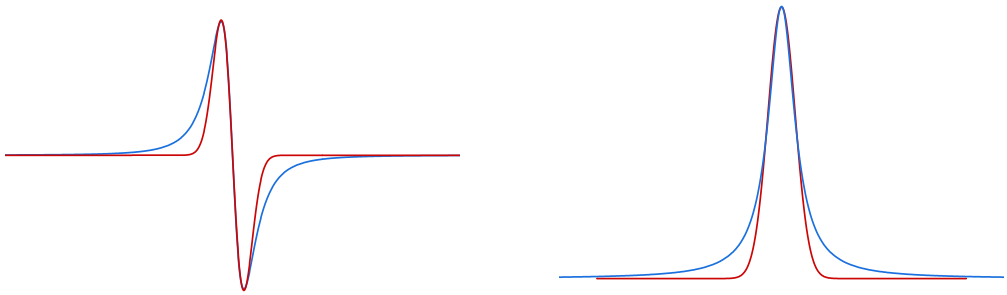

Figure 18 - First derivative lines (left) and absorption lines (right) for Lorentzian (blue) and Gaussian (red) functions. The lines have the same peak-to-peak linewidth.

In most cases, both of these types of broadening are present, and so the resulting broadening is the convolution of the two, and may be considered Voigtian. The degree of broadening present, as well as the ratio between the two types, can provide useful information about the environment of the radical and the system it is in. However, the broadening of the signal may also introduce difficulties in characterising the spectra, as if many factors are contributing to broadening, it may not be possible to accurately model the system in simulations, as the contributions from each effect may not be able to be distinguished from one another.

1.3.4 Rotational effects: anisotropy in EPR spectra

For continuous wave (CW) EPR spectroscopy, four dynamic regimes may be defined: isotropic limit, fast motion regime, slow motion regime, and rigid limit. These regimes are dependent on the rotational motion of the paramagnetic species, defined by the rotational correlation time, τ_c / s, or rotational diffusion rate, D / s^{-1}, where $\tau_c = 1/(6D)$. The difference in the regimes may be defined by comparing the correlation time to the spectral anisotropy, $\Delta\omega$, which is a measure of the difference in resonance frequencies for the different molecular orientations.

Both the g- and A-values are inherently anisotropic, and dependent on the orientation of the molecule. However, if the rate of tumbling is much faster than the difference in resonance frequencies, all of the contributions will be averaged out, and an isotropic spectrum will be obtained. This corresponds to $\tau_c < 10^{-9}\ s$ or $D > 1.6 \times 10^{8}\ s^{-1}$ in general for a nitroxide

radical. In neat solvents such as H_2O and MeCN it would be expected that the diffusion rate will be sufficiently large that the spectra will be isotropic. The lines in an EPR spectrum for a sample in the isotropic limit will typically be sharp and narrow.

As the tumbling rate begins to approach the $\Delta\omega$ value, the fast-motion regime is entered. Here, the lines in the spectrum will be broadened slightly, and this broadening is dependent on the nuclear magnetic quantum number m_I. As a result, each line in a nitroxide spectrum for example will be broadened to different degrees, with the high-field line experiencing a greater degree of broadening.

However, if the rate of tumbling is similar to, or smaller than, the resonance frequency difference, the slow-motion regime will be encountered. This may be as a result of a more viscous solvent being used, for example an aqueous glycerol solution, or more relevant to this work, if binding to another structure is taking place. The slow-motion tumbling rate leads to broadening of the lines in the spectrum, as the contributions from molecules in different orientations throughout the sample are no longer averaged out. The rotation of the molecule may also be restricted or preferred in one axis than in others, and this can also lead to changes in the lineshape.

A general example of the change in lineshape for a nitroxide radical EPR spectrum in each of these dynamic regimes is demonstrated clearly in a diagram produced by Stoll and Schweiger[48], reproduced in Figure 19.

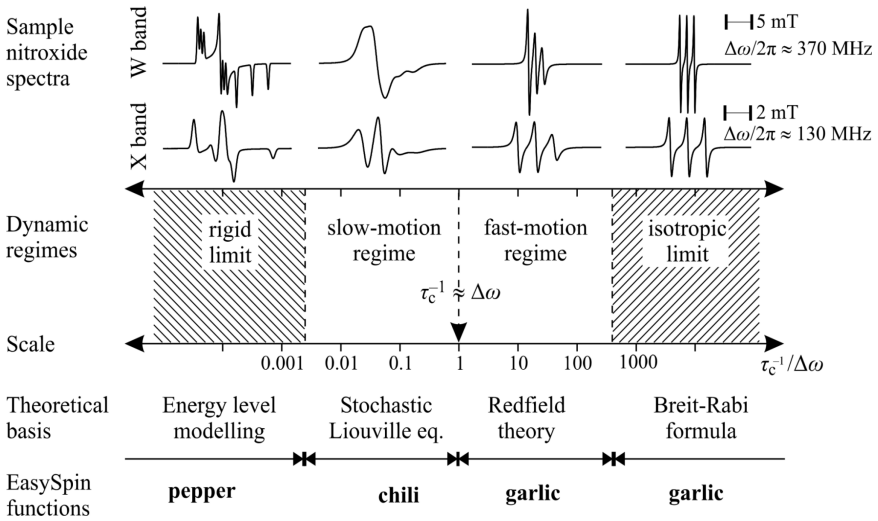

Figure 19 - Diagram showing the different dynamic regimes of EPR spectroscopy and sample EPR spectra for each regime. The diagram also shows the theoretical basis and EasySpin function used for each regime. Reproduced from reference.[48]

In order to extract information about the molecular motion and rotational diffusion rates, it is usually necessary to simulate the spectra, and depending on the regime in which the radical is

in, different theoretical bases and simulation functions may be used. When using EasySpin[49] isotropic and fast-motion spectra may be simulated using the *garlic* function, whilst the slow-motion regime requires using the *chili* function.

The *garlic* function uses Redfield theory[50] to simulate the spectra, where the effects of the anisotropy due to the tumbling are treated as a small perturbation, and can be described by a quadratic formula of the form:

$$\Delta B = A + B \cdot m_I + C \cdot m_I^2$$

Where ΔB is the perturbation in the linewidth due to the anisotropy, dependent on the parameters A, B and C, and m_I, the nuclear magnetic quantum number. The parameters A, B and C are linearly dependent on the correlation time, τ_c, and the anisotropic hyperfine and g tensors.[51]

In the slow-motion regime, the anisotropic effects can no longer be treated a small perturbation, and so the *chili* function uses the Stochastic Liouville equation to simulate spectra:

$$\frac{\partial}{\partial t}\rho(\boldsymbol{\Omega}, t) = -i\big[H\big((\boldsymbol{\Omega}, t)\big), \rho(\boldsymbol{\Omega}, t)\big] - \Gamma_{\boldsymbol{\Omega}}[\rho(\boldsymbol{\Omega}, t) - \rho_0(\boldsymbol{\Omega})]$$

Where ρ is the density matrix described by the spin Hamiltonian H and the diffusion superoperator $\Gamma_{\boldsymbol{\Omega}}$, and ρ_0 is the matrix at thermal equilibrium. The diffusion superoperator used is dependent on the model used for rotational diffusion, most commonly this is rotational Brownian diffusion. Using linear combinations of Wigner rotation functions which each define a continuous orientational distribution, the rotational distribution of the molecules in the EPR spectrum may be simulated. A more in-depth explanation of the way EasySpin solves the equations for the slow motion regime is described by Stoll and Schweiger,[48] based on theory presented by Gamliel and Levanon[52] and Schneider and Freed.[53]

Alternatively, for fast-motion nitroxide spectra, EWVoigt and EWVoigtN[54] may be used, which simulates the spectra as the convolution of Lorentzian and Gaussian lineshapes, and allows the combination of two different components with different linewidth parameters, useful for separating out bound and unbound radical components for example. An advantage of using EWVoigt is that it allows for more efficient correction of phases errors in the spectrum than EasySpin, and so provides a good alternative for spectra which are in the fast-motion regime.

1.4 Aims of the project

As the literature shows, investigating the properties of self-assembled structures and their host-guest complexes is an area of research that has been, and continues to be, widely explored by many different groups using a variety of techniques. The aim of this project was to continue this work, focussing specifically on the investigation of self-assembled supramolecular cage structures, using stable radical spin probes to investigate them with EPR spectroscopy, in ways that had not been used for these particular structures before. The benefits of EPR spectroscopy, with the high sensitivity of the g- and A-values to chemical environment, and the lineshape to rotational motion of the radical guests, aimed to provide detailed and useful information about the host-guest complexes formed. By comparing the results obtained in this work to previous work it was possible to determine new information, as well as demonstrating the validity of using this method to explore the complexes.

1.5 Choice of cage structure

The cage structure chosen for study in this work was first reported by the Ward group in 2008.[55] The general form of this cage structure is $[M_8L_{12}][X]_{16}$ where M = Cd, Co or Ni, L = $C_{28}H_{22}N_6$ and X = BF_4, ClO_4 or Cl. The cage is approximately cubic in shape, with eight metal atoms at the vertices of the cube joined by bis-bidentate linking ligands which form the 12 edges. The metal cations are in a 2+ oxidation state in octahedral geometry, giving the cage structure a charge of 16+, which is balanced by the 16 negatively charge counterions associated with the structure.

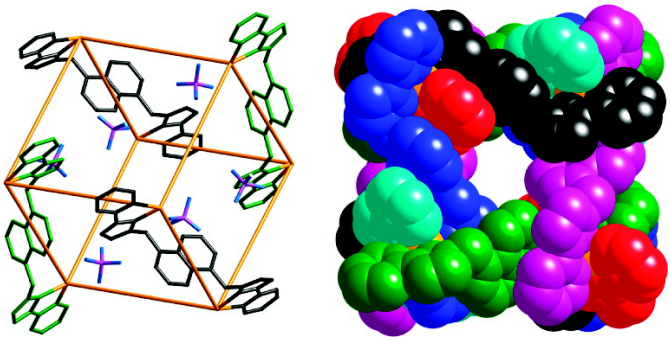

*Figure 20: Structure of the $[M_8L_{12}][X]_{16}$ cage showing four of twelve ligands and six counter ions (left) and space-filling view of the cage (right). Reprinted with permission from I. S. Tidmarsh, T. B. Faust, H. Adams, L. P. Harding, L. Russo, W. Clegg and M. D. Ward, J. Am. Chem. Soc., 2008, **130**, 15167–15175. Copyright 2008 American Chemical Society.*

This cage structure was chosen due to its reported stability both as a solid and in solution, making it easy to study in both forms. The relatively few synthetic steps to assemble the cage also made it desirable, as this should have enabled efficient synthesis. The size of the cage, specifically the cavity size, was also an important consideration, as the cavity needed to be

sufficiently large to accommodate the proposed radical guests. The cage chosen has an approximate cavity volume of 400 Å^3, which should be sufficient to encapsulate the intended guests, with the TEMPO and PROXYL derivatives having volumes ~180 Å^3.

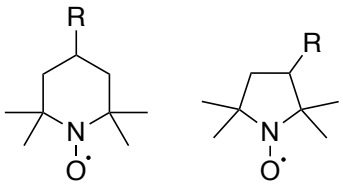

Figure 21 - General structures of TEMPO (left) and PROXYL (right) radicals.

This assumption was based on what is commonly known as Rebek's Rule – that the ideal volume for a guest inside a host complex will be ~55 % of the total internal volume of the host structure.[56,57] Since these guests have ~44 % occupancy of the cavity their volumes are slightly below this ideal size, but close enough that binding would still be expected if the binding can be stabilised by strong H-bond interactions.

Whilst the cavity size being large enough to accommodate the guests was an important consideration, it was also sensible to ensure that the cavity was not too large, as this would mean that only one guest molecule would be expected to be able to bind inside the cavity. This assumption would allow any binding studies to use formulae corresponding to 1:1 binding with relative confidence.

A final reason for choosing this cage structure was the flexibility afforded by the ability to change the metal atom and counterions associated with the cage structure. Changing these aspects increased the scope of the investigation by introducing slight variations that could be compared across the cages to gain greater insight. Using Cd as the metal allowed study of a diamagnetic cage, such that the only contribution to the EPR spectra was from the radical being investigated, whilst the use of Co allowed exploration into how the paramagnetic metal may have influenced the system. Meanwhile, the change in counterion allowed different solvents to be investigated – MeCN for ClO_4^- and H_2O for Cl^- - and hence allowed binding explorations where the dominant binding driving force was different.

This solubility in different solvents was desirable for potential investigation into radicals such as DPPH and Blatter-Type radical.

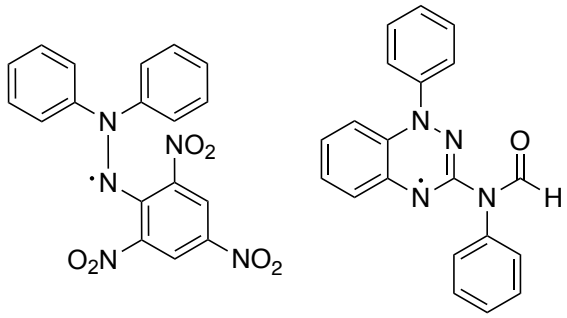

Figure 22 - Structure of DPPH (left) and Blatter-Type radical (right).

These radicals are soluble in organic solvent such as MeCN but not in H_2O, and are both strongly coloured, and so it was intended that for investigations with H_2O-soluble cage, binding may have made these radicals more soluble, which would have led to a change in colour of the solution, as well as the appearance of signal in the EPR spectrum, in contrast to using MeCN, where both radical and cage would be soluble. These radicals have volumes of approximately 316 $Å^3$, (79% occupancy) and 287 $Å^3$ (71 % occupancy) for DPPH and Blatter-Type radical respectively, meaning that it is less likely that they would be favourably bound within the cage. However, since Rebek et al. had previously reported success binding at ~70% occupancy due to extra stabilisation provided by H-bond acceptor/donor interactions between host and guest molecules,[56] it was thought that sufficiently strong intermolecular forces between the host and guest may stabilise a guest of this volume, as the aromatic groups of the radical may provide good stabilisation through such H-bond interactions, if a portion of the radical could be bound.

2 Synthesis of the cage

2.1 Synthesis of **P1**

The first step in the cage synthesis was to synthesise 1,5-bis(bromomethyl)naphthalene, **P1**, from 1,5-dimethylnapthalene via a radical bromination mechanism, using NBS as the source of bromine and 2,2′-azobis(2-methylpropionitrile) (AIBN) as the radical initiator (Scheme 3).

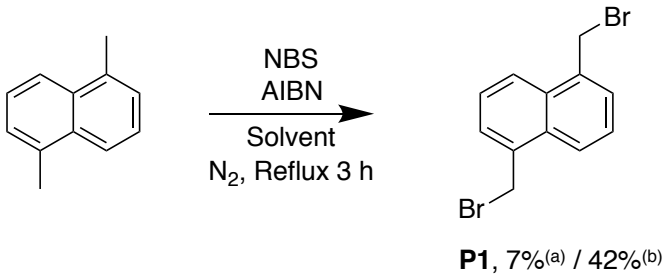

Scheme 3 - Synthesis of 1,5-bis(bromomethyl)naphthalene. Solvent is (a) MeCN or (b) CCl_4

Literature syntheses for **P1**[58–62] primarily used carbon tetrachloride as the reaction solvent, however complications in obtaining it due to delays in regulatory processes, led to attempting the synthesis using acetonitrile (MeCN) as an alternative solvent. MeCN was chosen as previous literature had reported successful radical bromination in similar systems using this solvent.[63] Chloroform was considered as an alternative solvent but, due to the labile nature of the hydrogen atom, was discounted, as this had the potential to interfere with the radical mechanism. Unfortunately, the reaction produced a complex mix of products as evidenced by NMR characterisations. This led to difficulties in separating the desired product from by-products of the reaction such as succinimide, which is soluble in MeCN but not in CCl_4. It is also likely that mono-brominated by-products were formed, which were not easily removed, and that the higher temperature required to reach reflux in MeCN may have also led to decomposition of by-products, further increasing crude product impurity. Use of separation techniques including column chromatography were attempted but only gave yields of 7%, which still had traces of impurity present. Had using MeCN as an alternative solvent proved more successful the results would have been interesting, since avoiding the use of CCl_4, a potent ozone depletor, would have made the reaction more environmentally friendly.

Once CCl_4 was obtained the reaction proceeded much more efficiently, with a greater yield obtained of 44 %. However, there was still some evidence of impurity in the aliphatic region of the NMR spectrum, illustrated in Figure 23 (top).

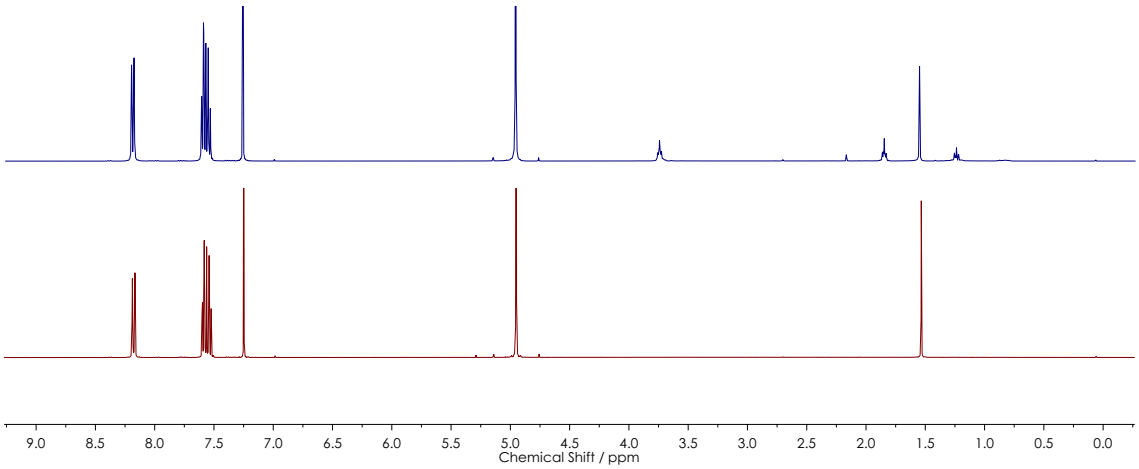

*Figure 23 - ^{1}H NMR spectra of **P1** without sublimation (top, blue) and with sublimation (bottom, red). The top spectrum shows impurity peaks at ~3.75, 2.17, 1.84 and 1.24 ppm, which are not present in the bottom spectrum.*

Upon including an additional sublimation step in the reaction synthesis, a purer product was obtained, albeit in slightly reduced yield. Further recrystallisation was then performed and NMR characterisation showed no significant impurity (Figure 23**,** bottom). Full experimental procedure can be found in Experimental Section 6.2.1 and NMR spectra can be found in Appendix 7.1.1**.**

2.2 Synthesis of **L1**

Following successful synthesis of **P1**, the ligand, **L1**, could be synthesised following the literature procedure, as described in Experimental Section 6.2.2 and shown in Scheme 4.

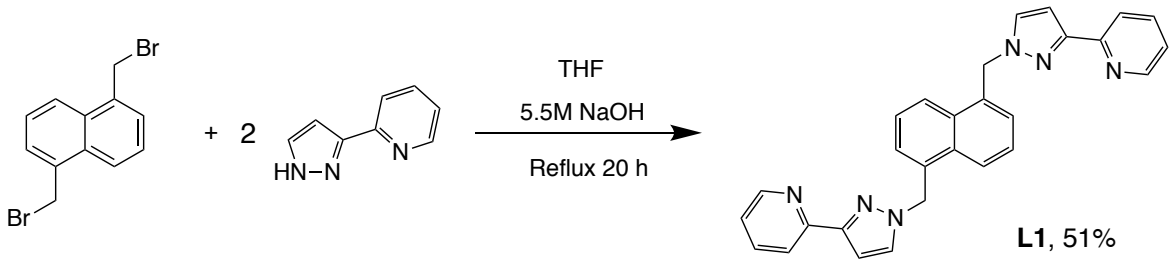

*Scheme 4 - Synthesis of **L1**.*

Initially, when using precursor **P1** that had been prepared without sublimation for the synthesis, peaks in the aliphatic region of the NMR spectrum were observed with similar shifts and splitting patterns to those ascribed to the impurities in the precursor NMR, suggesting that they were carried through and not removed during the work-up of **L1**. These peaks were no longer observed when using the purer sublimed product. Spectra are shown in Appendix 7.1.2. The product was also characterised by mass spectrometry, which showed peaks corresponding to the $(M+2H)^{2+}$, $(M+H)^{+}$, $(M+Na)^{+}$ as the most intense peaks, with few other peaks present. (Appendix 7.2.1) It was important to ensure the precursor **P1** and ligand **L1** were free from

impurities, as any impurities may have interfered with cage assembly, acting as templates leading to undesired products, thus hindering formation of desired cage products. Additionally, any impurity carried through may have been able to bind inside the cage, acting as a competing guest, and thus invalidating any binding studies carried out.

2.3 Synthesis of **C1** and **C2**

2.3.1 Procedure

In the literature, two different synthetic methods were presented for assembling the cage. The first – referred to as the "conventional method" – involved stirring solutions of the metal salt in MeOH and **L1** in $CHCl_3$ together at room temperature for 24 hours then working up the reaction mixture. The second – the "solvothermal method" – involved adding the salt and **L1** together with MeOH in an autoclave and heating the reaction mixture to 150 °C for 12 hours, before slowly cooling the reaction mixture, to yield product directly. Both methods were attempted in this work, but it was found that the conventional method yielded better results, with sharper product peaks in ^{1}H NMR discussed later, whilst the solvothermal method appeared unsuccessful. Therefore, the conventional method was used to prepare all the cage structures, with the reaction scheme shown in Scheme 5.

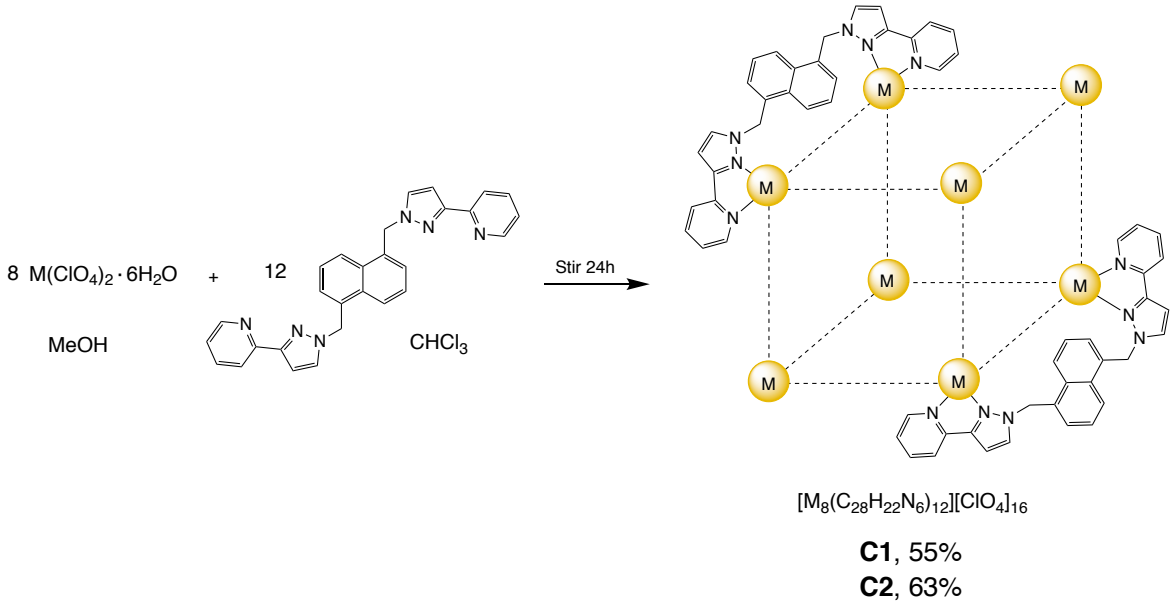

*Scheme 5 - Synthesis of **C1** (M = Cd) or **C2** (M = Co) via the conventional method.*

In this work, perchlorate metal salts were used in place of the tetrafluoroborate salts described for the syntheses in the literature, as they were more readily accessible, and had been shown to provide isostructural cage structures in work by Stephenson[64] and Ward and co-workers.[65]

2.3.2 Characterisation

In order to confirm successful synthesis of the cage structure multiple characterisation techniques were employed. ^{1}H NMR was used for both **C1** and **C2**, whilst ^{113}Cd NMR was also used for **C1**.

The cage possesses non-crystallographic or molecular S_6 symmetry (see Figure 24), meaning that the atoms in a single cage structure may be related by the S_6 symmetry operation.

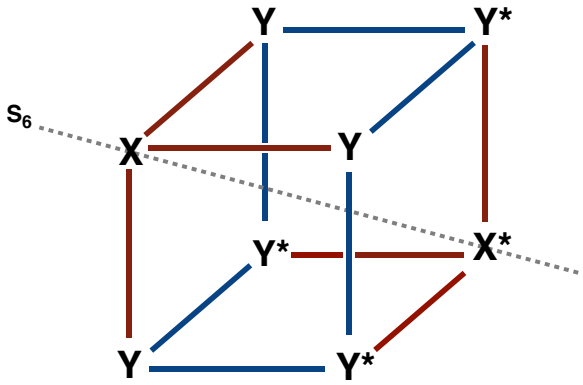

*Figure 24 - Representation of the cage structure highlighting the non-crystallographic S6 symmetry. The dotted grey line indicates the position of the S_6-axis. Facial tris-chelate metal centres are represented by X and meridional centres represented by Y. * Indicates the corresponding enantiomer. The different edge colours represent different bridging ligand environments.*

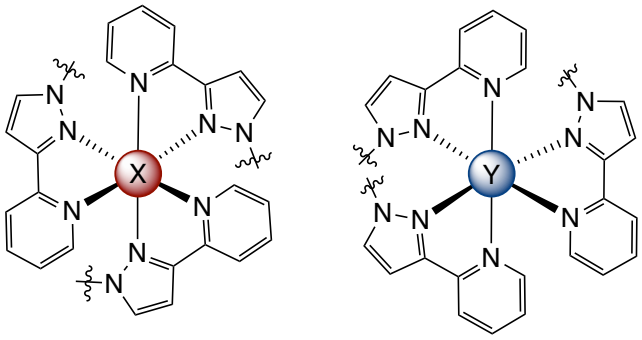

Figure 25 - Ligand binding to the metal atoms of the cage. Left: facial; Right: meridional.

Because of this molecular symmetry there are expected to be two different metal environments, X and Y, (and their equivalent enantiomers X* and Y*) (Figure 24) which correspond to *facial* and *meridional* binding of the ligands to the metal respectively (Figure 25). This in turn leads to two different general ligand types, one type connecting X and Y (X-Y or X*-Y*) and one connecting Y and Y* (Y-Y*). Each ligand type gives rise to 22 proton signals each, so a total of 44 signals were expected in the ^{1}H NMR, with many of them overlapping. A full explanation of the proton environments may be found in the paper by Tidmarsh et al.[55] The large number of overlapping signals means a definitive assignment of all H environments is very difficult, so the spectrum instead was compared to that of $[Cd_8(L1)_{12}][BF_4]_{16}$ reported in the same paper

(where a complete assignment was also not attempted). Whilst some variations were expected due to the different counterion present (ClO_4^- in **C1** and BF_4^- in the literature[55]), it was found that there was good agreement between the two, with most peaks matching well when considering the peak integrals, multiplicity and chemical shift. Integrals for the recorded and digitised literature are shown on the spectra in Figure 26 and Figure 27 respectively.

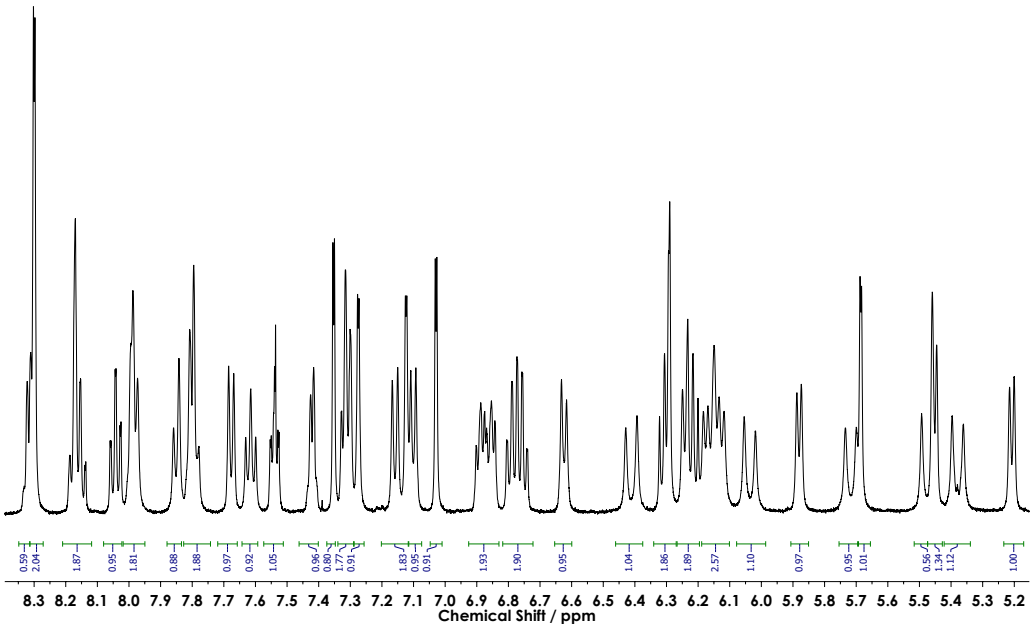

*Figure 26 - ^{1}H NMR (CD_3NO_2, 500 MHz) of **C1** – zoomed to expected product region.*

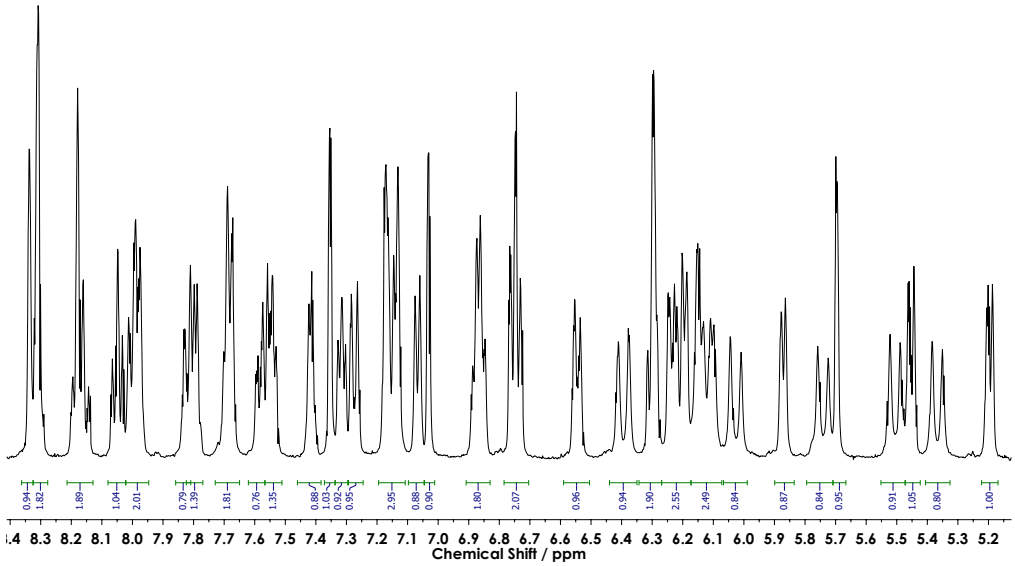

Figure 27 – Digitised ^{1}H NMR (CD_3NO_2, 500 MHz) of $[Cd_8(\mathbf{L1})_{12}][BF_4]_{16}$. Adapted from reference.[55]

^{113}Cd NMR was also used to confirm successful synthesis of **C1**, again by comparison to the literature spectrum. Two cadmium environments were expected in a 3:1 ratio, as illustrated above. The peaks seen in the recorded spectrum are very broad and integrate in a ratio of 2.32:1,

but appear at approximately the correct chemical shift, with peaks centred at ~-446.5 and -449.0 ppm. The whole spectrum (Appendix 7.1.3) has a significant amount of noise, but since these two peaks are still clearly discernible, despite their broadness, this supported that the correct product had been synthesised.

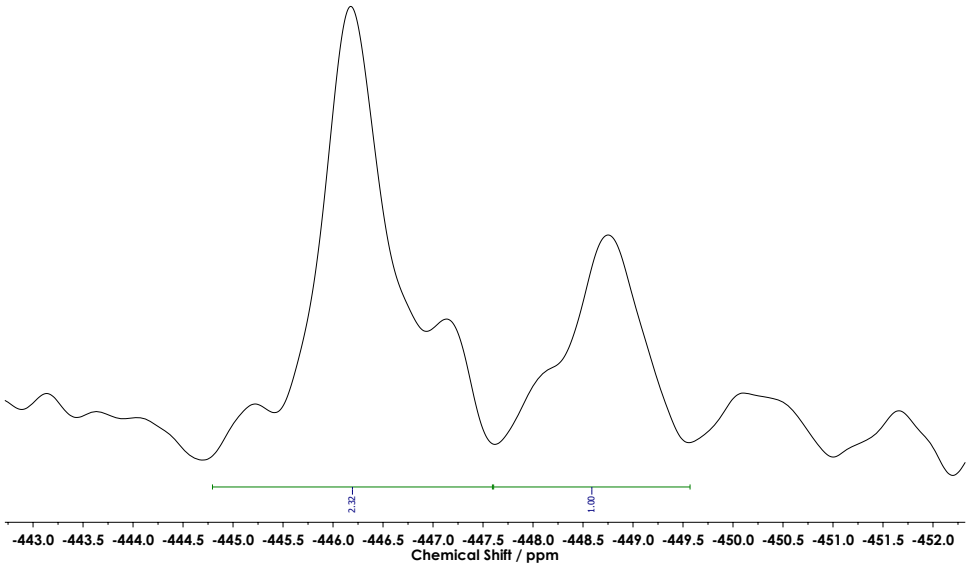

*Figure 28: ^{113}Cd NMR of (**C1**) in CD_3NO_2 showing two broad peaks at -446.5 and -449.0 ppm in a 2.32:1 ratio.*

The NMR spectrum obtained for **C2** is shown in Appendix 7.1.4, and was compared to literature spectra to confirm successful synthesis.

In addition to the NMR characterisation, mass spectrometry was also used to confirm the successful synthesis of **C1** and **C2.** In the literature, a clean spectrum of distinct peaks, corresponding to multiply-charged cage structures formed due to loss of BF_4^- counter-ions during the ESI experiment, was reported for the $[Co_8L_{12}][BF_4]_{16}$ structure. However, this was not observed for the cage products synthesised in this work. For **C1** only peaks corresponding to X = 5 and 6 for $[Cd_8L_{12}][ClO_4]_{16-X}{}^{X+}$ (X =5 expansion shown in Figure 29, X = 6 shown in Appendix 7.2.2) were found to match well with predictions based upon their intensity pattern and m/z position. Full spectra are also shown in Appendix 7.2.2. It is possible that the change from BF_4^- counterion to ClO_4^- is the main reason for the discrepancy between the peaks observed in the literature and experimental spectra, perhaps indicating that the ClO_4^- ion is bound more strongly to the cage structure, and so loss of the counterions to produce the multiply charged cage structures is more difficult.

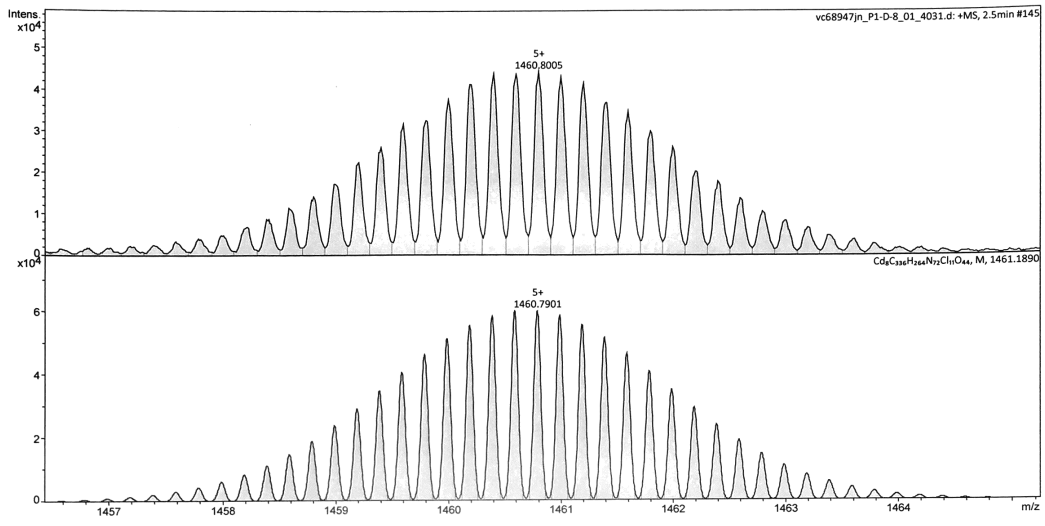

*Figure 29 – Top: Expansion of 5+ peak of experimental mass spectrum of **C1**, corresponding to loss of 5 ClO_4^- ions. Bottom: Predicted 5+ peak for $[Cd_8(L1)_{12}][ClO_4]_{11}^{5+}$*

For **C2** peaks corresponding to X = 4, 5 and 6 for $[Co_8L_{12}][ClO_4]_{16-X}^{X+}$ were observed, again which matched well with the predicted fragments with respect to intensity and position. The mass spectra for **C2** and the relevant expansions are shown in the Appendix 7.2.3**.**

2.4 Ion Exchange of **C2** to **C3**

In order to increase the scope of the investigation it was desirable to make the cage soluble in water. This was achieved by following a method reported by Cullen et al. in a recent paper discussing their work with cages of this type.[18] Whereas previously the ligand was modified to achieve water solubility,[66] extending and complicating the synthetic route, this method used the same synthesis, but exchanged the counter-ion to achieve solubility instead. In the literature BF_4^- ions were exchanged for Cl^- ions, whilst in this work ClO_4^- ions were used as shown in Scheme 6.

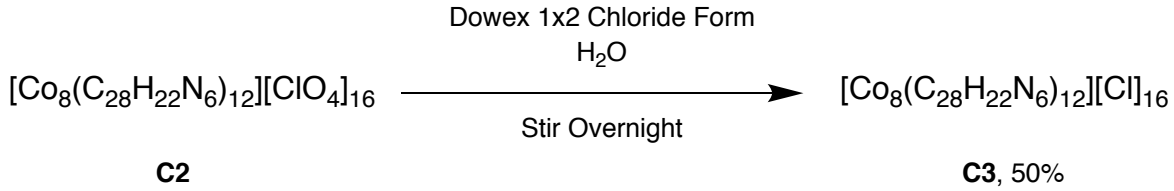

Scheme 6 - Conversion from MeCN soluble to H_2O-soluble cage using Dowex® Resin.

Successful conversion was confirmed by recording a ^1H NMR in D_2O and comparing to the literature spectrum obtained in the paper by Cullen et al.[18] The presence of signals in D_2O indicated that the cage had become soluble, and comparison between the experimental and literature spectra found good agreement between the peaks. Comparison to spectra recorded

of **C2** in $MeNO_2$ showed differences that can likely be attributed to the change in solvent and the change in counterion, confirming successful conversion. The experimental NMR spectrum is shown in Appendix 7.1.5 and literature spectrum shown in Appendix 7.1.6.

Conversion of **C1** into a water-soluble analogue was attempted, but no product could be isolated from the exchange reaction mixture or characterised, despite multiple filtration attempts.

Mass spectrometry was attempted for **C3** using both D_2O and $MeNO_2$ as the solvent, but unfortunately no peaks that could be assigned to product were observed in either solvent. This is likely due to the need for optimisation of the solvent system and concentration of cage used for the characterisation, as well as possible impurities in the sample, as the large and multiply charged cage structures formed will not necessarily be easily identified in the spectrum if more intense peaks not due to these impurities, or perhaps cage fragmentation, dominate the spectrum. As mass spectrometry data was not reported in the literature it would appear that obtaining a spectrum for the H_2O-soluble cage may be more challenging than for the MeCN-soluble cage.

2.5 Conclusions

Characterisation by NMR spectroscopy and mass spectrometry of the precursor **P1**, ligand **L1** and cage structures **C1**, **C2** and **C3** confirmed that desired structures had been obtained, with comparison to previous literature aiding the confirmation. It would have been desirable to obtain crystal structures of all the cages to help confirm successful synthesis, but unfortunately X-ray quality single crystals were not obtained for any of the structures. However, since the other characterisation evidence indicated that the cages had been synthesised as expected, investigations into guest binding were begun.

3 Binding of stable free radicals to the cage: a qualitative study

Once the cage structures had been successfully synthesised and characterised, explorations into potential guests suitable for the binding studies were begun. These studies aimed to test qualitatively whether the radicals were binding to the cage by comparing the spectra of radical solution with radical+cage solution and observing any differences between the two, noting whether this change corresponded to what might be expected upon binding.

For the initial investigations, unless stated otherwise, stock solutions of radical (4×10^{-5} M) and cage (1×10^{-3} M) were made up in the same solvent, either MeCN for **C1** or **C2** and H_2O for **C3**. A measured volume of radical solution was then combined with an equal volume of either neat solvent or cage solution, to yield a radical sample (~2×10^{-5} M) and a cage+radical solution with radical concentration ~2×10^{-5} M and cage concentration ~5×10^{-4} M. The samples were then transferred to capillaries, EPR spectra recorded at X band, and the two spectra compared. To maximise binding, high concentrations of both cage and radical guest were used, and it was ensured that cage was in excess.

For the samples in MeCN, the solutions were transferred to sealed Pasteur pipettes, and degassed with N_2 to reduce any broadening effects arising from the dissolved oxygen in the solvent interacting with the nitroxide radicals in solution.

For the samples in H_2O, sealed melting point tubes were used, internal diameter 0.8 mm, which were placed inside a larger glass tube to hold the capillary in place inside the cavity. Since polar solvents like water absorb microwave radiation well, the decreased diameter of the melting point tubes leads to a smaller sample volume, which helps to reduce the amount of absorption, and therefore also the broadening of the spectrum that results. This is because the capillary is placed at the centre of the cavity, where absorption of the electrical components of the microwave is at a minimum, but absorption of the magnetic component is strongest, on a similar principle to that of a flat cell. The samples were not degassed as the dissolved oxygen content of the H_2O was considered low enough that the spectra should be well-defined enough to study. Another consideration was the difficulty in degassing different samples evenly, due to the small diameter of the capillaries used, and it was decided that attempts to degas the solutions may in fact lead to greater discrepancy between samples.

3.1 TEMPO (**R1**)

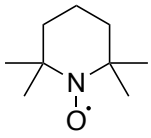

*Figure 30 - Structure of TEMPO (**R1**).*

TEMPO (**R1**) (Figure 30) was the first radical investigated with cage **C3** in H_2O. This structure had been mentioned as a potential guest in one of the previous papers[27] so was a good starting point. As TEMPO is a nitroxide radical, the EPR spectrum contains three signals due to hyperfine coupling between the unpaired electron and the ^{14}N nucleus. The expected change in the EPR spectrum upon addition of cage was that the signal would be broadened due to reduced tumbling rate, and so the spectrum would look more anisotropic, and move towards the slow-motion regime. The spectra for **R1** and **R1**+**C3** are shown in Figure 31.

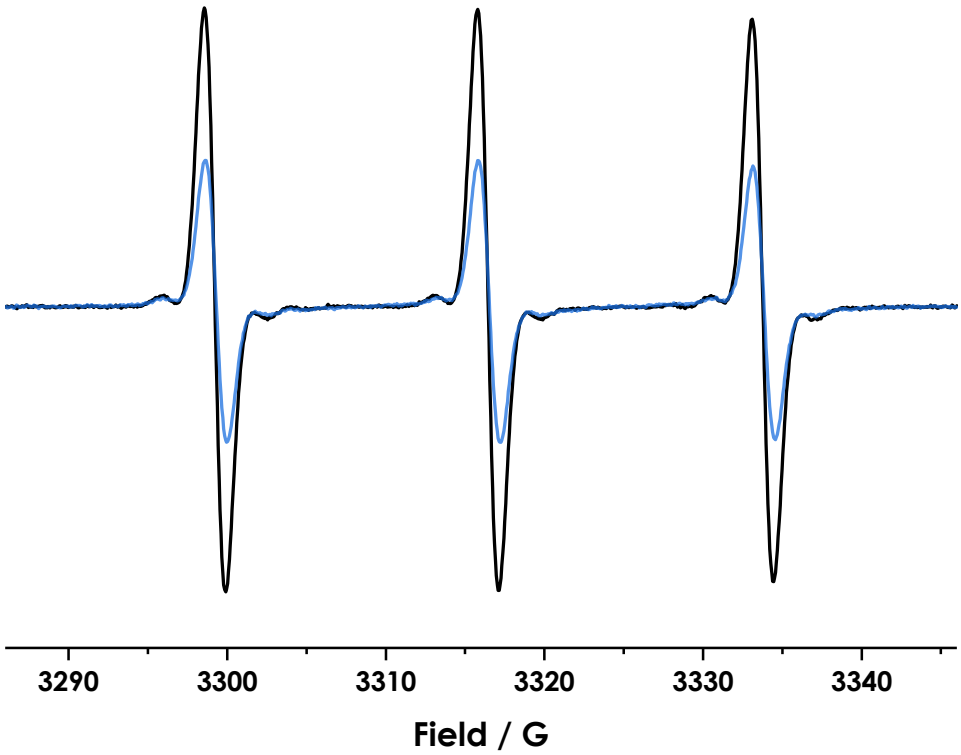

*Figure 31 - EPR spectra of 2×10^{-5} M TEMPO (**R1**) (black) and **R1**+**C3** (blue) in H_2O. Addition of **C3** to **R1** led to a decrease in signal intensity.*

Upon first inspection, the observed decrease in the signal intensity could be taken as a sign of binding, leading to broadening of the signal. To ensure this was the case, rather than an experimental artefact or the destruction of the radical, a competing guest was added for which the binding constant was assumed to be greater than that of the radical based on previous literature. The competing guest chosen for this radical@cage complex was hexamethylacetone (**CG1**) (Figure 32).[67]

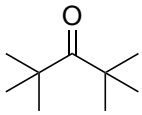

CG1

*Figure 32 - Structure of hexamethylacetone, competing guest 1 (**CG1**).*

It was expected that the competing guest would preferentially bind inside the cage, preventing and displacing any radical binding, and leaving a solution for which the EPR spectrum would closely match that of **R1** with no cage added.

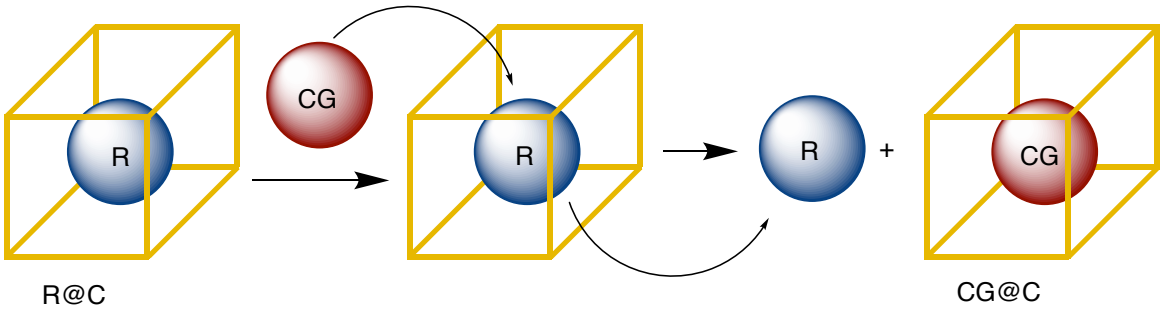

Figure 33 - Diagram showing the addition of generic competing guest (CG) to radical@cage solution (R@C) to yield a solution containing unbound radical (R) and CG@C complex.

However, when **CG1** was added to **R1@C3** solution, the signal in the EPR spectrum did not return to the same linewidth and intensity as of **R1** in neat solution, as illustrated in Figure 34.

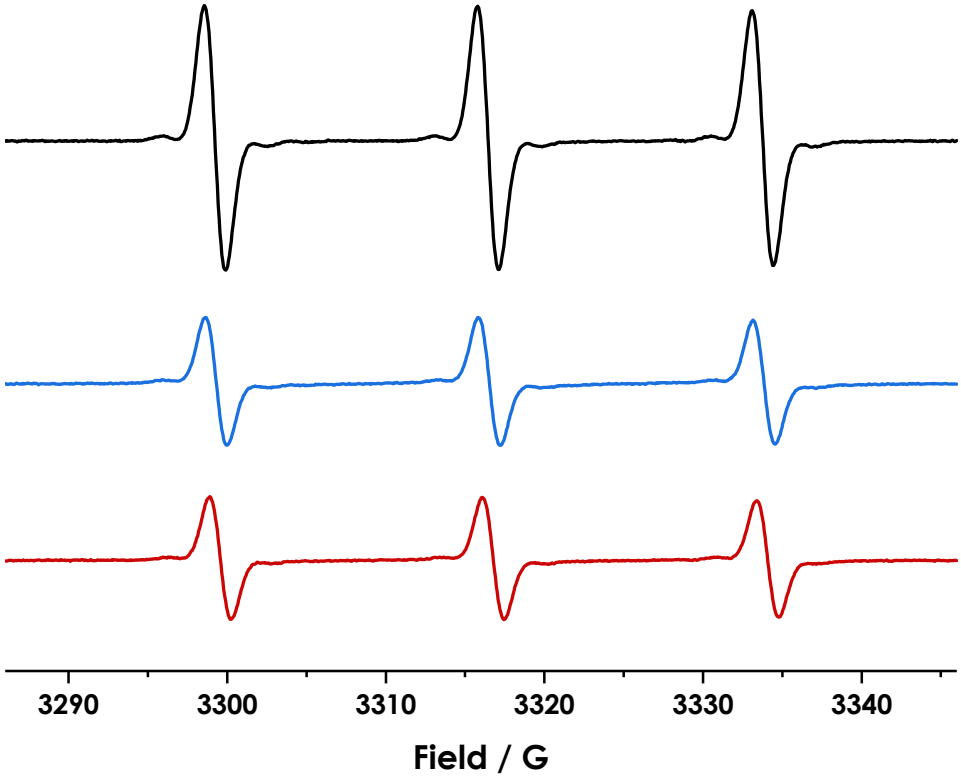

*Figure 34 - EPR spectra of solutions of: 2×10^{-5} M TEMPO (**R1**) (top, black); 2×10^{-5} M **R1** + 5×10^{-4} M **C3** (middle, blue); 1.82×10^{-5} M **R1** + 4.55×10^{-4} **C3** + 2.27×10^{-3} **CG1** (bottom, red). (Addition of competing guest increased total sample volume, causing radical and cage concentrations to decrease slightly)*

Instead the spectral lineshape and intensity remained constant, suggesting it was not a binding effect being observed, but that another effect was broadening the signal. This effect was suspected to be due to either exchange between bound and unbound radical, or the paramagnetic nature of the cobalt atoms in **C3**, which would broaden the signal through Heisenberg exchange. The latter was deemed more likely, since the competing guest was added at a significantly high concentration that there should be no bound nitroxide left, such that no exchange would be seen.

A theoretical explanation of how Heisenberg exchange affects EPR spectra is detailed by Freed[68], who explains that the effect arises when two paramagnetic species collide, resulting in an exchange of their electron spin states. The frequency of this exchange is assumed to be such that the duration of collision is short when compared to the effective exchange time, and that the time between the collisions is greater than the time taken for any rotational and translational relaxation.

The overall effect of this exchange parameter is to introduce additional broadening, which is dependent on the frequency of collisions, and hence concentrations of the radical and cobalt

atoms. Since all of the bound radicals experience the same environment within the cage, this means the broadening is homogenous, and thus additional, purely Lorentzian, broadening is introduced to the spectrum.

The amount of broadening observed in the spectrum was consistent with the concentration of the paramagnetic ions in the sample, as was confirmed in the next section for 4-oxo-TEMPO.

3.2 4-oxo-TEMPO (**R2**)

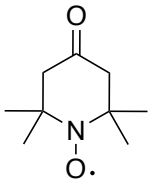

*Figure 35 - Structure of 4-oxo-TEMPO (**R2**).*

After **R1**, 4-oxo-TEMPO (**R2**) (Figure 35) was investigated, as the extra carbonyl group was expected to allow stronger binding to the internal cavity of the cage by providing a good H-bond acceptor site. Again, it was expected that the EPR spectrum of **R2**+**C3** would be broader than that of just **R2**, due to restricted motion of the radical.

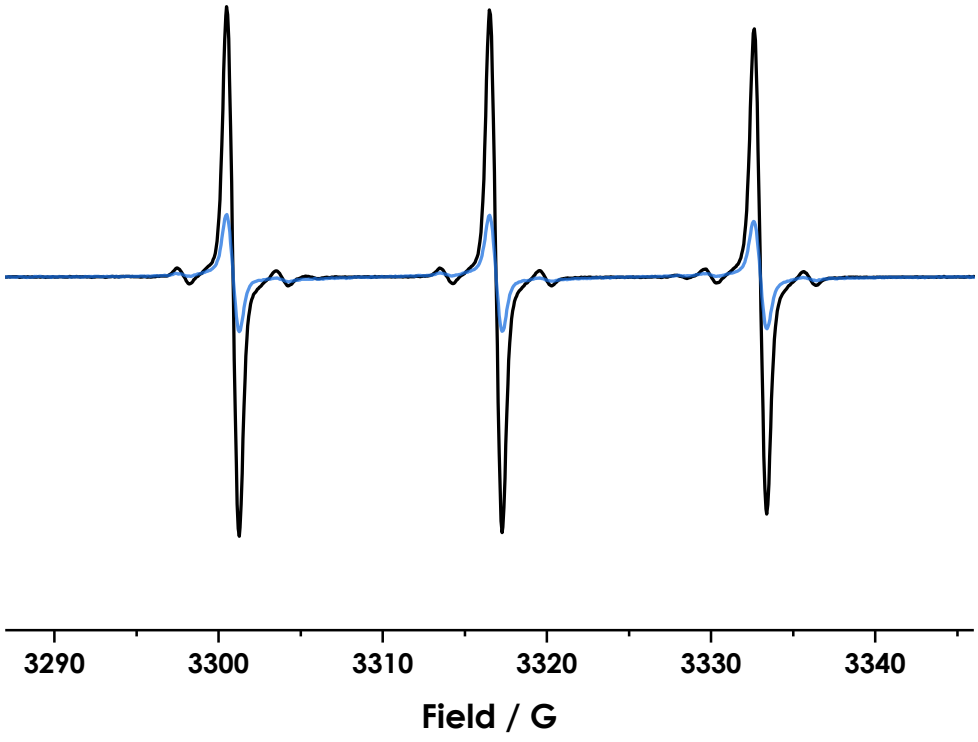

*Figure 36 - EPR spectra of 2×10^{-5} M 4-oxo-TEMPO (**R2**) (black) and **R2**+**C3** (blue) in H_2O.*

A much larger difference was seen upon addition of **C3** to **R2** than was observed for **R1**, suggesting this time that radical binding to the cage was successful, and that the broadening

effects were due to the restricted motion effects of binding, in addition to interactions with the cobalt atoms. To confirm this was the case, **CG1** was added to solution of **R2**+**C3**, and the EPR spectrum recorded. The three different spectra are shown in Figure 37.

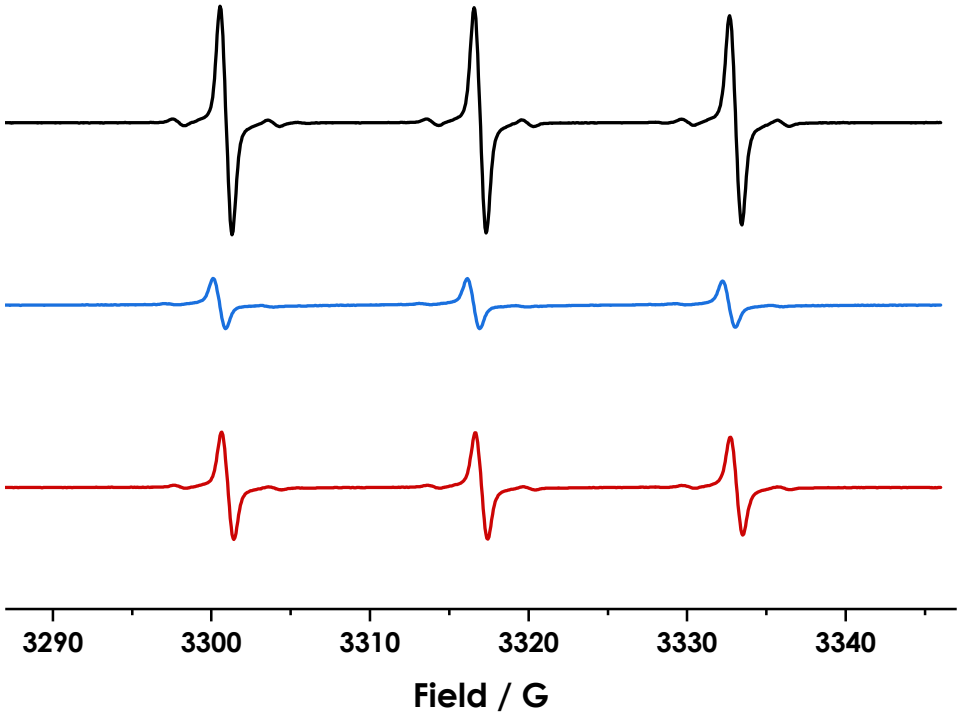

*Figure 37 – EPR spectra of solutions of: 2×10^{-5} M 4-oxo-TEMPO (**R2**) (top, black); 2×10^{-5} M **R2** + 5×10^{-4} M **C3** (middle, blue); 1.82×10^{-5} M **R2** + 4.55×10^{-4} **C3** + 2.27×10^{-3} **CG1** (bottom, red). (Addition of competing guest increased total sample volume, causing radical and cage concentrations to decrease slightly)*

In contrast to the spectrum for **CG1** + **R1**+**C3**, the linewidth and intensity of the spectrum for **CG1** + **R2**+**C3** was not the same as for **R2**+**C3** and was instead somewhere between this spectrum and the spectrum for **R2** in neat solvent. This suggested that **R2** had been bound and subsequently displaced, and that the extra broadening due to the cobalt atoms was still present in the spectrum also containing competing guest, as would be expected.

As a control experiment, to show that the extra broadening seen for both **R1** and **R2** was due to the cobalt atoms, an 8×10^{-5} M $Co(ClO_4)_2{\cdot}6H_2O$ solution was added to a 1×10^{-3} M solution of **R2**. The concentration of cobalt atoms in this combined solution was equal to the concentration in the radical@cage solution, such that the ratio between cobalt atoms and radical molecules was the same. However, no binding to the $Co(ClO_4)_2$ was expected, and instead any line broadening effects observed would be attributed to collisions, and hence exchange interactions, between the $Co(ClO_4)_2$ and radical molecules. The EPR spectrum of this new solution showed a broadening similar to that of the **R1+C3** and **R2**+**C3**+**CG1** spectra, indicating

that the observed broadening was indeed due to Heisenberg exchange between the radical and the cobalt atoms. Addition of **CG1** to this solution did not appear to affect the signal in any way, also confirming that broadening was not being influenced by any binding that could be disrupted by addition of competing guest. A comparison between the spectra obtained is shown in Figure 38.

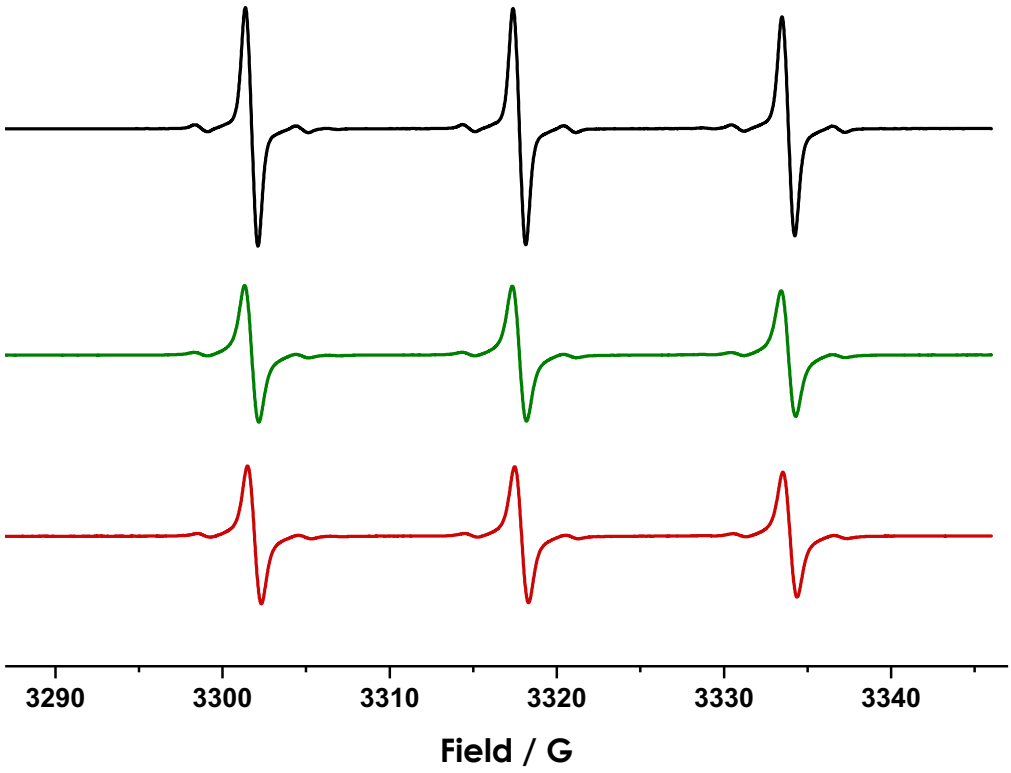

*Figure 38 - EPR spectra of solutions of: 4-oxo-TEMPO (**R2**) (top, black); **R2** + $Co(ClO_4)_2 \cdot 6H_2O$ (middle, green); **R2** + $Co(ClO_4)_2 \cdot 6H_2O$ + **CG1** (bottom, red). Concentration of radical is 2×10^{-5} M in all cases, concentration of $Co(ClO_4)_2 \bullet 6H_2O$ was 8×10^{-5} M and concentration of **CG1** was ~2×10^{-3} M.*

This confirmation provided more evidence that the effects observed upon addition of **C3** to **R2** were a combination of binding and exchange effects, and so suggested that **R2** would be a suitable radical to carry out more detailed binding studies on. These studies are presented in Chapter 4.

3.3 4-carboxy-TEMPO (**R3**)

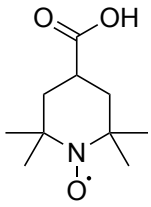

*Figure 39 - Structure of 4-carboxy-TEMPO (**R3**).*

Following on from the carbonyl derivative, the carboxy derivative of TEMPO was investigated, this time with **C1** instead of **C3**. The change to the Cd cage and MeCN was made as it was expected that the carboxy group would provide a better H-bond acceptor site than the carbonyl group, and so could hopefully bind strongly without the need for the additional hydrophobic driving force present for **C3**. As **C1** was diamagnetic, this also provided a benefit, as there would be no metal-radical interactions observed in the EPR spectra, and so investigation would focus purely on any change in the spectra due to binding effects. It was found that upon addition of the cage to the radical, a broadening of the signal was observed, similar to the effect observed for **R3**. The spectra are shown in Figure 40.

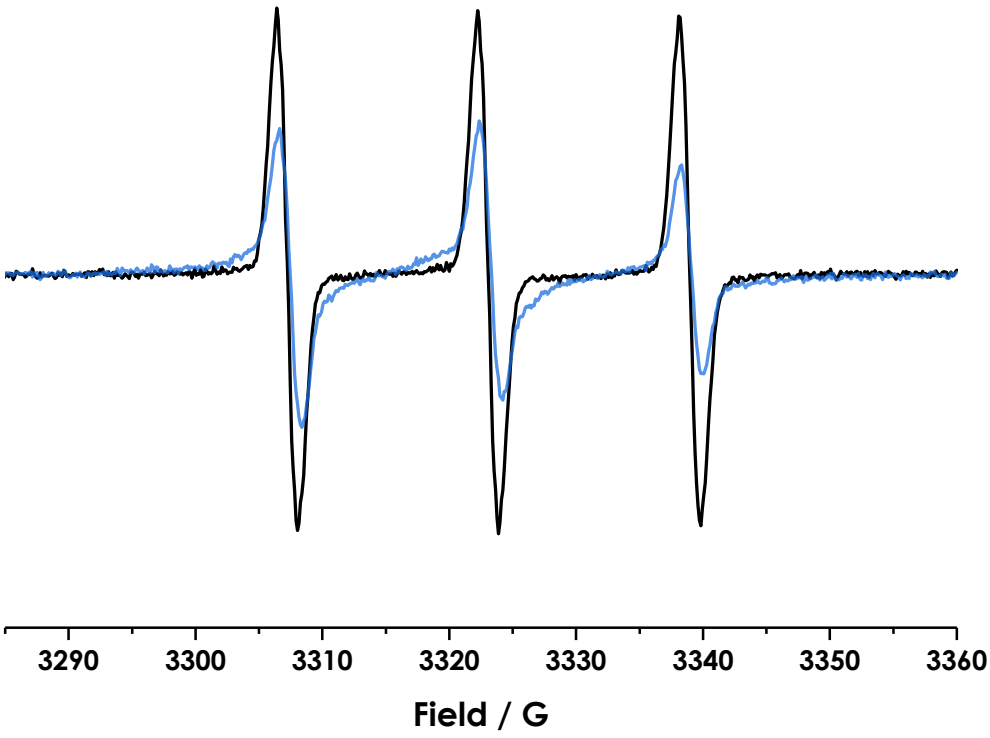

*Figure 40 - EPR of spectra of 2×10^{-5} M 4-carboxy-TEMPO (**R3**) (black) and **R3**+**C1** (blue) in MeCN.*

Due to the lack of paramagnetic metal atoms in **C1** it was more likely that the broadening observed was a result of binding, making **R3** another good candidate for further binding studies, this time in MeCN rather than H_2O. However, a competing guest was again used to ensure it was a binding effect.

For the MeCN-soluble cage **C1**, hexamethylacetone, **CG1**, could not be used as the competing guest, as the major driving force for binding in this case was not the hydrophobic effect as it had been in the H_2O-soluble cage **C3**. Instead, the strength of binding is mainly determined by the H-bond acceptor nature of the guest,[26] as the internal cavity of the cage contains H-bond donor sites which will allow binding, and as such **CG1** was not a good enough H-bond acceptor. Therefore, another competing guest was needed.

Since the main binding mechanism of radical to cage was assumed to be through the carboxy group, (confirmed by the initial binding studies comparing 3-carboxy-PROXYL and 3-carbamoyl-PROXYL, below) the competing guest chosen, benzoic acid, **CG2,** also contained this functional group. It was therefore expected that it would bind via the same mechanism, but would have the additional benefit of an aromatic ring group which could further enhance binding ability due to the extra H-bond acceptor ability afforded by the ring, as discussed by Turega et al.[25]

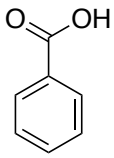

*Figure 41 - Structure of benzoic acid, competing guest, **CG2**.*

It was expected that, as previously, the competing guest would disrupt the radical binding and lead to an EPR spectrum that matched closely with the spectrum for the radical with no cage added. As **C1** contains cadmium atoms which are diamagnetic, rather than the paramagnetic cobalt atoms, no Heisenberg exchange effects were expected. However, as can be seen in Figure 42, upon addition of the competing guest, the spectrum increased in intensity above that of the purely radical spectrum.

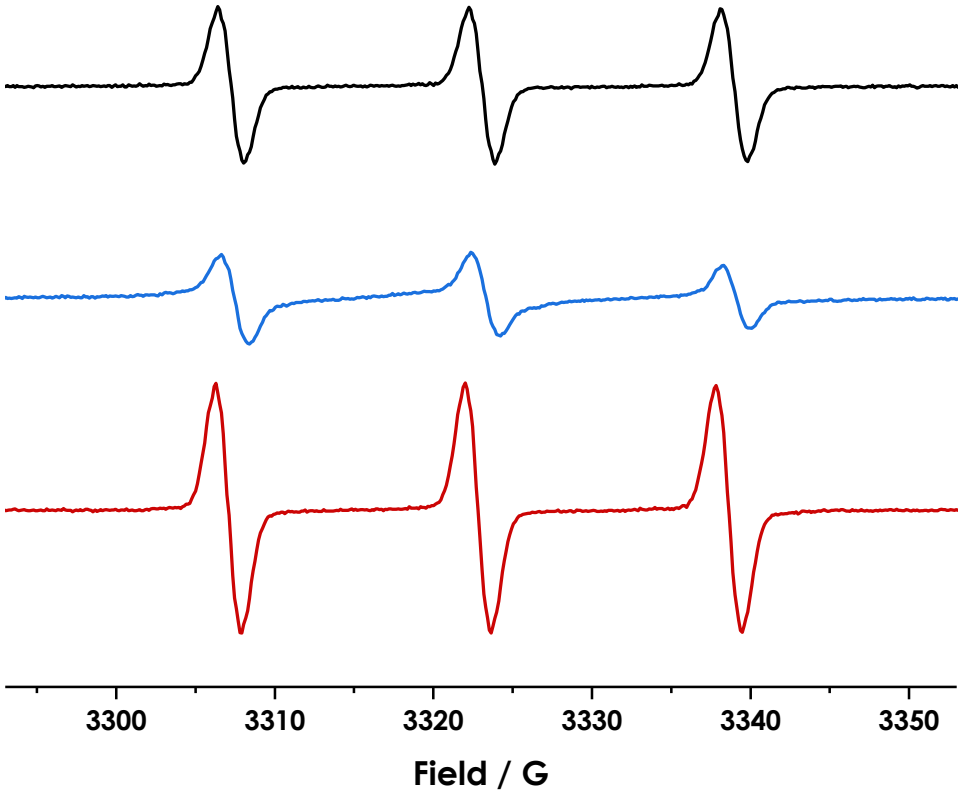

*Figure 42 – EPR spectra of solutions of: 2×10^{-5} M 4-carboxy-TEMPO (**R3**) (top, black); 2×10^{-5} M **R3** + 5×10^{-4} M **C1** (middle, blue); 1.82×10^{-5} M **R3** + 4.55×10^{-4} **C1** + 2.27×10^{-3} **CG2** (bottom, red). (Addition of competing guest increased total sample volume, causing radical and cage concentrations to decrease slightly)*

This behaviour is attributed to the fact that in solution the radical-containing carboxylic acid may form dimers, as described by Marshall[69] and later by Kooser.[70] This means that a more complex spectrum is observed, consisting of multiple lines, similar to a bi-radical spectrum. In rigid biradical spectra, the shape is dependent on the ratio between exchange interaction, J, and the hyperfine coupling constant, A. For a very strong exchange interaction, a five-line spectrum would be observed, whilst for a weak interaction, where J is less than the hyperfine coupling constant, three lines are observed. In flexible biradicals, the situation is more complex, and the spectra often contain multiple components depending on the strength of the exchange interaction, and the rate of conformational interconversion. In this case it likely that the formation of the flexible dimers leads to the visual effect of a broadened signal for the radical, due to the contribution of the multiple components, compared to a mono-radical spectrum. Upon addition of **CG2** the dimerisation was disrupted, meaning that the EPR spectrum only showed signal from a mono-radical, and hence there is no broadening effect, and the EPR spectrum appears to increase in intensity. By comparing the increase in intensity upon addition of **CG2** to a solution containing **R3** and **C1** and to one containing just **R3** it was determined that the addition of **CG2** increased the apparent intensity of the **R3**+**C1** spectrum by releasing any bound radical as well as disrupting dimerisation.

3.4 3-carboxy-PROXYL (**R4**)

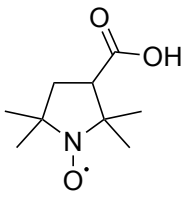

*Figure 43 - Structure of 3-carboxy-PROXYL (**R4**).*

After the apparent binding of **R3** with **C1**, 3-carboxy-PROXYL (**R4**) was chosen as an alternative radical probe to allow investigation into what effects, if any, the smaller ring size may have upon binding. Similarly to **R3**, the addition of cage to the radical solution led to broadening of the signal, as may be seen in Figure 44.

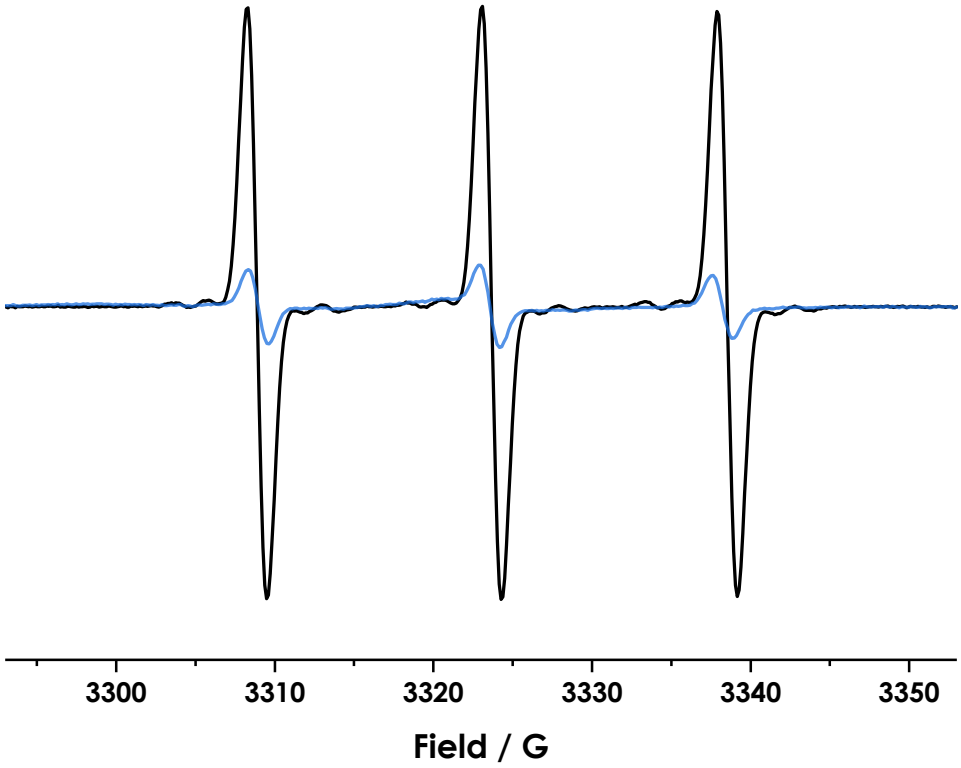

*Figure 44 - EPR spectra of 2×10^{-5} M 3-carboxy-PROXYL (**R4**) (black) and **R4**+**C1** (blue).*

When comparing the spectrum of **R4**+**C1** to that of **R3**+**C1**, the apparent decrease in intensity due broadening is far more pronounced. This was thought to be due to the motion of the radical being more restricted, as would be expected for a more rigid 5-membered ring structure. For the confirmation of binding with **R4**@**C1** the competing guest used was again benzoic acid, and the same effects were observed as for **R3**@**C1** where the apparent intensity of the spectrum

increased on addition of the competing guest, due to the disruption of dimerisation between the radical molecules in solution. The spectra are shown in Figure 45.

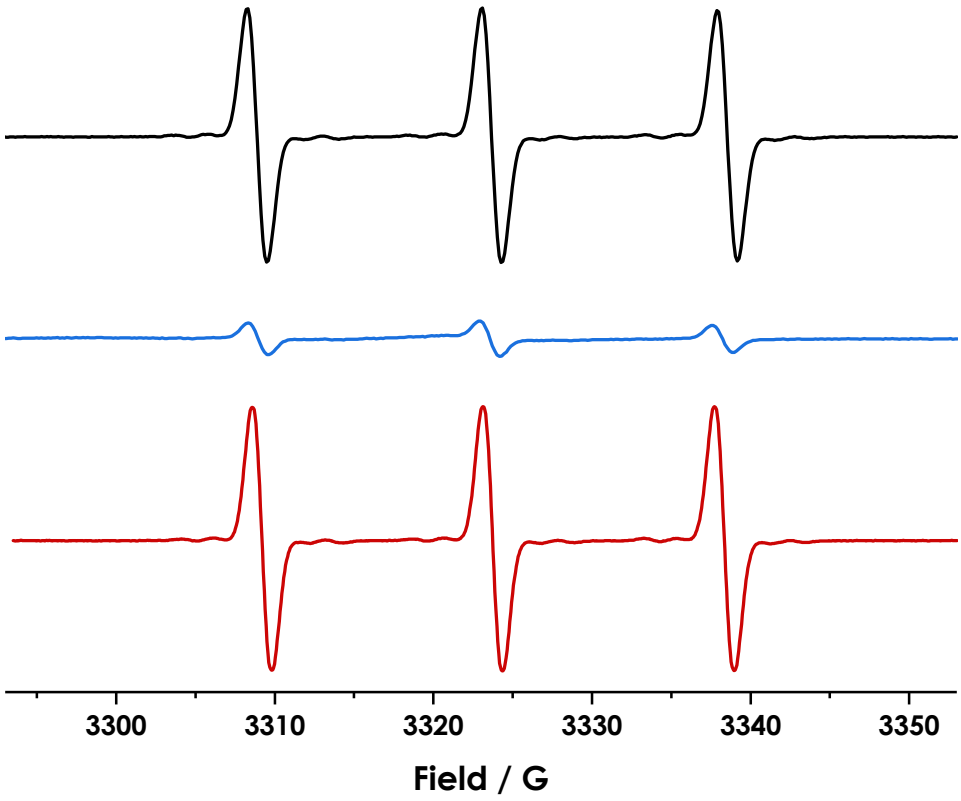

*Figure 45 - EPR spectra of solutions of: 3-carboxy-PROXYL (**R4**) (top, black); **R4** + **C1** (middle, blue); **R4** + **C1** + **CG2** (bottom, red). Concentration of **R4** was 2×10^{-5} M in all cases, concentration of **C1** was 5×10^{-4} M and concentration of **CG2** was ~2×10^{-3} M.*

Since the addition of **CG2** appeared to be releasing bound radical in addition to affecting dimerisation this suggested that **R4** would be a sensible radical to investigate further.

3.5 3-carbamoyl-PROXYL (**R5**)

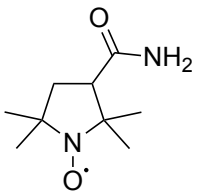

*Figure 46 - Structure of 3-carbamoyl-PROXYL (**R5**).*

In order to gain more insight into how **R4** may be binding to the cage, the similarly structured radical 3-carbamoyl-PROXYL (**R5**) was added to **C1** in MeCN. The change from the carboxy group to the amide allowed confirmation as to whether the group was important in the binding. The spectra for the **R5** and **R5**+**C1** samples are shown in Figure 47 in black and blue respectively.

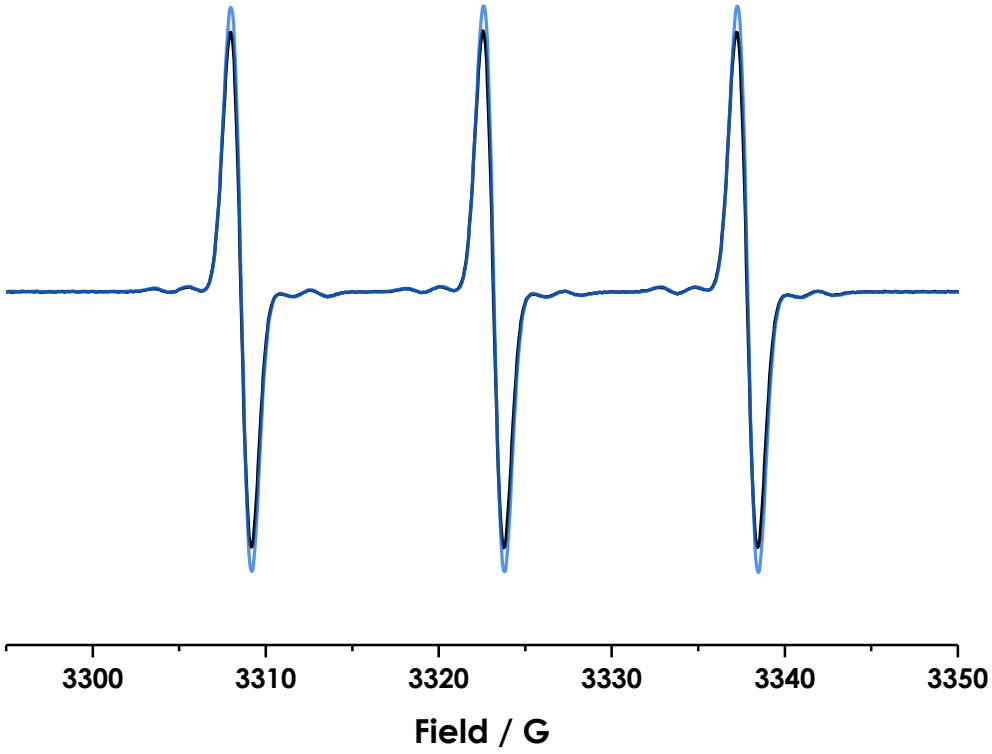

*Figure 47 - EPR spectra of 3-carbamoyl-PROXYL (**R4**) (black) and **R4**+**C1** solution (blue) in MeCN.*

Since the spectra here appear to be almost identical in their lineshape and intensity, this suggests that the radical was not bound to the cage structure, indicating that the carboxy group present in radicals **R3** and **R4**, and therefore perhaps the acidity of the molecules, plays an integral part in host-guest binding of these radicals.

3.6 Benzyl *tert*-butyl nitroxide (BTBN) (**R6**)

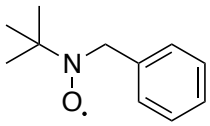

*Figure 48 - Structure of benzyl tert-butyl nitroxide (BTBN) (**R6**).*

Continuing with nitroxide radicals, the benzyl *tert*-butyl nitroxide radical (**R6**) was investigated next with cage **C3** again, rather than **C1**, since **R6** is not soluble in MeCN. This radical was chosen as previous work by Franchi et al.[71] had shown that the benzylic proton hyperfine couplings were highly sensitive to conformational changes when investigating binding of the radical to cyclodextrins. Therefore, it was expected that if binding to the cage was successful, clear differences between bound and unbound radical could be seen in the EPR spectra in addition to line broadening effects.

In contrast to the previous nitroxides, this radical was not stable however, and so was made *in situ* by heating combined solutions of benzyl *tert*-butylamine and magnesium monoperoxyphthalate hexahydrate,[71] and subsequently adding **C3**. The spectra for **R6** and **R6**+**C3** are shown in Figure 49.

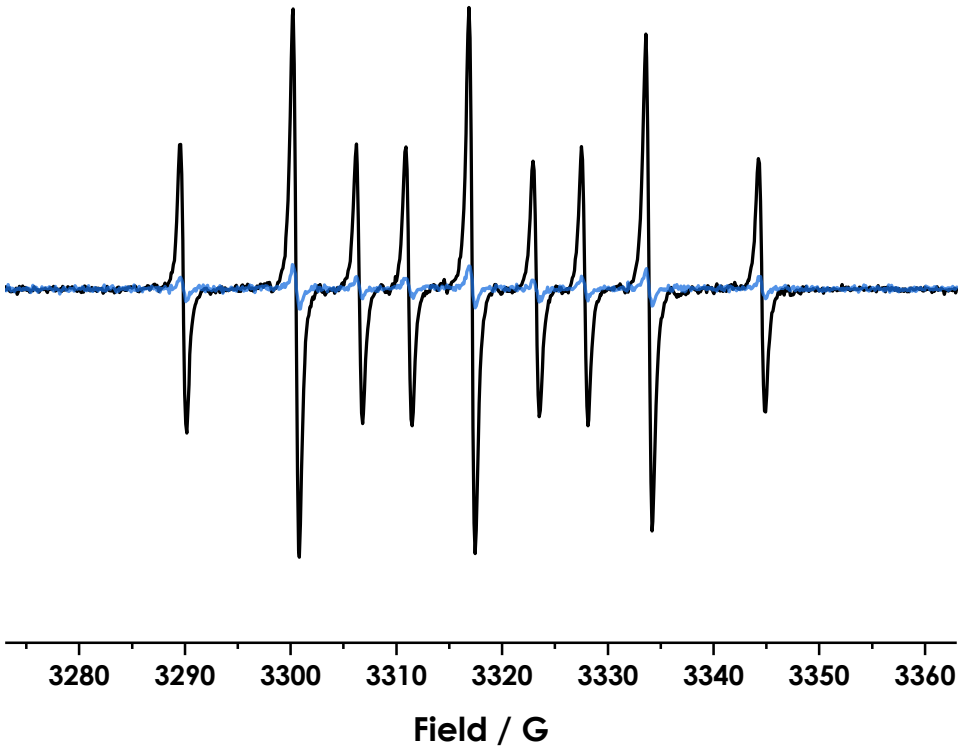

*Figure 49 - EPR spectra BTBN (**R6**) (black) and **R6**+**C3** solution (blue) in H_2O.*

As the spectra show, upon addition of **C3**, the spectral intensity is reduced compared to the radical in solution. However, as the hyperfine coupling to the benzylic protons appears to remain unchanged, this would suggest that no significant binding is being observed, and that the decrease is likely due to radical being destroyed by other impurities, and possibly broadening from the cobalt atoms of the cage. Addition of hexamethylacetone, **CG1**, did not reveal a return to the same intensity as radical in neat solvent, also confirming that no binding was observed, and that the radical was probably being destroyed.

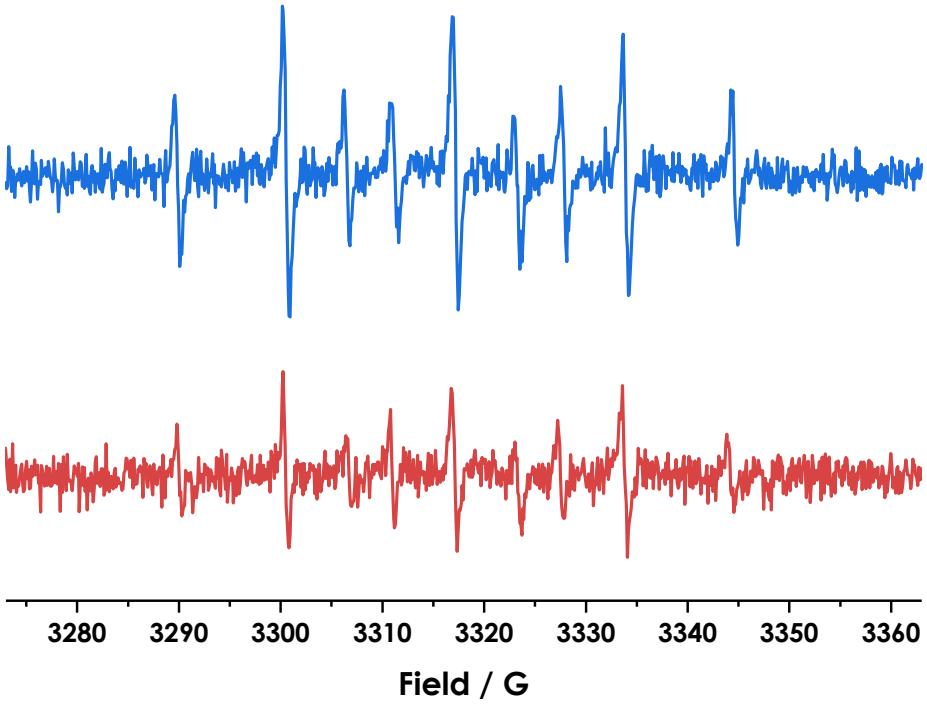

*Figure 50 - EPR spectra of **R6**+**C3** (blue) and **R6**+**C3**+**CG1** (red) in H_2O.*

The high noise-signal ratio of the **R6**+**C3** spectrum also made it unfeasible to study this radical further due to the difficulty that would be experienced when attempting to simulate the spectrum to obtain parameters.

3.7 Galvinoxyl (**R7**)

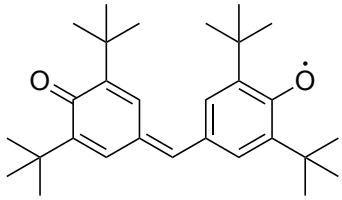

*Figure 51 - Structure of galvinoxyl (**R7**).*

After the nitroxides above had been investigated, galvinoxyl was chosen, as a larger, more rigid radical to investigate. Since the volume of the galvinoxyl molecule is ~450 Å^3, it was not expected that the whole radical could bind inside the ~400 Å^3 cage cavity. However, if a portion of the molecule, for example one of the aromatic ring groups, was to be bound, this would have led to changes in the EPR spectrum, although the bulky nature of the *tert*-butyl groups may have caused potential difficulty in passing through the cage portals. As the unpaired electron experiences significant hyperfine interactions with the methine proton, and four ring protons, leading to a well resolved doublet of quintets splitting pattern, it was expected that any binding

would change the environment of some of these protons enough that the hyperfine coupling would also change. This would then lead to an identifiable change in the splitting pattern of the EPR spectrum, alongside any change due to restricted motion effects. The spectra for the **R7** and **R7**+**C1** in MeCN are shown in black and blue respectively in Figure 52.

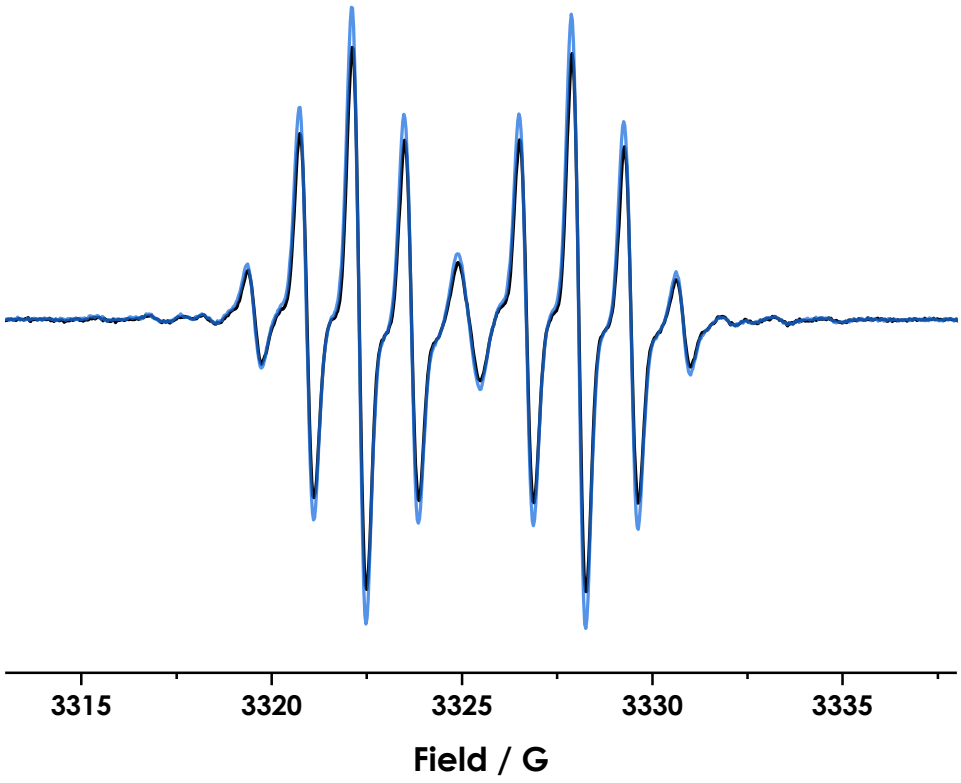

*Figure 52 - EPR spectra of galvinoxyl (**R7**) (black) and **R7**+**C1** solution (blue) in MeCN.*

The lack of any significant change in the spectrum of **R7**+**C1** compared to **R7**, suggests that binding of **R7** was not successful. This is likely due to the size of the radical as discussed, and lack of flexibility that would be required for a portion of the radical to become encapsulated.

3.8 Blatter-Type Radical (**R8**) and DPPH (**R9**)

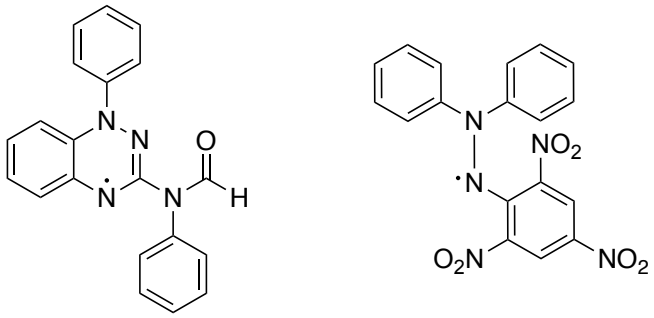

*Figure 53 - Structural formulae of Blatter Type-Radical (**R8**) (left) and DPPH (**R9**) (right).*

3.8.1 **R8** and **R9** in MeCN

Another avenue of exploration involved the stable Blatter-Type radical (**R8**) and 2,2-diphenyl-1-picrylhydrazyl (DPPH) (**R9**). These two radicals were both larger than the ideal size for binding inside the cage, (**R8**: ~287 Å^3, 71% occupancy; **R9**: ~316 Å^3, 79% occupancy) but it was thought that interactions between the aromatic groups of the radical and the H-bond donor groups in the cage cavity could possibly stabilise the larger size, or that only a portion of the radical may become bound inside the cage, leading to binding effects being observed in the EPR spectra.

Both of these radicals are delocalised, with significant spin density on the nitrogen atoms, with nine signals expected in the EPR spectrum of **R8** due to hyperfine coupling to the three nitrogen atoms in the ring, and six signals in the EPR spectrum of **R9** due to hyperfine coupling to the two nitrogen atoms nearest to the electron.

Initial investigations were carried out with the radicals in MeCN with **C1**, to see whether any change in the EPR signal was observed, indicating that the radical had been bound to the cage structure. However, the results obtained showed no significant change in the EPR spectra to suggest evidence of binding. The spectra for **R8** and R9 are shown in Figure 54 and Figure 55 respectively.

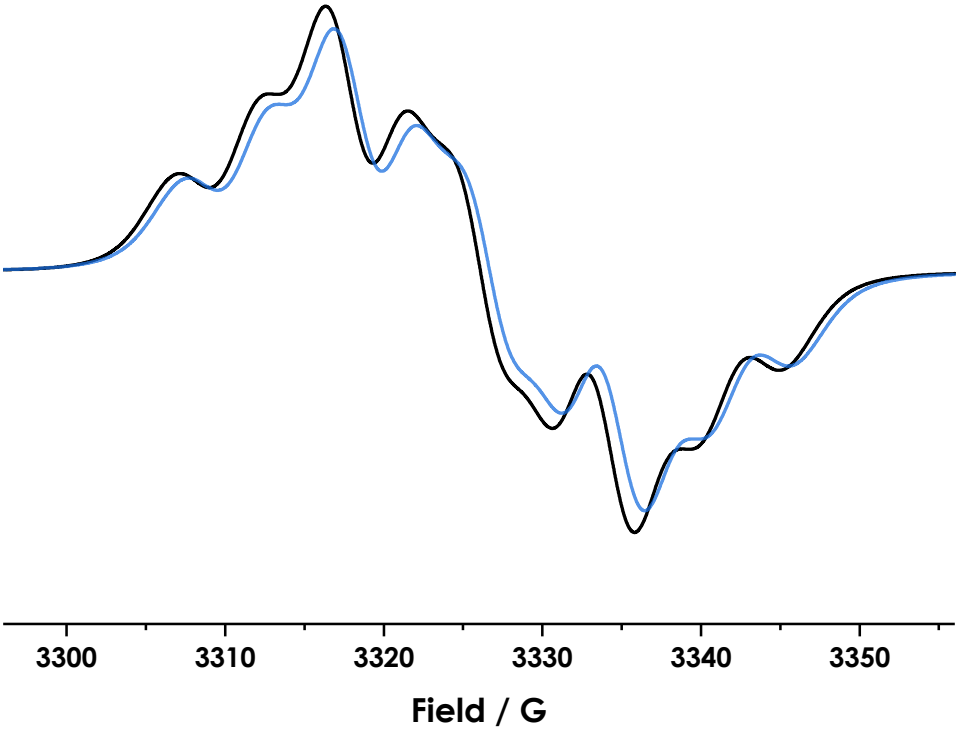

*Figure 54 - EPR spectra of 5×10^{-3} M **R8** (black) and 5×10^{-3} M **R8** + 5×10^{-4} M **C1** (blue) in MeCN.*

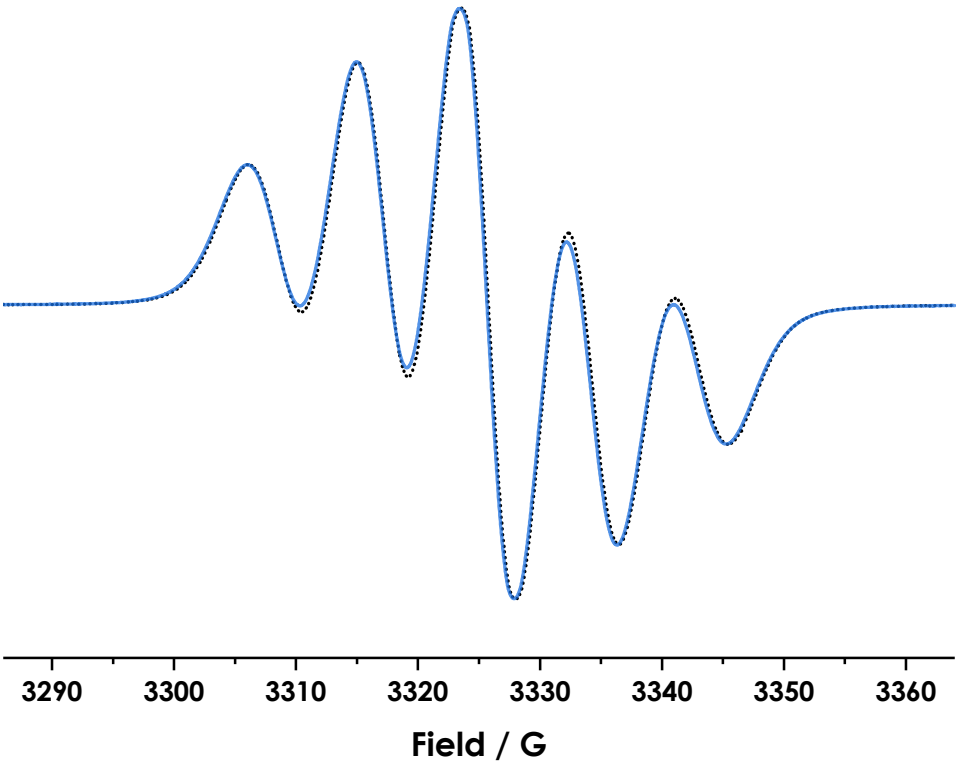

*Figure 55 - EPR spectra of DPPH (**R9**) (dotted, black) and **R9**+**C1** (blue).*

3.8.2 **R8** and **R9** in H_2O

Similar investigations were attempted adding the radicals to **C3** in H_2O. In this case, since neither of the radicals themselves were soluble in H_2O, the theory was that binding to the cage may allow the radicals to become soluble, leading to a colour change of the solution, and hence confirming binding. Unfortunately, no significant colour changes were observed upon addition of radical to aqueous cage solution, nor after subsequent sonication or centrifugation to remove the aggregated radical particles from solution. EPR spectra of the supernatant revealed only broad single peaks, corresponding to low concentrations of aggregated radical in the solution.

A possible avenue of future investigation with these radicals and cage structure would be to use a multi-solvent system, such as an MeCN/H_2O combination. The solubility of the radical in such a solvent system would be increased due to the addition of MeCN, and by varying the ratio of MeCN:H_2O such that the radical was only just soluble, it may be possible to investigate binding that would not be impeded by aggregation of insoluble particles. Initial investigations were started to explore this possibility but were not pursued further due to time constraints.

3.8.3 Synthesis of cage in presence of **R8**

As mentioned previously, these radicals were larger than might feasibly be expected to pass through the portals of the cage, and so an alternative investigative route was to encapsulate the radical during the self-assembly of the cage. This route was attempted with **R8**.

The procedure involved synthesising **C1** by the same method as described in Section 6.2.3, using $Cd(ClO_4)_2 \cdot 6H_2O$ (7.56 mg, 18.03×10^{-3} mmol) and **L1** (12.85 mg, 28.97×10^{-3} mmol) but additionally including an amount of **R8** (1.68 mg, 5.13×10^{-3} mmol) in the reaction mixture. During the reaction a colour change was observed in the reaction solution, from deep red to green. Characterisation of the resulting product using NMR spectroscopy revealed that the cage appeared to have been synthesised, but EPR spectroscopy did not show the expected signal for **R8**, and it was suspected that **R8** was being converted into another Blatter-Type radical (**R10**), structure shown in Figure 56.

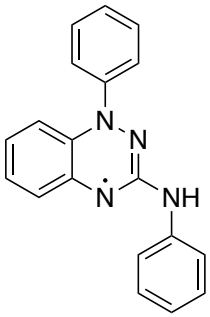

*Figure 56 - Structure of Blatter-Type radical (**R10**).*

3.8.4 Conversion of **R8** to **R10**

After further investigation, it was discovered that the conversion was being promoted by the $Cd(ClO_4)_2 \cdot 6H_2O$ starting material and MeOH solvent. The conversion was monitored by UV-Vis spectroscopy over the course of 24 hours using a diluted solution of a mixture containing the Cd salt, MeOH and **R8**. The UV-Vis spectra are shown in Figure 57.

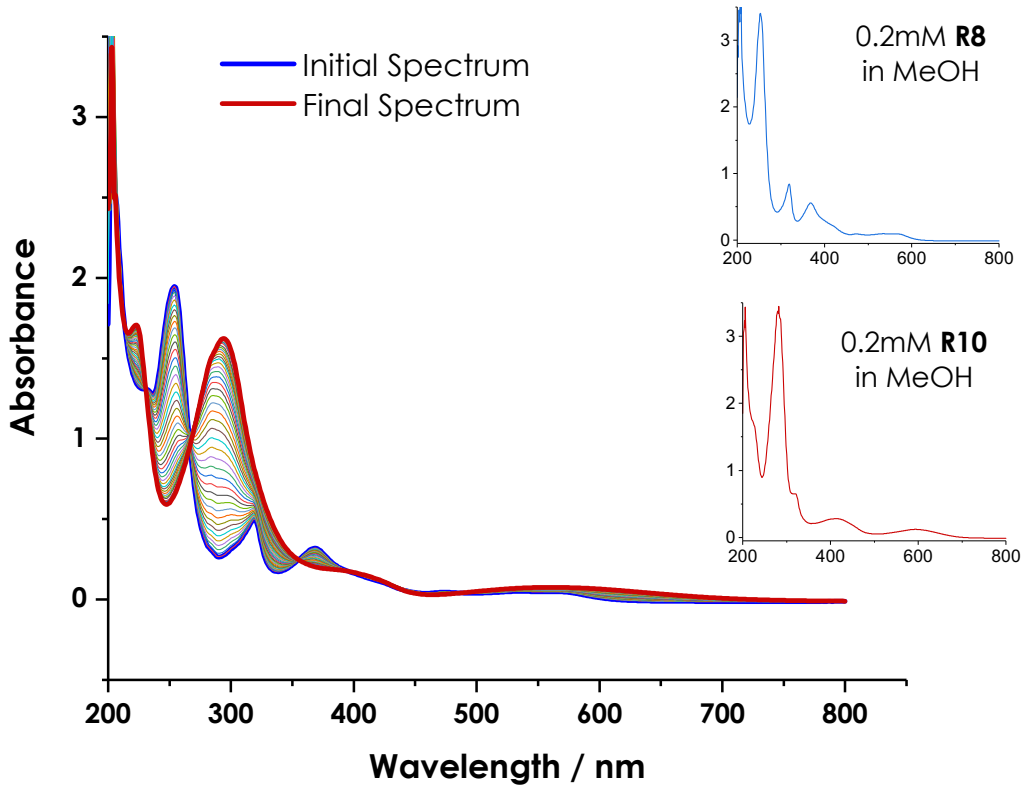

*Figure 57 - UV-Vis spectra of 0.08 M **R8** + $Cd(ClO_4)_2$ in MeOH. Spectra were recorded every 30 minutes, with the initial spectrum highlighted in bold, blue, and the final spectrum highlighted in bold, red. The UV-Vis spectra for **R8** and **R10** are inset for comparison.*

Previous literature[72] had shown that formation of (**R10**) was possible from (**R8**) under strongly basic conditions, and so it was presumed that this conversion was a sensible proposed

explanation for the colour change in solution, and the observed change in the UV-Vis spectra. Further investigation into this conversion was not carried out due to time constraints and the tangential nature of the investigation compared to the main aims of the project.

3.9 Conclusions

Of the radicals investigated in the initial binding studies it was found that the EPR spectra of nitroxides **R2**, **R3** and **R4** showed convincing evidence of binding, making them suitable for further investigation. The use of competing guests appeared to be successful in confirming binding effects, whilst also confirming the presence of Heisenberg exchange effects in studies with the Co cage **C3**, and dimerisation effects of the radical-containing carboxylic acids **R3** and **R4**. Radicals with volumes much larger than 55 % of the volume of the cavity of the cage did not appear to successfully bind, suggesting that none of these radicals chosen had any features that would enhance binding to overcome their undesirable size, or that the portions of radical that may have been able to bind could enter the cage cavity. Whilst not directly related to the binding studies, the discovery of conversion of Blatter-Type radical **R8** to **R10** in the presence of $Cd(ClO_4)_2 \cdot 6H_2O$ and MeOH was interesting, and may be worth investigating further to understand more fully the driving force and mechanism of conversion.

4 Quantitative binding studies of stable radical guests in supramolecular cages

From the initial binding explorations carried out, three radical@cage complexes were chosen for more in-depth binding studies. 4-oxo-TEMPO (**R2**) was chosen for investigation into binding with **C3** in H_2O, whilst 4-carboxy-TEMPO (**R3**) and 3-carboxy-PROXYL (**R4**) were used for binding studies with **C1**. These radicals were chosen as they showed the strongest evidence of binding in the initial studies, with distinct differences between the spectra for radical with and without cage added, and binding confirmed with addition of competing guests. Although all three were nitroxides, the slight variation in functional group between the two TEMPO derivatives allowed investigation into the H_2O-soluble and MeCN-soluble cages for comparison, whilst keeping the carboxy functional group the same, but varying between TEMPO and PROXYL derivative allowed investigation into the effects of ring-size and radical rigidity on binding effects and environment.

The aim of the detailed binding studies with these radicals was to determine more about the binding environment of the radicals within the complex, how the motion of the radical was affected and how strongly the radicals were bound, both qualitatively and quantitatively. This was to be achieved by performing titrations of the radical, keeping cage concentration constant, and observing any change in hyperfine values, calculating association constants, and using simulated parameters to investigate the rotational diffusion of the radicals, comparing bound and unbound radical guest.

4.1 4-oxo-TEMPO@**C3** in H_2O

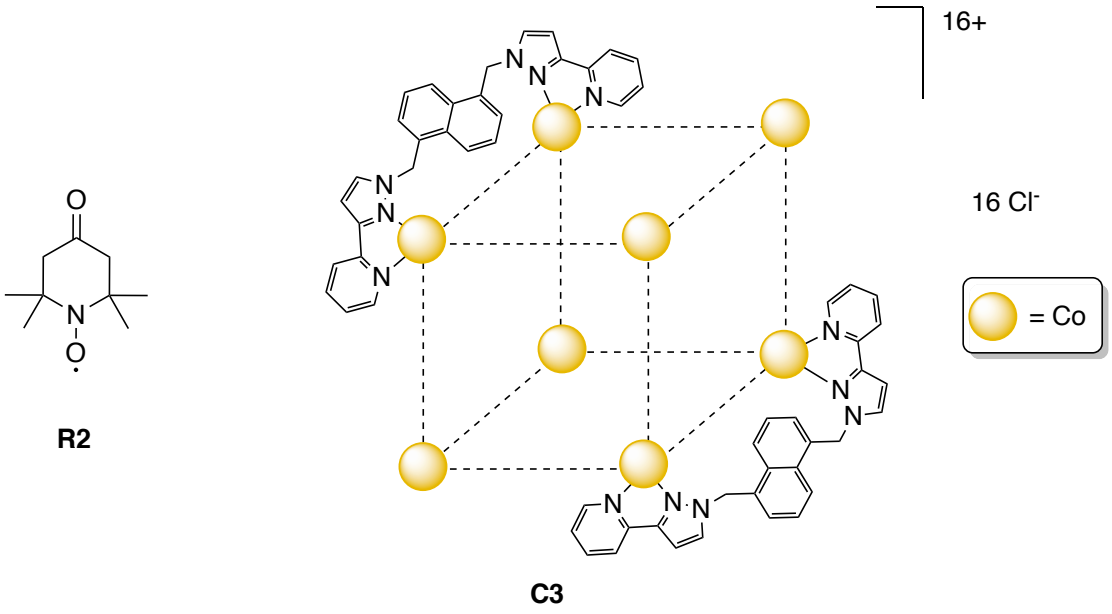

*Figure 58 - Structure of 4-oxo-TEMPO **(R2)** and diagram of cage **C3**, showing two of the twelve ligands, metal is Co and counterion is Cl^-.*

4.1.1 Titrations of **R2**

After binding had been confirmed in the initial studies, additional concentrations of radical **R2**, were prepared, in order to provide a number of data points that could be used to quantitatively analyse the binding equilibrium of the radical@cage complex and determine the strength of binding. Stock solutions of radical were prepared at additional concentrations of 1×10^{-4} M, 8×10^{-5} M and 2×10^{-5} M and, as previously, equal volumes of radical solution and either neat H_2O or cage solution were combined, to give samples with radical concentrations of 5×10^{-5} M, 4×10^{-5} M and 1×10^{-5} M in addition to the 2×10^{-5} M sample. The samples were then transferred to capillaries and EPR spectra recorded.

4.1.2 Simulation of **R2@C3**

The experimental spectra obtained showed evidence of two components, both in the fast motion regime, but with one sharper and the other broader, contributing to the overall spectra. Using EWVoigtN[54], the two components could be simulated well. First, an unbound component was simulated using parameters taken from simulations of solution of radical with no cage added. This allowed sensible parameters for the unbound component to be obtained, which could then be fixed, and a second component added to allow simulation of the bound component. Once a good fit had been obtained all parameters were allowed to vary slightly to improve the final fit of the simulation to the experimental spectrum. This provided confidence that the parameters used to simulate each component were sensible, showing that the inclusion

of two components was sufficient for good quality simulation of the spectrum and that assignment of each component to unbound and bound radical was reasonable. These components are shown in red and blue respectively in Figure 59 for radical at 2×10^{-5} M concentration. Spectra for the other concentrations may be found in the Appendix 7.3.1.

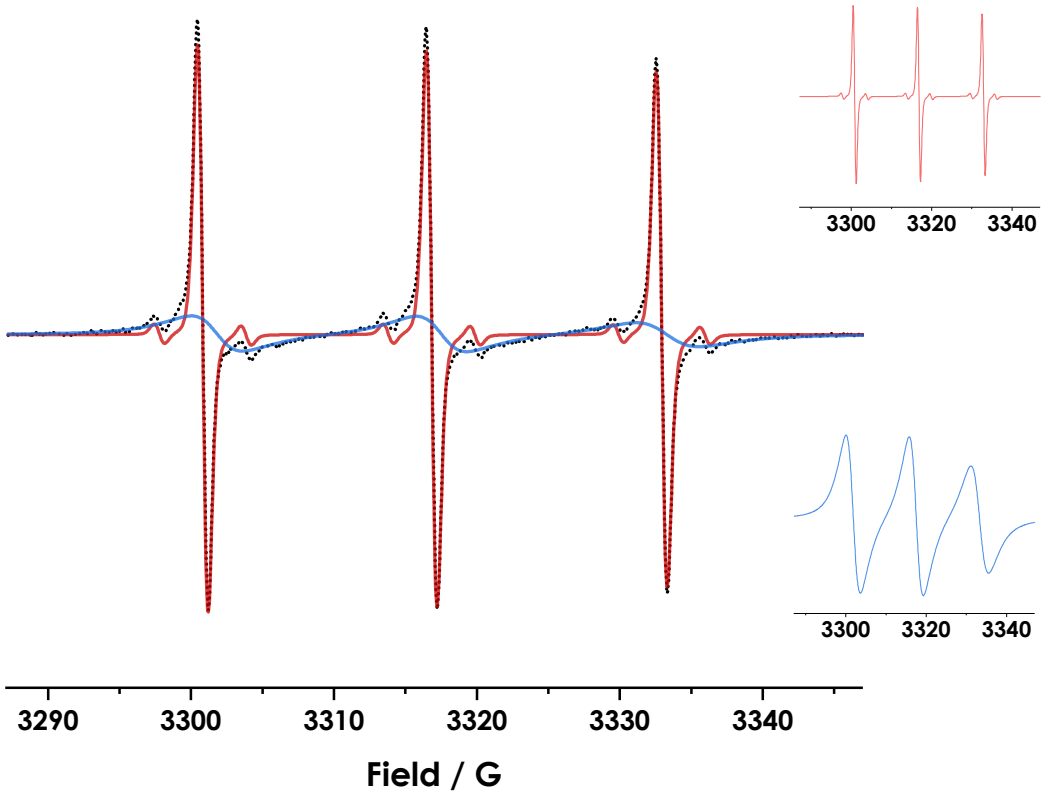

*Figure 59 - EPR spectrum of 2×10^{-5} M 4-oxo-TEMPO@**C3** in H_2O (black, dotted) overlaid with simulated components overlaid (red, unbound component; blue bound component). The two components are also inset to highlight the difference in lineshape.*

The unbound component shows three sharp signals, as expected for fast motion regime, whilst the bound component shows clear evidence of restricted motion, with signals that are far broader, but still in the fast motion regime.

Each concentration was simulated individually to obtain the best-fit parameters for the experimental spectra. The Lorentzian and Gaussian broadening parameters and the nitroxide hyperfine parameters from these best-fit parameters were then averaged for each component. These parameters are shown in Table 1.

*Table 1 - Averaged parameters for the simulations of **R2@C3** spectra.*

Unbound Component Parameters				
Lorentzian (1) / G[a]	**Lorentzian (0) / G[b]**	**Lorentzian (-1) / G[c]**	**Gaussian / G[d]**	**Nitroxide Hyperfine / G[e]**
0.18	0.19	0.22	0.64	16.03
Bound Component Parameters				
Lorentzian (1) / G[a]	**Lorentzian (0) / G[b]**	**Lorentzian (-1) / G[c]**	**Gaussian / G[d]**	**Nitroxide Hyperfine / G[e]**
3.73	3.68	4.50	0.14	15.74

[a] Contribution of the Lorentzian to the linewidth of the $m_I = 1$ peak, [b] the $m_I = 0$ peak, [c] the $m_I = -1$ peak in the EPR spectrum, in Gauss. Each was determined directly by EWVoigtN, based on a least-squares fitting of the simulated spectrum to the experimental spectrum. The simulated spectrum is a convolution of a Lorentzian lineshape function with a Gaussian envelope function, and additional envelope functions such as isotropic hyperfine interactions.
[d] Contribution of the Gaussian envelope function in Gauss, determined directly by EWVoigtN.
[e] Isotropic hyperfine contribution to the spectrum, in Gauss, determined directly by EWVoigtN.

Since the environment of both unbound and bound radical should remain the same, regardless of the concentration of radical, the shape of the unbound and bound components should also remain constant, provided no spin-broadening mechanisms are affecting the linewidths. This assumes that the spectra are not affected by any binding kinetics, and since no trends were observed in the EPR spectra upon changing the concentrations, with any differences within experimental error, it was assumed that binding was slow on the EPR timescale, and hence the values could be averaged. This provided an alternative to globally fitting the spectra directly, and also reduced the effect of experimental error between samples.

The parameters from Table 1 were fixed, and the spectra resimulated using these fixed values, whilst the scaling factor for each component was allowed to vary. The goodness-of-fit of the simulations to the experimental spectra were monitored by the chi-squared value to ensure the average parameters used were reasonable. From these new simulations, the new scaling factors were extracted, which could be assigned to the proportion of radical that was bound and unbound within the solution. This allowed the ratio between the two components to be calculated.

4.1.3 Determination of association constant

Since the cage was always in excess in these investigations, association constants could be determined using Equation 3, where [*R*@*C*] is the concentration of bound radical and cage complex, [*R*] is the concentration of unbound radical, the ratio of which may be defined by the ratio of their simulated scaling factors, and where [*C*] is the concentration of cage.

$$K = \frac{[R@C]}{[R]} \times \frac{1}{[C]}$$

Equation 3 - Calculation of association constant K, from ratio of simulated scaling factors and cage concentration.

The results of the calculations for each radical concentration are shown in Table 2.

Table 2 - Simulated scaling factors, bound/unbound ratio and association constant, K, calculated for each radical concentration.

Guest Conc. / 10^{-5} M	Unbound Guest Scaling / 10^{-3}	Bound Guest Scaling / 10^{-3}	Bound/Unbound Ratio	K / 10^{3} M^{-1}
1.00	0.838	3.63	4.33	**8.59**
2.00	1.74	7.13	4.10	**8.13**
4.00	4.17	15.2	3.65	**7.23**
5.00	4.61	18.2	3.95	**7.83**

By averaging the K values obtained, an overall association constant of K = 7.9±0.3 $\times 10^{3}$ M^{-1} could be determined. This value was compared to those of some previously studied guests, with a similar H_2O-soluble Co cage $[Co_8(C_{29}H_{25}N_6O_2)_{12}][BF_4]_{16}$, (where the ligand was functionalised with an OH group to allow solubility)[66], shown in Figure 60.

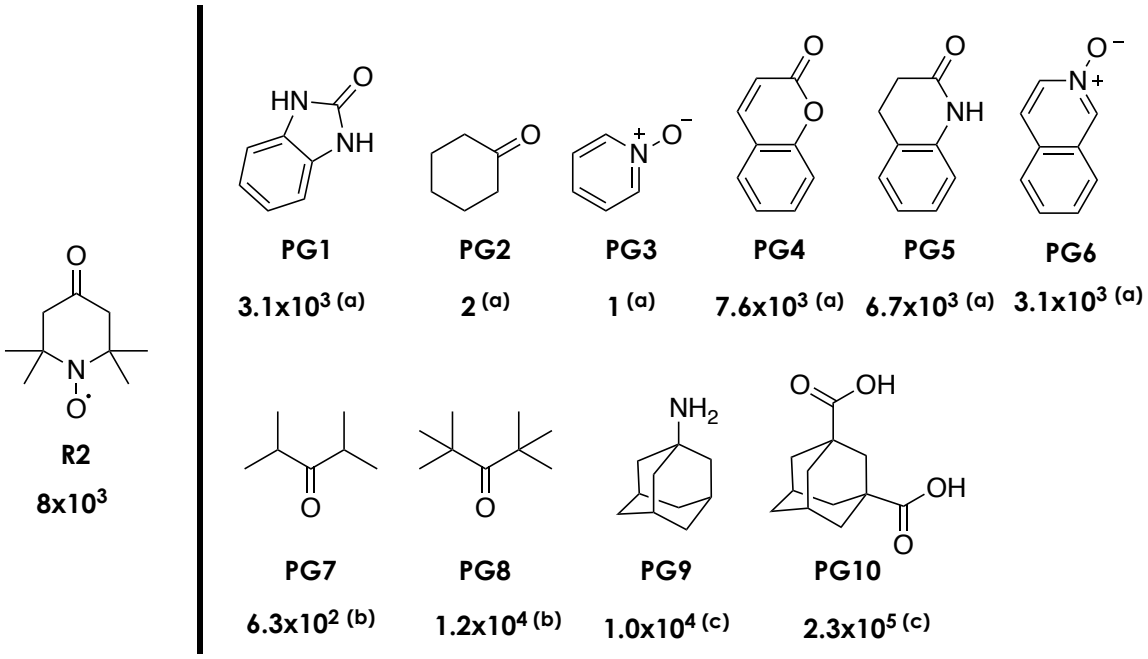

*Figure 60 – Structure of **R2** and previous guests (**PG**s) studied with H_2O-soluble Co cage (modified ligand) reported by Ward and co-workers.[66] Association constants are shown below each structure, in M^{-1}. [(a)]from reference.[66] [(b)]from reference.[67] [(c)] from reference.[73]*

Comparison of the association constant values suggests that the binding ability of **R2** is enhanced compared to **PG2** and **PG3**, possibly due to increased size filling the cage cavity more

completely, as well as the presence of both the carbonyl and nitroxide groups acting as potential H-bond acceptors, in comparison to the single H-bond acceptor nature of these guests. This is supported by the similar association constants for **PG4** and **PG5**, which have both the carbonyl group and the fused aromatic ring that can act as H-bond acceptors. For the guests **PG8**-**PG10**, the association constant was larger than that obtained for **R2**. This is likely due to the more favoured geometry of these guests compared to the radical **R2**, as well as the stronger H-bond acceptor nature of the guests, and the greater degree of desolvation they experience when going from free solution to cage cavity. As a result, it would appear that **R2** has an intermediate binding affinity for the cage **C3** in H_2O compared to other previously studied guests.

Comparison to the investigation by Ayhan et al.[36] of 4-oxo-TEMPO with the resorcinarene developed by Rebek et al., in water shows that the association constant obtained in this work is of the same order of magnitude as the 1:1 guest@cavitand complex, $K_a = 4.4\times10^3$ M, suggesting that the binding inside the two supramolecular capsules is comparable.

4.1.4 Characterisation of binding environment

Previous studies[43,74,75] into how solvent polarity affects the nitrogen hyperfine splitting parameters of radicals have found the hyperfine value increases with solvent polarity in general, due to the solvent environment influencing the distribution of spin density in the N-O bond. Using these prior observations, the difference in hyperfine values obtained for the unbound and bound components of the **R2**@**C3** spectrum (unbound: 16.03 G, bound: 15.73) suggests that the bound radical experiences a slightly less polar environment than the unbound radical. In this case, this would appear to indicate that the cavity of the cage is less polar than water. It is important to note that the change in hyperfine value is only ~0.3 G, and so drawing this conclusion from the data here alone is not necessarily reliable. However, previous work by Whitehead et al.[66] found that with the H_2O-soluble cage, $[Co_8(C_{29}H_{25}N_6O_2)_{12}][BF_4]_{16}$, the solvent provided a better H-bonding environment than the internal cavity, and thus likely provided a more polar environment, therefore supporting the conclusions.

4.1.5 Molecular motion within the cage

Due to the size of the cage, it was expected that the tumbling rate of the cage itself would be slow on the EPR timescale (10^5-10^{11} s), meaning that the broad component of the spectrum would correspond to the motion of the radical inside the cage. By comparing the rotational diffusion rate of the unbound and bound components, it would be possible to show that binding of the radical was restricting its motion. To calculate the tumbling rate, EasySpin[49] was used

to simulate the components, using the *garlic* function for the fast-motion, unbound component, and the *chili* function for the bound, more restricted-motion component. EasySpin was used at this stage due to the complexity of the spectrum analysis required, including both the effects of restricted motion and exchange parameters, which could not be separated using EWVoigtN.

To simulate the spectra in this way, A- and g-tensor values were taken from a paper by Azarkh and Groenen[76] for a frozen solution of 4-oxo-TEMPO in aqueous glycerol. Ideally, a frozen solution of the radical in pure H_2O would have been recorded first-hand to obtain these values. However, this would require freezing the solution very rapidly, to avoid aggregation of the radicals, and it was not possible to obtain a good enough spectrum from which the required values could have been calculated from. The values taken from the paper were g = [2.0083 2.0058 2.0030] G, and A = [18 18 99] MHz.

Using these values, the fast-motion component was first simulated to obtain the linewidth values, which included the Lorentzian and Gaussian broadening effects. These values were then fixed and used to simulate the more restricted-motion component, whilst the rotational diffusion parameters were varied to account for broadening due to restricted motion. The results of this simulation are shown in Figure 61.

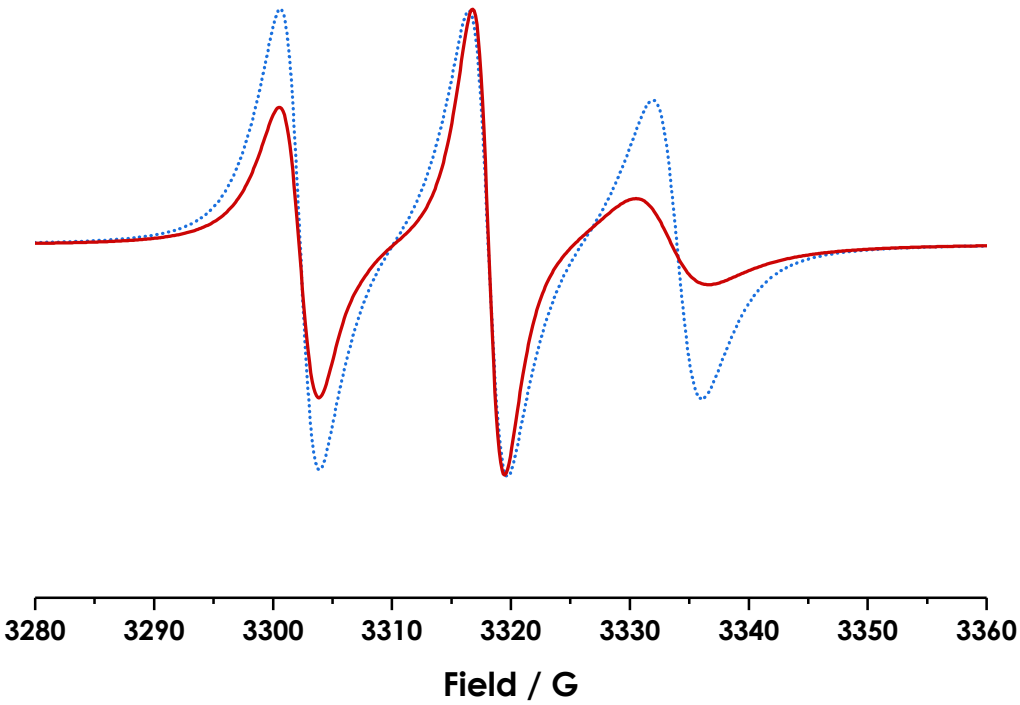

*Figure 61 - Slow motion component of 2x10^{-5} M **R2**@**C3** solution (blue, dotted), overlaid with simulation where linewidth and A- and g-values were fixed and rotational diffusion parameters allowed to vary (red, solid).*

It was at this stage that further evidence of the Heisenberg exchange effect was confirmed, as simulations which did not include an exchange parameter (as above) did not converge to a good fit, and only if the linewidths were allowed to vary could a better fit be obtained. In contrast, including a Heisenberg exchange parameter (at a value of 7.54 MHz in this case) provided a much better fit when the simulation was allowed to converge, as shown in Figure 62.

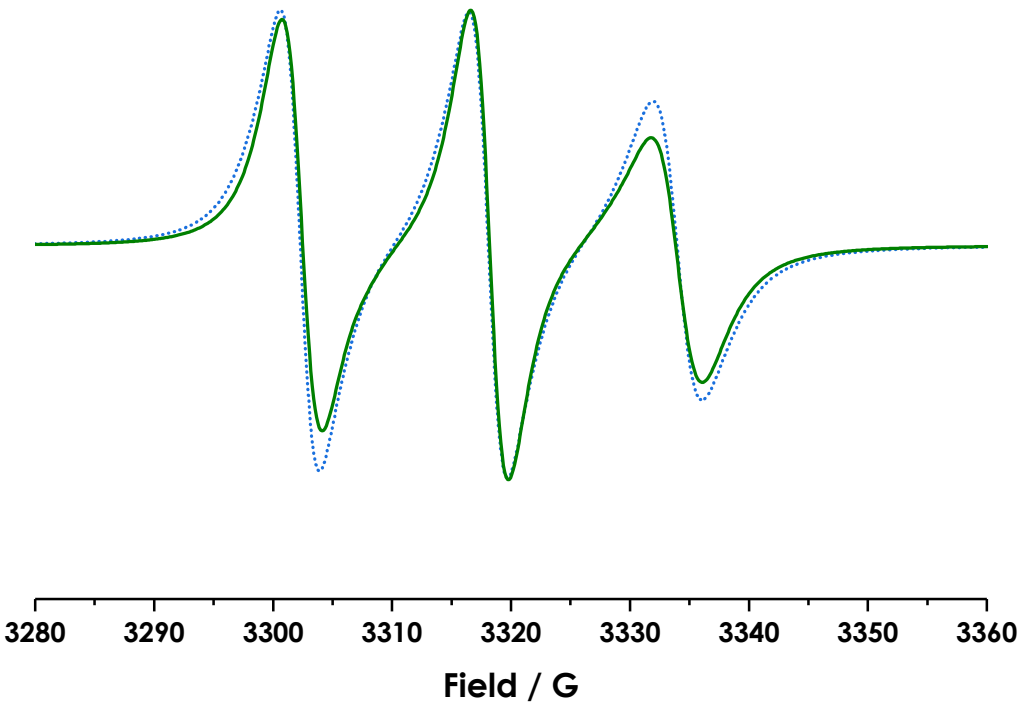

*Figure 62 -Slow motion component of 2x10^{-5} M **R1**@**C3** solution (blue, dotted), overlaid with simulation where linewidth and A- and g-values were fixed and rotational diffusion parameters allowed to vary, and an exchange parameter of 7.54 MHz was also included (green, solid).*

This also confirms that the broadening effect of Heisenberg exchange is stronger when the radical is bound, as would be expected since the cobalt atoms will be fixed in position closer to the radical, meaning exchange is more frequent, than when unbound in free solution.

From the simulation of the slow component, the tumbling rate of the radical inside the cage could be calculated as $D_{xy} = 2.44\times10^{8}$ s^{-1} and $D_z = 3.98\times10^{5}$ s^{-1}, slower than the isotropic diffusion tensor of $D = 9.52\text{x}10^{9}$ s^{-1} calculated for the unbound component. To interpret these values, it is necessary to consider the orientation of the magnetic and diffusion axes for the molecule, and the relation between them. For nitroxides the magnetic z-axis is taken to be perpendicular to the N-O bond, with the x-axis parallel. Since the nitroxide is attached to the cage, it may be approximated as a rigid rod, with one end fixed to the cage, and the other terminating with the N-O bond. The rotational diffusion of this rod can be assumed to have axial symmetry, and so the rotational diffusion axes may be defined as $D_{\|}$ and $D_{\perp}$ where the angle between $D_{\|}$ and the magnetic z-axis is defined by β_D. In the simulations in this work, $\beta_D = 90°$, and so the $D_{\|}$ axis is parallel to the N-O bond. Diagrams showing the orientation of the axes are given in Figure 63.

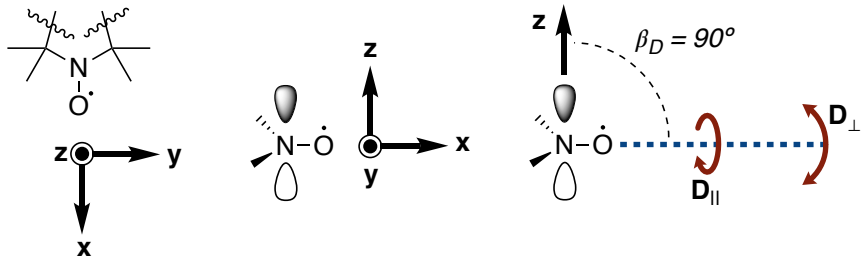

Figure 63 - Diagrams showing the orientation of the magnetic axes for nitroxides in this work: Top view (left), side view (centre), and diagram showing rotation about the diffusion axes, where angle between the magnetic z-axis and $D_{\|}$, given by β_D, is 90° (right). $D_\perp$ is perpendicular to $D_{\|}$.

Based upon these axis systems, the rotational diffusion parameter D_z corresponds to $D_{\|}$, whilst the D_{xy} parameter corresponds to $D_\perp$, and hence $D_{\|} = 3.98\times10^5$ s^{-1} and $D_\perp = = 2.44\times10^8$ s^{-1}.

In order to determine whether these values are reasonable, it is sensible to compare to previous values obtained for similar studies with other supramolecular assemblies. Figure 64 shows the structures of some such assemblies, reported by Ionita et al.[32] and Garel et al.[38] alongside the structures of some TEMPO derivatives that were used as guests for these structures. Table 3 shows the rotational EPR parameters for the unbound and bound guests with these structures.

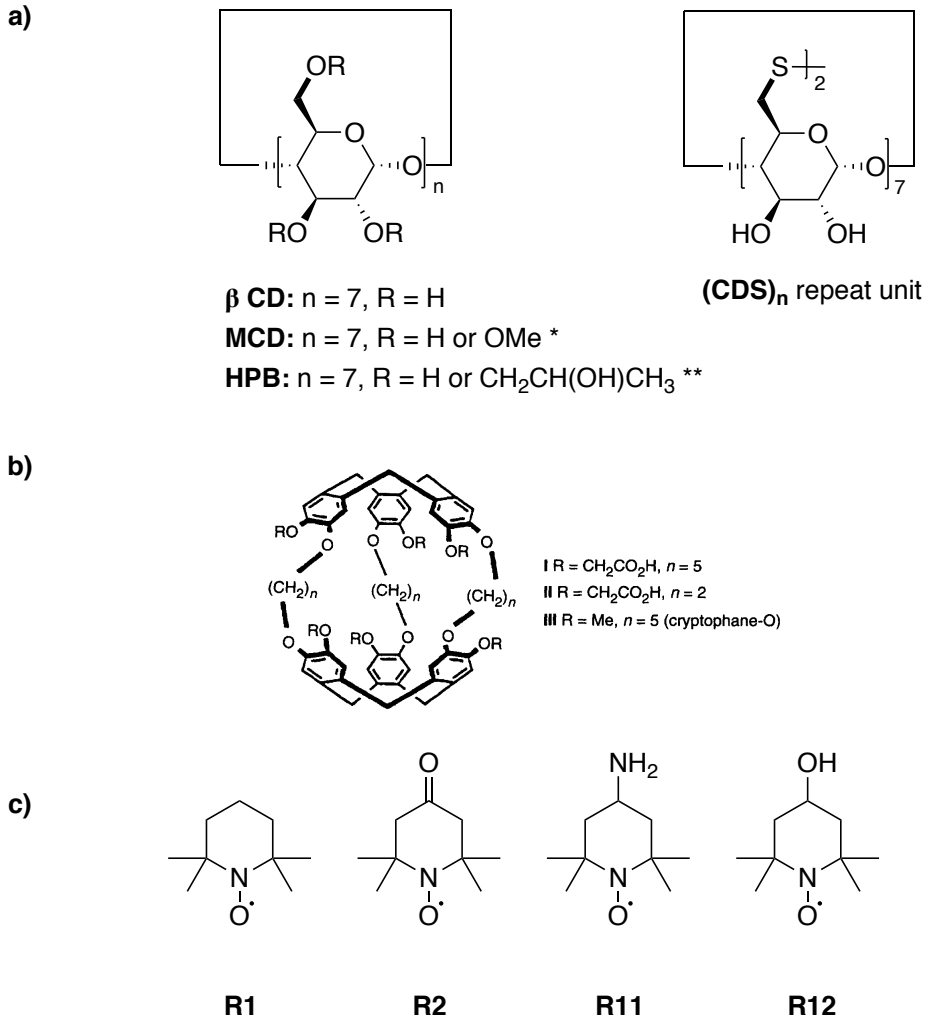

*Figure 64 - a) Structures of the functionalised cyclodextrins (CDs), **β-CD**, hydroxypropyl-β-CD (**HPB**), methyl β-CD (**MCD**) and polymeric β-CD-based, disulfide-crosslinked nanocapsules **(CDS)$_n$** studied by Ionita et al.[32] *(Avg. M_W =1310) ***(Avg. M_W =1460) b) Structure of the cryptophane studied by Garel et al. Adapted from Ref.[38] with permission from The Royal Society of Chemistry. c) Structures of the radicals TEMPO (**R1**), 4-oxo-TEMPO (**R2**), 4-amino-TEMPO (**R11**), 4-hydroxy-TEMPO (**R12**).*

Table 3 - Rotational correlation constant values, τ_c, and equivalent rotational diffusion parameters, D. (a) Data from reference[32] (b) Data from reference.[38] All parameters calculated for guest and host-guest complexes in H_2O.

Host Structure	Radical	Unbound		Bound	
		τ_c / 10^{-10} s	D / 10^9 s^{-1}	τ_c / 10^{-10} s	D / 10^8 s^{-1}
β-CD[a]	**R1**	0.63	2.64	0.84	19.8
HPB[a]				1.60	10.4
MCD[a]				1.36	12.3
(CDS)$_n$[a]				7.82	2.13
Cryptophane I[b]	**R1**	0.25	6.67	5.05	3.30
	R2	0.22	7.58	3.95	4.22
	R11	0.35	4.76	5.68	2.93
	R12	0.33	5.05	6.50	2.56

From comparison with these previous studies, it can be observed that the unbound component rotational diffusion parameters are similar to those obtained in this work, all having the same order of magnitude (10^9 s^{-1}). This suggests that the simulations of the fast-motion component of the spectra are good, and the parameters reliable, since as the solvent used is H_2O in all cages, the values would be expected to be similar.

In these papers, only one value is reported for the bound, slow-motion component, with most on the order of magnitude 10^8 s^{-1}. This matches well with the value obtained for the D_{xy} rotational diffusion value of 2.44×10^8 s^{-1}. As is noted in the paper by Ionita et al.,[32] the host-guest complexes of **β-CD**, **HPB**, and **MCD** show faster tumbling rates (smaller τ_c, larger D values) than the radical bound to **(CDS)$_n$**, and the radical-host complexes reported by Garel et al.[38] This is attributed to the contribution of host tumbling effects for the former structures, whilst the polymeric nature of the **(CDS)$_n$** means that this tumbling is reduced and no longer detectable on the EPR timescale, meaning the rotational parameter recorded only results from the tumbling of the radical inside the CD, which is slower. Due to the larger size of the cryptophane structure, it is likely that the rate of tumbling will also be slow on the EPR, such that the only contribution will be from the tumbling of the radical inside the cavity. It is assumed that the same reasoning holds true for the cage **C3** studied in this work, and this would appear to be supported by the values obtained for the rotational diffusion rate.

However, the rotational diffusion parameter in the z-direction, $D_z = 3.98\times10^5$ s^{-1}, does not appear to match the order of magnitude expected. The reasons for this are unclear, since cw-EPR at X band is not sensitive to rotational diffusion below ~10^6 s^{-1}, and so it would appear that rotation about this axis is frozen on the EPR timescale, but that the value obtained is not necessarily reliable. If it is assumed that the main binding of the radical to the cage is through the carbonyl group, as illustrated in Figure 65, this would suggest that there may be a barrier to rotation about this axis.

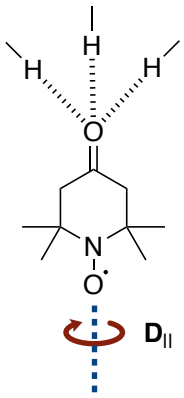

*Figure 65 – Diagram showing the carboxyl group of **R2** may be bound to the cage through H-bonding interactions. The principal diffusion axis, $D_{\|}$, and direction of rotation about this axis is shown.*

However, it is also important to note that the effects of Heisenberg exchange broadening the spectra may be leading to large errors in determining the anisotropic diffusion parameters, so it is hard to draw any definitive conclusions as to the validity of this value.

4.1.6 Conclusions

Simulations of the **R2@C3** spectra revealed that two components, an unbound and bound component, contributed to the spectra, and that both components were in the fast motion regime, with the bound component showing evidence of restricted motion as expected. This reduced rate of tumbling was determined quantitatively through simulation of the two components, with the rotational diffusion rate of the unbound component calculated as 9.52×10^{9} s^{-1}, and the bound component rotational diffusion rate defined by the axial tensors $D_{xy} = 2.44 \times 10^{8}$ s^{-1} and $D_z = 3.98 \times 10^{5}$ s^{-1}. The former value appears to match well with previous literature studies of **R2** with a supramolecular assembly, whilst the latter value is likely unreliable. The association constant for **R2@C3** was calculated as 8×10^{3} M, and evidence was observed that supported the conclusion that the binding environment of the radical was less polar than H_2O.

4.2 4-carboxy-TEMPO@**C1** in MeCN

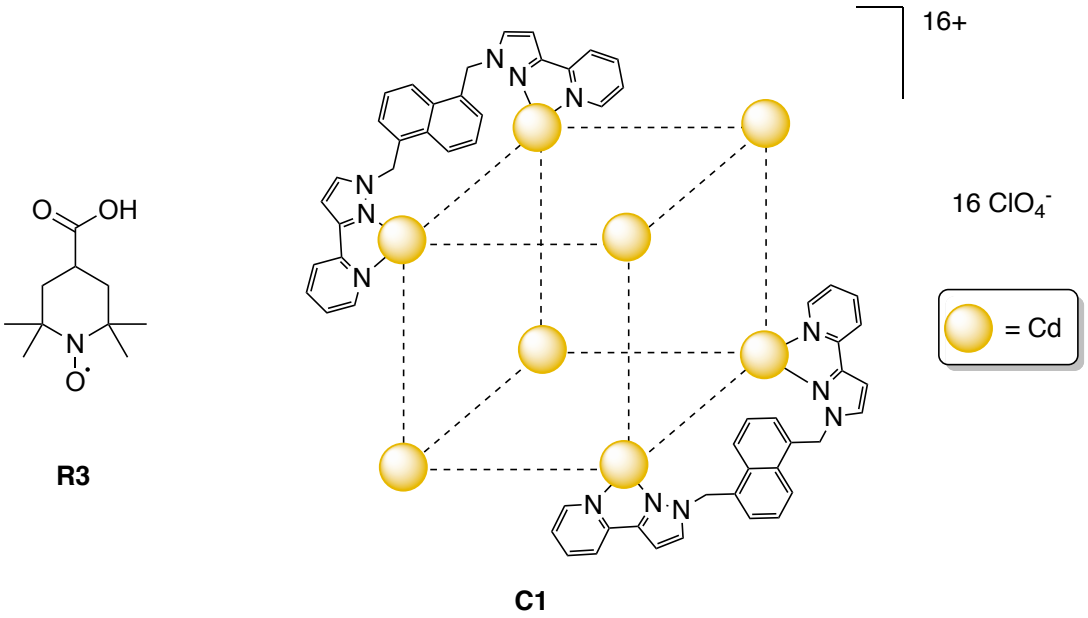

*Figure 66 - Structure of 4-carboxy-TEMPO (**R3**) and diagram of cage **C1**, showing two of the twelve ligands; metal is Cd and counterion is ClO_4^-.*

4.2.1 Titrations of **R3**

As with **R2,** stock solutions of radical were prepared at additional concentrations in order to again calculate binding constants and determine information about the binding environment using multiple data points. Solutions of radical at 1×10^{-4} M, 8×10^{-5} M and 2×10^{-5} M were prepared to give samples with radical concentrations of 5×10^{-5} M, 4×10^{-5} M and 1×10^{-5} M in addition to the 2×10^{-5} M sample. As described previously, (Chapter 3) the samples were transferred to sealed Pasteur pipettes and degassed with N_2 before EPR spectra were recorded.

4.2.2 Simulation of **R3@C1**

The spectra obtained for the **R3@C1** samples again showed evidence of two components, like for **R2@C3**. However, in this case the contribution from the bound component appeared more prominent, and the bound radical appeared to be more restricted in its motion. However, it was still possible to fit the spectrum well as a superposition of Voigtian peaks, with a constant peak-peak separation, corresponding to the hyperfine value between nitroxide peaks. Therefore it was assumed that simulating the spectra as two components in the fast-motion regime with EWVoigtN did not lead to unacceptably large errors. The spectrum and simulated components are shown in Figure 67 for radical at 2×10^{-5} M, and other concentrations are shown in Appendix 7.3.2.

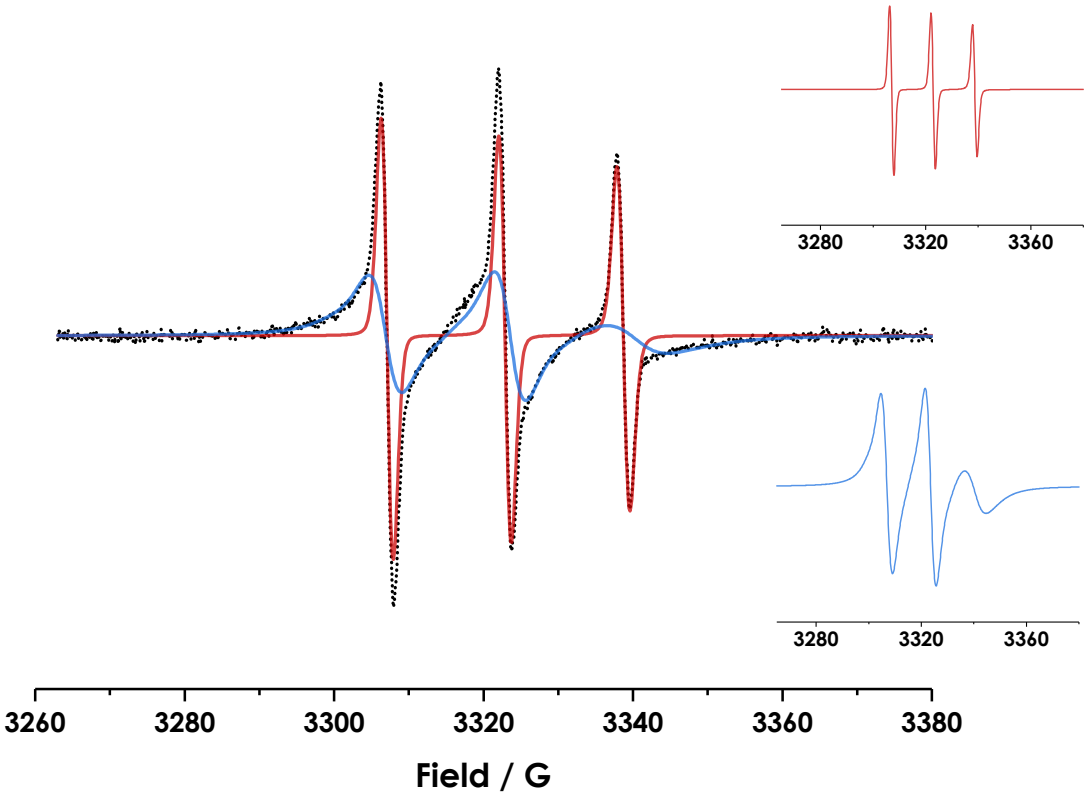

*Figure 67 – EPR spectrum of 2×10^{-5} M 4-carboxy-TEMPO@**C1** in MeCN (black, dotted overlaid with simulated components overlaid (red, unbound component; blue, bound component). The two components are also inset to highlight the difference in lineshape.*

The simulations confirmed that the bound radical was indeed more restricted in its motion than in the **R2@C3** complex, with the high-field peak showing a much lower intensity compared with the low- and mid-field, characteristic of increased anisotropy.

4.2.3 Determination of association constant

Again, the **R3@C1** solution spectra were simulated individually to obtain the best fit parameters, and the best averaged to give the parameters shown in Table 4. These parameters were used for the new simulations to calculate the scaling factors and ratio between the components. Association constants were calculated using Equation 3, with the values shown in Table 5.

*Table 4 - Averaged simulation parameters for **R2@C3**.*

Unbound Component Parameters				
Lorentzian (1) / G[a]	**Lorentzian (0) / G[b]**	**Lorentzian (-1) / G[c]**	**Gaussian / G[d]**	**Nitroxide Hyperfine / G[e]**
0.18	0.22	0.40	1.56	15.79
Bound Component Parameters				
Lorentzian (1) / G[a]	**Lorentzian (0) / G[b]**	**Lorentzian (-1) / G[c]**	**Gaussian / G[d]**	**Nitroxide Hyperfine / G[e]**
4.10	3.94	7.70	0.32	16.36

[a] Contribution of the Lorentzian to the linewidth of the $m_I = 1$ peak, [b] the $m_I = 0$ peak, [c] the $m_I = -1$ peak in the EPR spectrum, in Gauss. Each was determined directly by EWVoigtN, based on a least-squares fitting of the simulated spectrum to the experimental spectrum. The simulated spectrum is a convolution of a Lorentzian lineshape function with a Gaussian envelope function, and additional envelope functions such as isotropic hyperfine interactions.
[d] Contribution of the Gaussian envelope function in Gauss, determined directly by EWVoigtN.
[e] Isotropic hyperfine contribution to the spectrum, in Gauss, determined directly by EWVoigtN.

*Table 5 - Scaling factors and association constants for **R2@C3**.*

Guest Conc. / 10^{-5} M	Unbound Guest Scaling / 10^{-3}	Bound Guest Scaling / 10^{-3}	Bound/Unbound Ratio	K / 10^3 M^{-1}
1.00	1.38	5.66	4.10	**8.18**
2.00	1.61	8.94	5.55	**11.08**
4.00	4.15	1.91	4.60	**9.18**
5.00	5.07	2.06	4.06	**8.11**

The overall association constant for **R3** was then calculated as $9.2 \pm 0.6 \times 10^3$ M^{-1}. This value is slightly higher than that obtained for **R2@C3** ($7.9 \pm 0.3 \times 10^3$ M^{-1}) but is still of the same order of magnitude. Due to the large number of factors affecting the binding ability of the guest in the different solvents, for example the H-bond acceptor nature of the guest and solvent, the effect of desolvation of the guest molecules upon binding, and the effect of releasing bound solvent molecules, it is hard to draw any definitive conclusion as to what causes this slight increase. Future work including a larger data set would allow better quantification from which conclusions could be drawn.

However, comparison with previous guests studied with the MeCN-soluble cobalt cage, **C2** may be made. A selection of these guests are shown with their association constants in Figure 68.

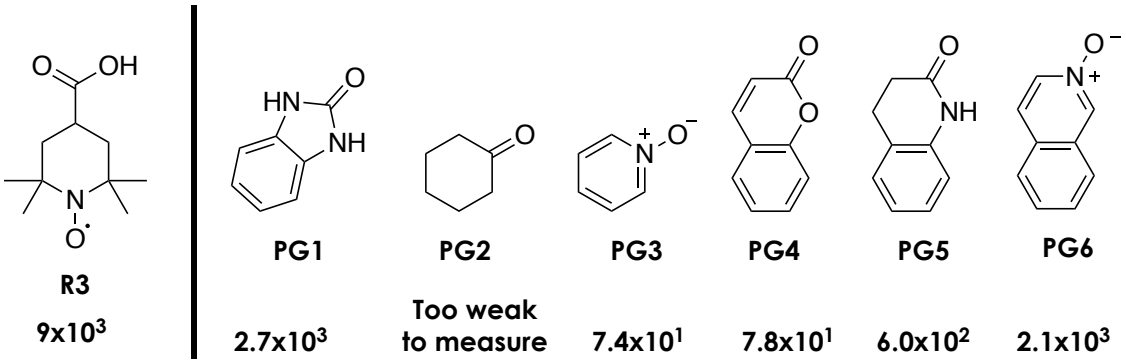

*Figure 68 - Structure of **R3** and previous guests (**PG**s) studied with MeCN-soluble Co cage reported by Ward and co-workers.[55] Association constants are shown below each structure, in M^{-1}. All **PG** data from reference.[66]*

The comparison to the previous guest association constants reveals that the radical **R3** binds significantly more strongly than **PG2**, which was found to bind too weakly to be measured by the NMR titration binding method employed by Ward and co-workers,[66] as might be expected due to the low H-bond acceptor ability of **PG2** in comparison. **PG3** and **PG4** have stronger binding, but still lower than for **R3**, whilst **PG1** and **PG6** are of the same order of magnitude (10^3 M^{-1}) but are still somewhat weaker than **R3**. This would appear to indicate that the inclusion of the carboxy functional group is sufficient to provide better binding interactions in the cage structure in MeCN. However, using the carboxylic acid does allow the possibility of binding through the metal centre, and as such the radical could be bound inside or outside the cage cavity, with no easy way to distinguish between these two possibilities.

4.2.4 Characterisation of binding environment

When considering the change in the hyperfine value between the unbound and bound component of the simulations in this system it was observed that the bound component hyperfine was larger than the unbound component, in contrast to the findings for **R2@C3**. This suggests that the binding environment in the **R3**+**C1** system is more polar than the environment for unbound radical. If radical is binding inside the cavity, this would suggest that overall the cavities of the cage structures are more polar than MeCN but less polar than H_2O. However, it is important to note that this change in hyperfine value may be an artefact arising due to the use of the fast-motion approximation, and as such the conclusions about the polarity of the environment are not necessarily reliable.

4.2.5 Molecular motion within the cage

As with **R2**, in order to calculate the tumbling rates of the unbound and bound radical, the EasySpin functions *garlic* and *chili* were used to simulate the fast- and slow-motion components of the spectra respectively. The A- and g-values needed for this were obtained by first

simulating a frozen spectrum of **R3**+**C1** in MeCN at 125 K using the *pepper* function of EasySpin. The experimental frozen spectrum and simulation are shown in Figure 69.

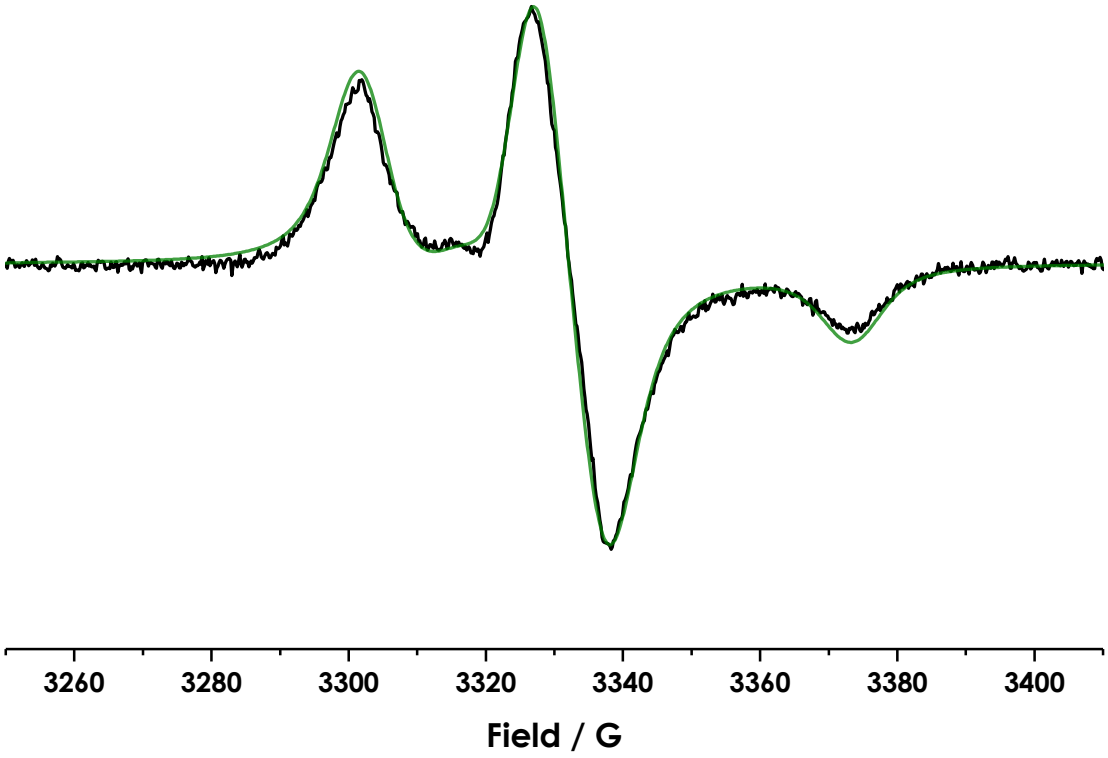

*Figure 69 - 5×10^{-5} M 4-carboxy-TEMPO (**R3**) + **C1** in MeCN at 125 K (black) overlaid with simulated spectrum (green)*

The values obtained from the simulation were g = [2.00807 2.00591 2.00138] G and A = [18 13 100] MHz. Using these values the components were simulated following a similar process as for **R2**, to calculate the rotational diffusion parameters, obtaining the linewidths from the fast motion component and then only varying the rotational diffusion parameters and the A_{zz} value to simulate the slow component. The slow component and simulation are shown in Figure 70

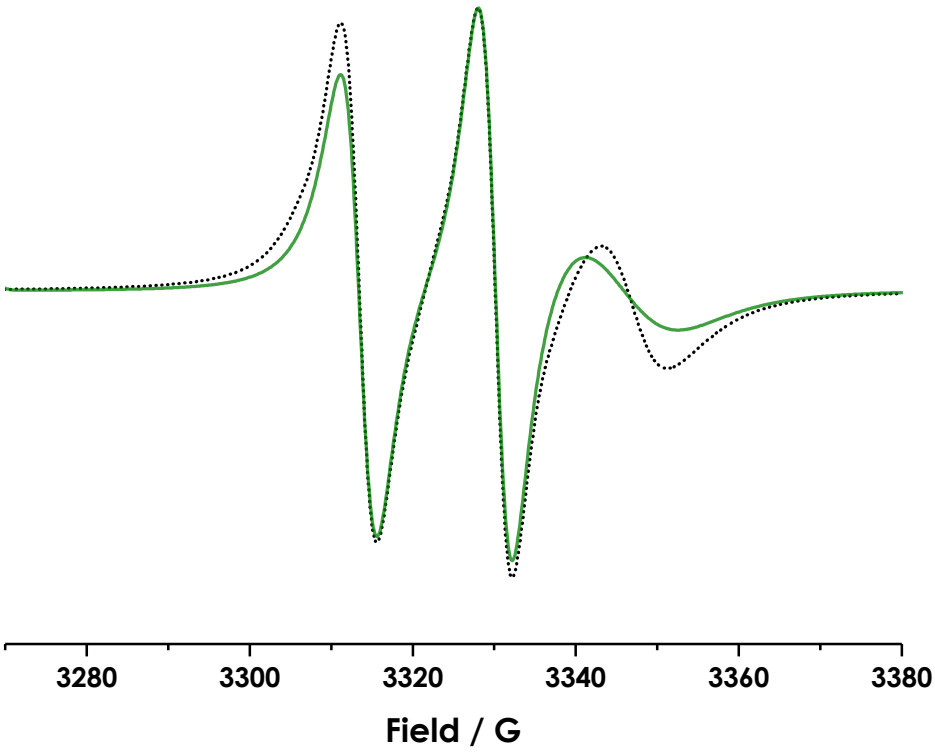

Figure 70 - Slow motion component of 2x10^{-5} M 4-carboxy-TEMPO + C1 in MeCN (black, dotted) overlaid with simulation (green)

Although the fitting of the simulation to the slow component is poor, since small changes in the value of the diffusion tensors leads to large changes in the simulated spectrum, the accuracy of the diffusion parameters is reliable, meaning conclusions can be drawn with reasonable confidence.

From these simulations, the unbound component diffusion rate was found to be $D = 2.34\times10^{9}$ s^{-1}, whilst the bound component diffusion rate was slower with $D_{xy} = 3.39\times10^{5}$ s^{-1} and $D_z = 1.63\times10^{8}$ s^{-1}. The unbound component value is similar to that of the TEMPO derivatives **R11** and **R12** studied with the hexameric resorcinarene capsule in water-saturated dichloromethane, reported by Mileo et al.[77] and shown in Figure 71.

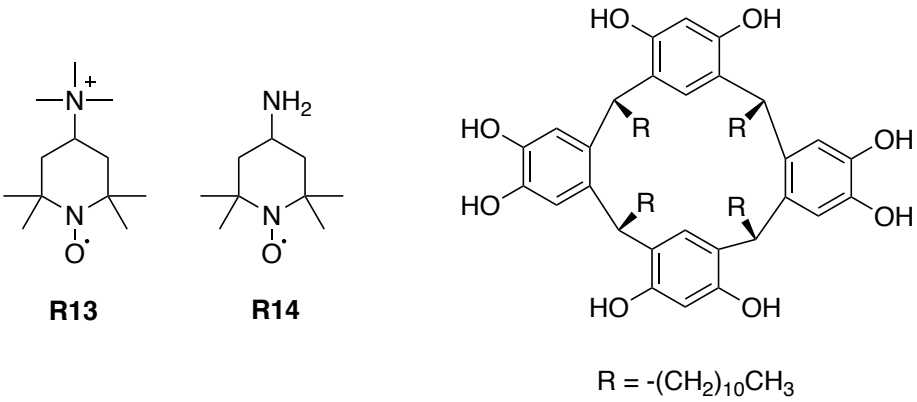

*Figure 71 - Structures of TEMPO-Me_3N^+ (**R13**) and 4-amino-TEMPO (**R14**) with the structure of the resorcinarene host reported by Mileo et al.[77] The resorcinarene host forms a hexameric structure to encapsulate the radical guests.*

These radicals had unbound isotropic values of D = 3.96×10^9 s^{-1} and D = 1.39×10^{10} s^{-1} for **R13** and **R14** respectively, which are similar to that obtained for **R3** in MeCN. The slight variations can be attributed to the different functional groups of the TEMPO derivatives, as well as the slightly different solvent properties. However, the viscosity of the two solvents are expected to be similar enough that tumbling rate should be comparable between them, and suggesting that the value obtained for unbound **R3** is reasonable.

When comparing the bound values, the literature reports only a single isotropic value for each, with D = 8.33×10^6 s^{-1} for **R13** and D = 1.28×10^8 s^{-1} for **R14**. These values show decreases in tumbling rate of a factor of 10^3, (~500 and ~100) respectively, whilst the decrease for **R3** when bound to **C1** is a factor of ~7000 for the D_{xy} component, and ~15 for the D_z component. The discrepancy between the two components may be explained by again considering the binding site of the radical inside the cage, and the orientation of the rotational diffusion axes. These are illustrated in Figure 72.

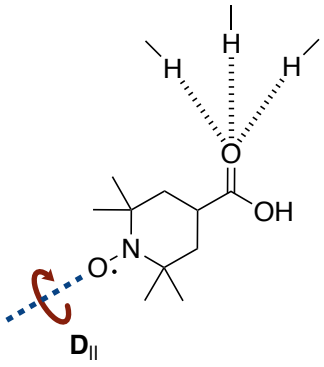

*Figure 72 - Diagram showing how the carboxy group of **R3** may be bound to the cage through H-bonding interactions. The principal diffusion axis, $D_{\|}$, and direction of rotation about this axis is shown.*

As described for **R2** in section 4.1.5, $D_z = D_{\|}$ and $D_{xy} = D_{\perp}$, and for **R3** bound through the carboxylic acid group, it would be expected that rotation about the $D_{\|}$ would be faster due to

possible rotation about the C-C bond connecting the carboxylic acid to the ring, suggesting that the 1.63×10^{8} s^{-1} is reasonable. However, the very slow value for D_{xy}, 3.39×10^{5} s^{-1}, again appears to suggest that rotation about this axis is frozen on the EPR timescale, and no significant conclusions can be drawn from this.

4.2.6 Conclusions

Simulations of the **R3@C1** spectra revealed that two components contributed, an unbound and bound component, and that whilst both components were again in the fast-motion regime, the bound component showed a greater level of restricted motion than for **R2**. The rotational diffusion parameter for unbound component was $D = 2.34\times10^{9}$ s^{-1} and for bound component were $D_{xy} = 3.39\times10^{5}$ s^{-1} and $D_z = 1.63\times10^{8}$ s^{-1}. The association constant obtained for the radical using the scaling factor ratios was calculated to be 9×10^{3} M^{-1}. The change in hyperfine coupling constant for the bound component compared to unbound suggested that the binding environment of the radical was more polar than MeCN. Whilst it is likely that the radical is bound inside the cage in this case, there is the possibility that the carboxy group may afford the radical ability to bind outside the cage. Unfortunately, the investigations here could not distinguish between the two possibilities. Although the diamagnetic nature of this cage could allow for some confirmatory NMR investigations to be attempted in future work to gain further insight, the large number of overlapping peaks in the spectrum for **C1** would likely make it difficult to observe any paramagnetic broadening of the spectrum that would arise due to the binding of radical **R3** to the cage.

4.3 3-carboxy-PROXYL@**C1** in MeCN

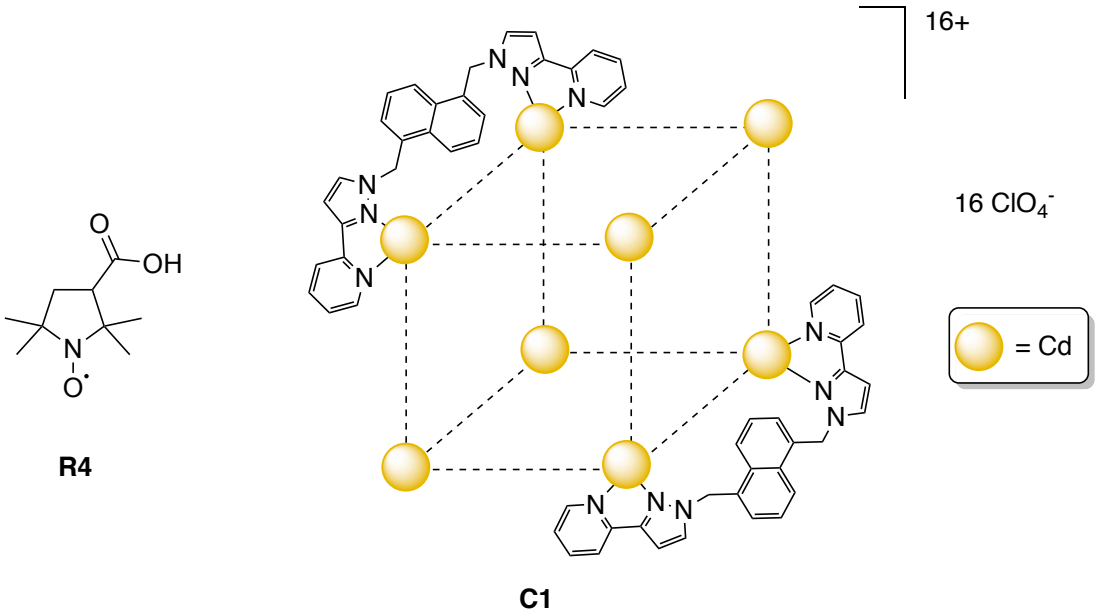

*Figure 73 – Structure of 3-carboxy-PROXYL (**R4**) and formula of **C1***

4.3.1 Titrations of **R4**

As previously, stock solutions of radical were prepared at additional concentrations of 1×10^{-4} M, 8×10^{-5} M and 2×10^{-5} M, to give samples with radical concentrations of 5×10^{-5} M, 4×10^{-5} M and 1×10^{-5} M in addition to the 2×10^{-5} M sample. The samples were transferred to sealed Pasteur pipettes and degassed with N_2 before EPR spectra were recorded.

4.3.2 Simulation of **R4@C1**

The spectra obtained for this complex again showed evidence of two components. This time the bound radical appeared to be even more restricted in its motion such that it could not be treated as being in the fast motion regime, and as a result, EWVoigtN could not be used for the initial simulation of components. Instead the EasySpin function *chili* was used to simulate the spectra, including two components, and the weighting factors used in the same way as the scaling factors from EWVoigtN.

In this case more initial parameters were required to simulate the spectra. In a similar way to the simulation of the bound component of **R2@C3** (Section 4.1.5), A- and g-values were obtained from literature and used to simulate the spectra. Linewidths were calculated by first simulating the radical spectrum with *garlic*, and then using these values to simulate the two components of the **R4@C1** spectra for each concentration respectively, whilst the diffusion rate parameters were allowed to vary. This ensured that the parameters obtained for the

simulations were sensible, and that the restricted motion effects were not artificially obscured by other parameters varying in the simulation.

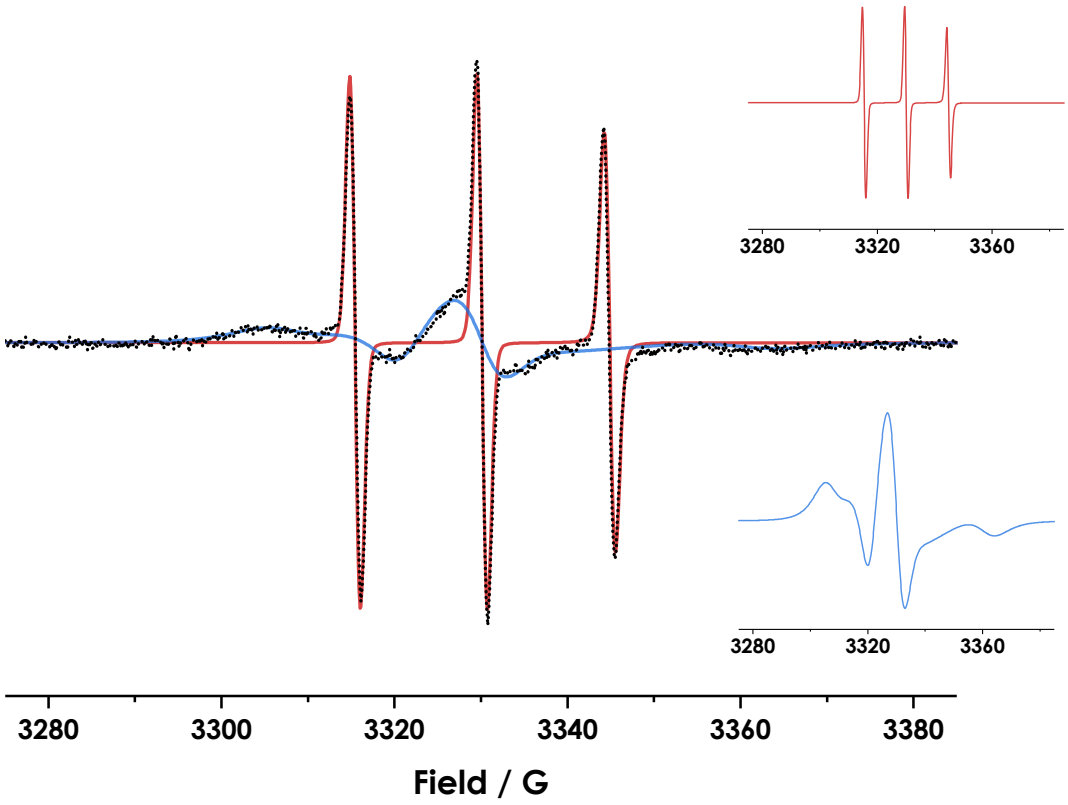

*Figure 74 - EPR spectrum of 2×10^{-5} M 3-carboxy-PROXYL@**C1** in MeCN (black, dotted overlaid with simulated components overlaid (red, unbound component; blue, bound component). The two components are also inset to highlight the difference in lineshape.*

The spectrum for radical at 5×10^{-5} M showed clear evidence of complex spin-spin interactions arising due to the dimerisation of the free carboxylic acid in solution, and therefore was not included in the simulations or subsequent calculations. The spectrum is shown in Figure 75.

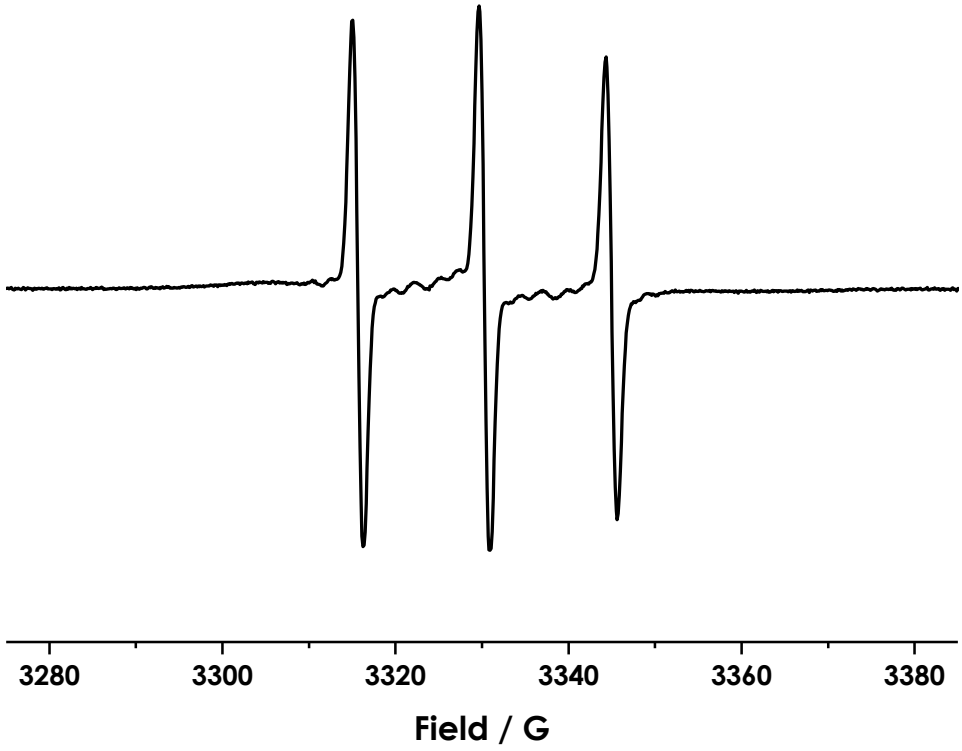

*Figure 75 - EPR spectrum of 5×10^{-5} M 3-carboxy-PROXYL@**C1** in MeCN. The effects of dimerisation of the free carboxylic acid in solution are visible as small peaks in the spectra between the three large nitroxide peaks.*

Ideally, dimerisation effects would have been accounted for in all the simulations, with the weighting of the effect determined by titration investigations of competing guest, **CG2**, allowing a more accurate simulation of the spectra for **R4@C1**. However, due to the complex nature of fitting polyradical spectra with simulations, this was not attempted, as the dimerisation effects with the lower concentrations of radical appeared less significant, and so the spectra could still be fitted with reasonable confidence.

4.3.3 Determination of association constant

Average parameters were then calculated from the remaining concentrations, this time averaging single values for Lorentzian and Gaussian broadening, and either an isotropic diffusion rate parameter for the unbound component, or axial diffusion rate parameters for the bound component. The spectra were resimulated using these fixed parameters, while only the weighting was allowed to vary, to obtain the best fit spectra. These average parameters are shown in Table 6.

*Table 6 - Average parameters for the simulations of **R4@C1** spectra.*

Unbound Component Parameters			
Lorentzian / G	**Gaussian / G**	**log[Diffusion Rate / s^{-1}] (Isotropic)**	
0.32	1.34	9.38	
Bound Component Parameters			
Lorentzian / G	**Gaussian / G**	**log[Diffusion Rate / s^{-1}]**	
		(D_{xy})	**(D_z)**
1.42	2.59	7.12	7.59

Association constant was then calculated for **R4** as before using Equation 3, with the values shown in Table 7.

Table 7 - Simulated scaling factors Bound/Unbound ratio and association constant, K, calculated for each radical concentration.

Guest Conc. / 10^{-5} M	Unbound Guest Scaling / 10^{-1}	Bound Guest Scaling	Bound/Unbound Ratio	K / 10^3 M^{-1}
1.00	1.22	1.00	8.17	**16.31**
2.00	1.85	1.00	5.40	**10.77**
4.00	1.14	1.00	8.79	**17.55**

The average association constant value obtained for **R4** was K = 15±2 $\times 10^3$ M^{-1}. This value is larger than for **R3** (9×10^3 M) suggesting that binding is stronger in this case. As described in Section 4.2.3, comparison to previous guests in the MeCN-soluble cage indicates that binding of this radical is preferred, most likely due to the nature of the interactions with the carboxylic acid group, albeit with the possibility of binding outside the cage. The extra binding strength above that of **R3** is not immediately obvious, but may be due to the slightly smaller, more rigid shape fitting better into the cavity. In this case it is also important to note that the reliability of the value for association constant may be reduced due to only considering three concentrations of radical in the calculations, highlighted by the larger error value. Additionally, the association constant obtained for a guest concentration of 2×10^{-5} M appears to be somewhat anomalous when compared to the other concentrations. This could be indicative of an issue with the sample itself or be due to the simulation parameters used being insufficient to account for all the factors affecting the spectrum reliably (e.g. dimerisation effects). Further investigation was limited by time constraints, and so future work would be needed to ascertain the exact cause of this anomaly, as this again reduces the reliability of the calculated association constant for this radical@cage complex. A greater number of repeated

measurements for each sample and a larger number of radical concentrations investigated would improve the reliability of these calculations.

4.3.4 Molecular motion within the cage

For **R4**, as EasySpin was used from the outset to simulate the EPR spectra, the values required for working out the tumbling rates for each component were already calculated when simulating the initial EPR spectra, and so additional simulation was not required. As with **R4**, there was no Heisenberg exchange effects that needed to be taken into consideration, and so the tumbling rate for the bound radical was calculated as $D_{xy} = 1.33\times10^{6}$ s^{-1} and $D_z = 3.93\times10^{6}$ s^{-1} compared to the isotropic diffusion rate of tumbling for the unbound component of 2.41×10^{9} s^{-1}. These axial rotational diffusion tensors are slower than the tensors calculated for the radicals **R2** and **R3**, suggesting that **R4** is more restricted in its motion when bound than these other radicals. This effect can likely be ascribed to the increased rigidity of the molecule itself, which possesses a 5-membered ring compared to the 6-membered ring structures of the TEMPO derivatives. By again considering the potential binding of the radical to the cage through H-bonding interactions to the carboxylic acid group, (Figure 76) the rotation about D_z ($D_{\parallel}$) would be expected to be faster than that of D_{xy} ($D_{\perp}$), as is observed, and the different geometry of the 5-membered ring structure may explain why D_{xy} appears less restricted than for **R3**. However, it is also possible that the rotation about D_{xy} may be frozen on the EPR timescale, similarly to for **R3**, and that the value is still unreliable.

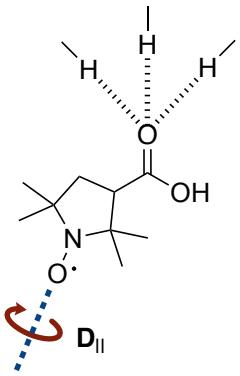

*Figure 76 - Diagram showing how the carboxy group of **R3** may be bound to the cage through H-bonding interactions. The principal diffusion axis, $D_{\parallel}$, and direction of rotation about this axis is shown.*

4.3.5 Conclusions

Simulations of **R4@C1** revealed the two components of the spectra corresponding to unbound and bound radical, with the bound component showing significant evidence of restricted motion, no longer in the fast motion regime, in contrast to **R2** and **R3**. Whilst for the lower

concentrations of **R4@C1** dimerisation appeared to have no significant effect on the binding, at 5×10^{-5} M radical concentration, the dimerisation was such that simulations could not be accurately used to obtain EPR parameters at this concentration, and thus the spectra for this concentration were not used.

This restricted motion was defined quantitatively through rotational diffusion parameters, $D_{xy} = 1.33\times10^{6}$ s^{-1} and $D_z = 3.93x10^{6}$ s^{-1}, obtained from the simulations, for the slow component, compared to 2.41×10^{9} s^{-1} for the unbound component. This larger decrease in tumbling rate than for **R2** and **R3** was ascribed to the increase in radical rigidity going from 6- to 5-membered ring. The association constant was calculated as 15×10^{3} M, although the reliability of this value is lower than that of the previous radicals, due to the potentially anomalous value for the sample at 2×10^{-5} M concentration and the use of fewer samples overall for the calculations. As with **R3**, it is again likely that the radical is bound inside the cage, but with the possibility of being bound to the outside of the cage due to the presence of carboxy group, with the two binding possibilities unable to be distinguished in this work.

5 General conclusions and future work

Previously developed supramolecular self-assembled cage structures of the general form $[M_8L_{12}][X]_{16}$ where M = Cd or Co, L = $C_{28}H_{22}N_6$ and X = ClO_4 or Cl, were investigated with radical guest probes using EPR spectroscopy. The different metal ions and counterions allowed investigation into both MeCN- and H_2O-soluble cages, providing a wider scope of investigation.

Initial studies were carried out with a number of different radical guests comparing radical EPR spectra to radical+cage spectra, and using competing guests to determine whether binding had taken place. Of the initial radicals studied qualitatively, three were chosen for more in-depth studies, 4-oxo-TEMPO (**R2**), 4-carboxy-TEMPO (**R3**) and 3-carboxy-PROXYL (**R4**).

These studies focussed on three main aspects of the EPR spectra that could be used to determine information about the host-guest complexes formed. The first was the ratio of bound to unbound radical guest, obtained by simulating the two components contributing to the EPR spectra of radical@cage, and allowing calculation of association constant for these radicals. The second was the rotational diffusion parameters, obtained again by simulating the spectra, enabling quantification of the restriction of motion of the radical probe upon binding to the cage, as compared to the tumbling motion of the radical in free solution. Finally, the change in hyperfine value between bound and unbound guest was observed and taken to provide an indication of the change in polarity of environment. For this third parameter care was taken not to draw any strong conclusions, as the changes observed were slight, and may in fact have been due to experimental and simulation errors. The possibility of the radicals with carboxylic acids binding outside the cage also meant that definitive conclusions could not be drawn for these complexes.

Comparison of the values obtained for association constants in this work with previous studies of the similar cage structures and their host-guest complexes confirmed that the observations were consistent with the expected binding strength, showing greater affinity than some previous guests due to preferred functional groups, but lesser affinity than others with more favoured geometries. Rotational diffusion parameters were also found generally match well with previous literature of radical@host complexes studied with other supramolecular assemblies, and although some of the values were determined to be unreliable, general conclusions could be drawn with relative confidence.

Further studies with these radicals and cage structures could explore titrating a larger range of concentrations of radical guests. This would ensure greater reliability in calculation of

association constants and provide a method to determine the concentration of radical for which evidence of binding could no longer be determined. The limits of observation of binding could also be investigated by varying the concentration of host cage used with the same concentration of radical guest.

Use of alternative methods to investigate the host-guest complexes formed in this work would also be desirable in future work, to validate the EPR results obtained and provide further insight into the observations. For example, other characterisation techniques may provide the possibility of confirming the binding site of the radicals allowing greater confidence in predicting the factors that could then contribute to binding strength.

Investigations into a wider array of radicals with these cage structures would also be interesting, for example using radical anions to observe the effects of changing pH, allowing effects observed in previous work,[73,78] to be confirmed using the EPR spectroscopic technique.

Future work in this area could also observe how the binding of the radicals inside the cage may afford protection from conditions outside the cage in free solution, for example through the addition of ascorbate in a similar way to the method described by Bardelang et al.[79] during their investigations with cucurbiturils. Since nitroxides are readily reduced by ascorbates, leading to removal of signal in the EPR spectrum, binding inside the cage may prevent this reduction, and a signal in the spectrum would still be observed, allowing study of this potential effect.

6 Experimental

6.1 General Details

6.1.1 Chemicals

All chemicals were used as received from Sigma-Aldrich, TCI, Alfa Aesar, Flurochem, Acros Organics or Fisher Scientific, without further purification.

6.1.2 NMR spectroscopy

^{1}H NMR spectra were recorded at 400 MHz on a JEOL ECS400 spectrometer or at 500 MHz on a Bruker AVIII500HD spectrometer. The deuterated solvent used for each sample was used as an internal standard for ^{1}H NMR. ^{113}Cd NMR spectra were recorded at 110 MHz on the same Bruker spectrometer, and $Cd(ClO_4)_2{\cdot}6H_2O$ was used as an external standard. All chemical shifts reported in parts per million (ppm). Spin multiplicities are represented as follows: s (singlet), d (doublet), t (triplet), m (multiplet).

6.1.3 Mass Spectrometry

Mass spectra were recorded on a Bruker compact™ QqTOF spectrometer in positive ion mode unless stated otherwise.

6.1.4 EPR spectroscopy

EPR spectra were recorded on a Bruker EMXmicro spectrometer, with samples in organic solvents recorded in sealed Pasteur pipettes, and degassed with N_2, whilst samples in water recorded in sealed Marienfeld melting point tubes. Typical parameters were: Power = 5.024 mW; Frequency = 9.32 GHz, Field Modulation Width = 1.0 G.

Experimental EPR spectra were presented without normalisation, and absolute integrals were reported. To ensure comparison between spectra was possible, measurements of samples in the same solvent were recorded in identical EPR cells, and controls showed that absolute integrals were reproducible to within 2.5 %.

EWVoigt software developed by Alex I. Smirnov[54] was used for fast motion nitroxide EPR simulations and EasySpin[49] version 5.2.15 was used in MATLAB R2017b for slow-motion simulations.

6.1.5 UV-Vis spectroscopy

UV-Vis spectra were recorded on a Shimadzu UV-1800 spectrophotometer.

6.2 Synthetic Procedures

6.2.1 1,5-Bis(bromomethyl)naphthalene - **P1**

1,5-Bis(bromomethyl)naphthalene, **P1** was prepared by adapting previously published syntheses. [58,62]

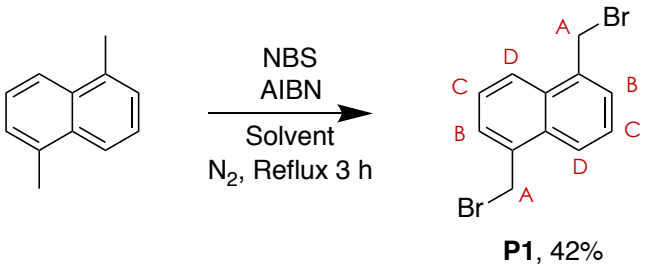

Scheme 7 - Synthesis of 1,5-bis(bromomethyl)naphthalene.

1,5-Dimethylnaphthalene (200.53 mg, 1.28 mmol), N-bromosuccinimide (458.08 mg, 2.57 mmol), AIBN (16.41 mg) and carbon tetrachloride (8 cm^3) were stirred at reflux under N_2 for 3 hrs. The reaction mixture was cooled and filtered and dichloromethane (40 cm^3) was added to the solid residue. The resulting solution was washed with ice cold water (3 × 60 cm^3), dried ($MgSO_4$), and concentrated at reduced pressure. The crude product was sublimed and then recrystallised from hot chloroform (~10 cm^3) to yield the product as white solid (170.24 mg, 0.54 mmol, 42 %). ^1H NMR (400 MHz, $CDCl_3$): δ ppm 4.95 (s, 4H; CH_2 *"A"*), 7.54 (dd, J = 8.4, 7.3 Hz, 2H; CH *"C"*), 7.59 (d, J = 7.3 Hz, 2H; CH *"B"*), 8.19 (d, J = 8.4 Hz, 2H; CH *"D"*).

6.2.2 $C_{28}H_{22}N_6$ - **L1**

L1 was prepared as previously reported by Tidmarsh et al.[55]

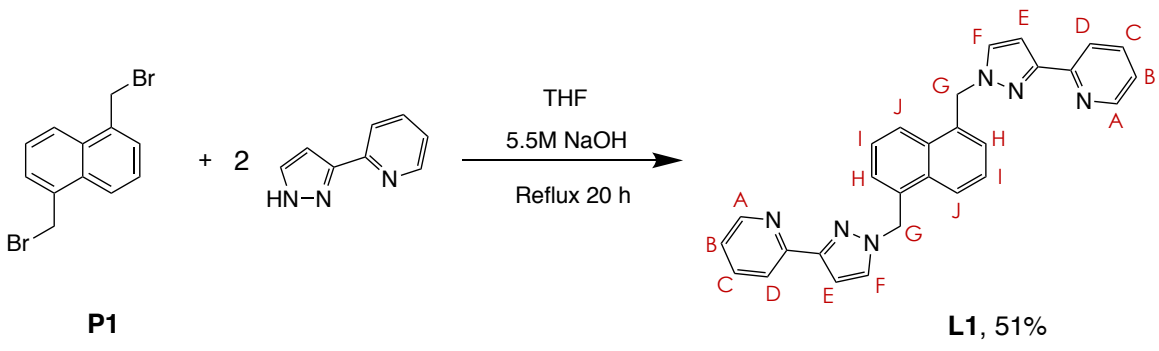

*Scheme 8 - Synthesis of ligand, **L1**.*

To a solution of **P1** (191.29 mg, 0.61 mmol) and 3-(2-pyridyl)pyrazole (186.17 mg, 1.28 mmol) in THF (25 cm^3) was added aqueous NaOH (5.5 M; 2 cm^3). The resulting mixture was heated to reflux for 20 h and then allowed to cool to room temperature. Pure product precipitated from the reaction mixture and was collected by filtration, washed with cold THF, and dried to yield an analytically pure product as an off-white solid (139.35 mg, 0.31 mmol, 51 %). ESI-MS m/z: $(M+2H)^{2+}$calculated for $C_{28}H_{24}N_6$: 222.1026, found: 222.1019; $(M+H)^+$ calculated for $C_{28}H_{23}N_6$: 433.1979, found: 443.1977; $(M+Na)^+$ calculated for $C_{28}H_{22}N_6Na$: 465.1798, found: 465.1792. ^1H NMR (400 MHz, $CDCl_3$): δ 8.64 (ddd, J = 4.9, 1.8, 0.9 Hz, 2H; *"A"*), 8.06 (d, J = 8.5 Hz, 2H; *"H"*), 7.97 (dt, J = 8.0, 1.0 Hz, 2H; *"B"*), 7.72 (td, J = 8.0, 1.8 Hz, 2H; *"C"*), 7.48 (dd, J = 8.5, 7.0 Hz, 2H; *"I"*), 7.34 (d, J = 7.5 Hz, 2H; *"J"*), 7.24 (d, J = 2.4 Hz, 2H; *"F"*), 7.20 (ddd, J = 7.5, 4.9, 1.0 Hz, 2H; *"D"*), 6.84 (d, J = 2.4 Hz, 2H; *"E"*), 5.86 (s, 4H; *"G"*).

6.2.3 $[Cd_8(C_{28}H_{22}N_6)_{12}][ClO_4]_{16}$ - **C1** – (Conventional Method)

C1 was prepared by adapting previously published procedure by Tidmarsh et al.[55]

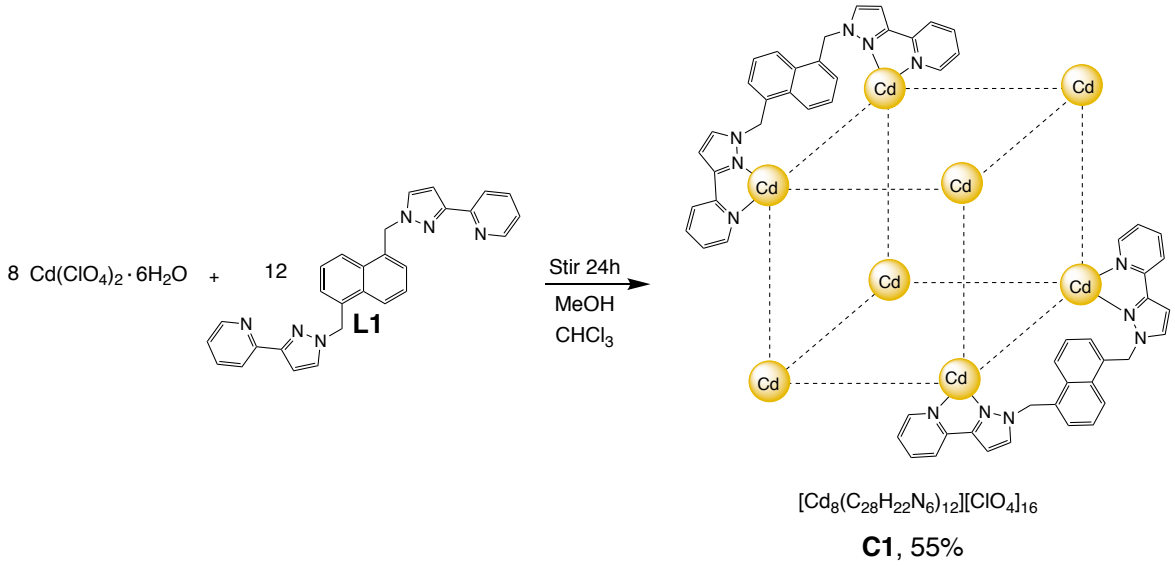

*Scheme 9 - Synthesis of cage **C1** via the conventional method.*

Solutions of $Cd(ClO_4)2{\cdot}6H_2O$ (36.51 mg, 0.0871 mmol) in MeOH (9.5 cm^3) and **(L1)** (60.23 mg, 0.136 mmol) in chloroform (9.5 cm^3) were combined, and the resulting solution was vigorously stirred for 24 h at room temperature. The solvent was removed under reduced pressure, and the crude solid washed with methanol (15 cm^3) and then chloroform (15 cm^3) to remove any unreacted starting materials. The product was dried and obtained as a pale cream solid (46.65 mg, 5.98 x 10^{-3} mmol, 55 %) ESI-MS m/z: 1460.80, $\{[Cd_8(L1)_{12}][ClO_4]_{11}\}^{5+}$; 1200.67, $\{[Cd_8(L1)_{12}][ClO_4]_{10}\}^{6+}$.

6.2.4 $[Co_8(C_{28}H_{22}N_6)_{12}][ClO_4]_{16}$ - **C2** – (Conventional Method)

C2 was prepared by adapting previously published procedure by Tidmarsh et al.[55]

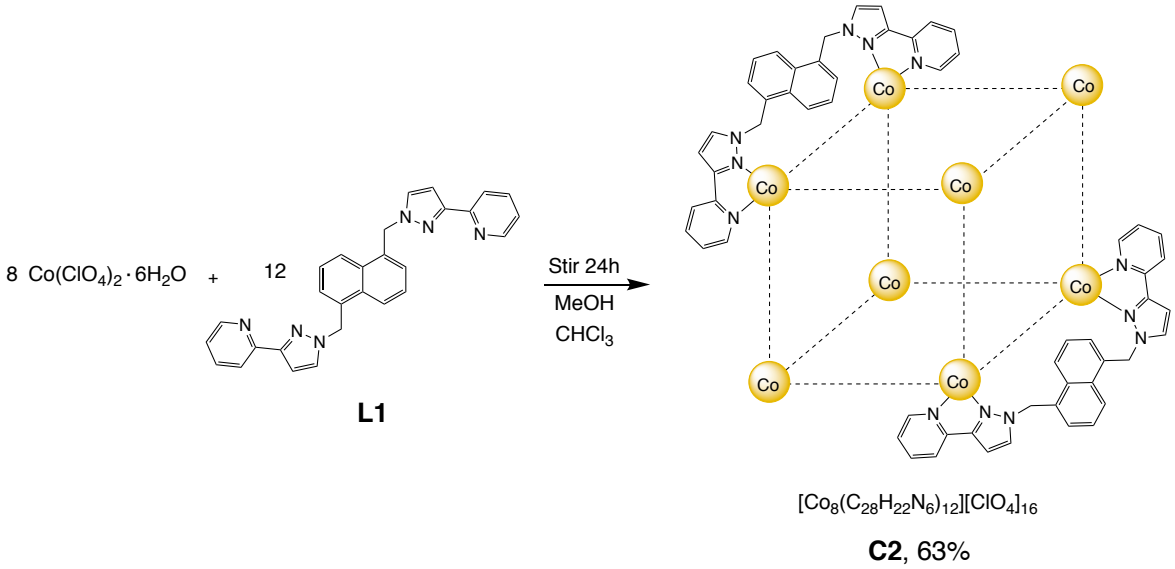

*Scheme 10 - Synthesis of cage **C2** via the conventional method.*

Solutions of $Co(ClO_4)2{\cdot}6H_2O$ (30.59 mg, 0.836 mmol) in MeOH (9.5 cm^3) and **(L1)** (56.97 mg, 0.129 mmol) in chloroform (9.5 cm^3) were combined, and the resulting solution was vigorously stirred for 24 h at room temperature. The solvent was removed under reduced pressure, and the crude solid washed with methanol (15 cm^3) and then chloroform (15 cm^3) to remove any unreacted starting materials. The product was dried and obtained as a pale orange solid (48.43 mg, 6.56 x 10^{-3} mmol, 63 %) ESMS: m/z 1743.77, $\{[Co_8(L1)_{12}][ClO_4]_{12}\}^{4+}$; 1375.03, $\{[Co_8(L1)_{12}][ClO_4]_{11}\}^{5+}$, 1129.20, $\{[Co_8(L1)_{12}][ClO_4]_{10}\}^{6+}$.

6.2.5 $[Co_8(C_{28}H_{22}N_6)_{12}][Cl]_{16}$ – **C3** – Ion Exchange

C3 was prepared from **C2** using an adapted method reported previously.[18]

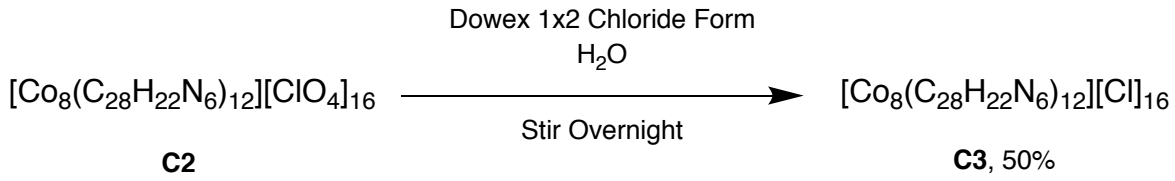

*Scheme 11 – Conversion of **C2** to **C3** using Dowex® resin.*

C2 (19.95 mg, $2.71{\times}10^{-3}$ mmol) and Dowex® 1x2 chloride form, 100-200 mesh (90.75 mg) were added to Millipore H_2O (2 cm^3) and stirred together overnight. The solution was then filtered

through glass wool to remove the Dowex® resin, and the filtrate concentrated under reduced pressure to yield the product as an off-white powder (8.63 mg, 1.36×10^{-3} mmol, 50 %).

6.2.6 Blatter-Type radical - **R8**

Blatter-Type radical (**R8**) was prepared based on procedure reported by Grant et al.[72]

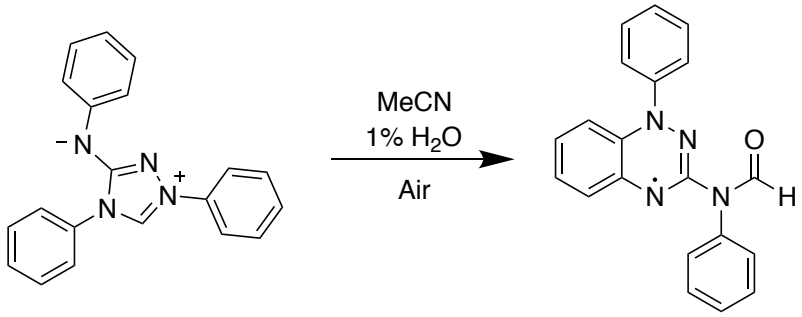

Nitron **R8**, 28%

*Scheme 12 – Synthesis of Blatter-Type radical **R8** from Nitron.*

Nitron (496.64 mg, 1.59 mmol) was added to a solution of MeCN (49.5 cm^3) and 1% H_2O (0.5 cm^3) and stirred for 72 h. The solution was then concentrated under reduced pressure and crude black crystals were obtained. These were purified by column chromatography (98:2 DCM:MeOH) with the product eluted as a dark red fraction, $R_f = 0.49$. This was concentrated under reduced pressure to yield a black solid, which was recrystallised from a minimum amount of hot ethanol to yield Blatter-Type radical (**R8**) as black crystals (145.73 mg, 0.45 mmol, 28 %) ESI-MS m/z: $(M)^+$ calculated for $C_{20}H_{15}N_4O$: 327.1240, found: 327.1240; $(M+Na)^+$ calculated for $C_{20}H_{15}N_4ONa$: 350.1138, found: 350.1139.

6.2.7 Benzyl *tert*-butyl nitroxide (BTBN) – **R6**

Benzyl *tert*-butyl nitroxide was prepared by adapting procedures by Mezzina et al.[31]

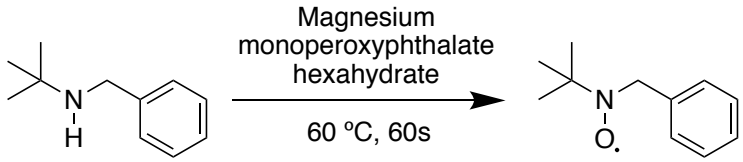

Scheme 13 - Synthesis of benzyl tert-butyl nitroxide, BTBN.

Solutions of benzyl *tert*-butylamine in MeOH (0.2 M) and magnesium monoperoxyphthalate hexahydrate in H_2O (0.2 M) were combined and heated for 60 s at 60°C to form benzyl *tert*-butyl nitroxide *in situ.* EPR (9.33 GHz, H_2O): $a_N = 16.71$ G, $a_H = 10.66$ G, $g_{iso} = 2.0047$.

7 Appendices

7.1 NMR Spectra

7.1.1 1,5-Bis(bromomethyl)naphthalene (**P1**)

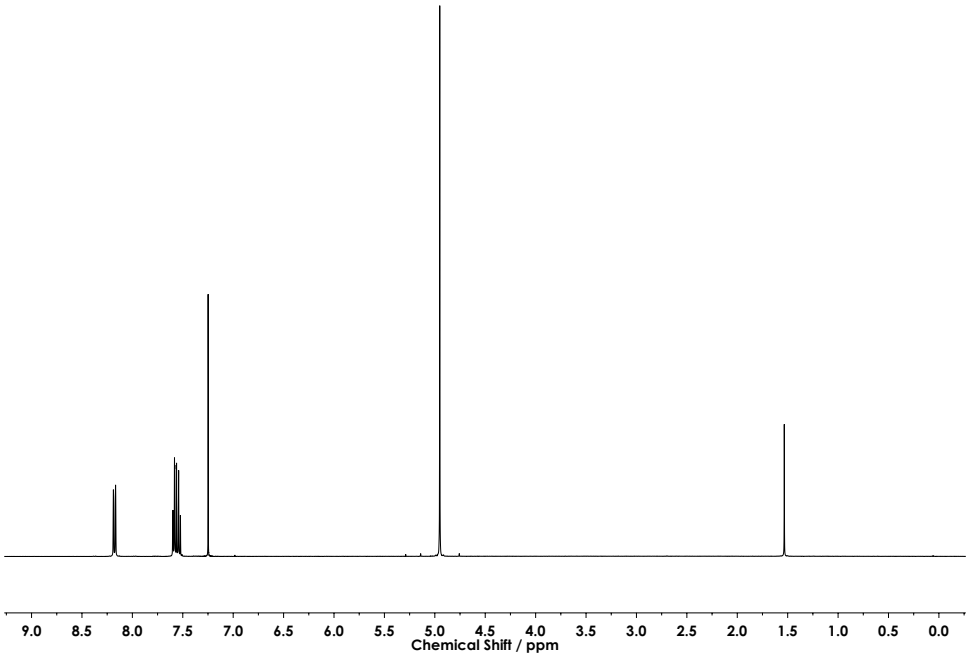

*Figure 77 - ^{1}H NMR ($CDCl_3$, 400 MHz) of 1,5-bis(bromomethyl)naphthalene (**P1**).*

7.1.2 $C_{28}H_{22}N_6$ (**L1**)

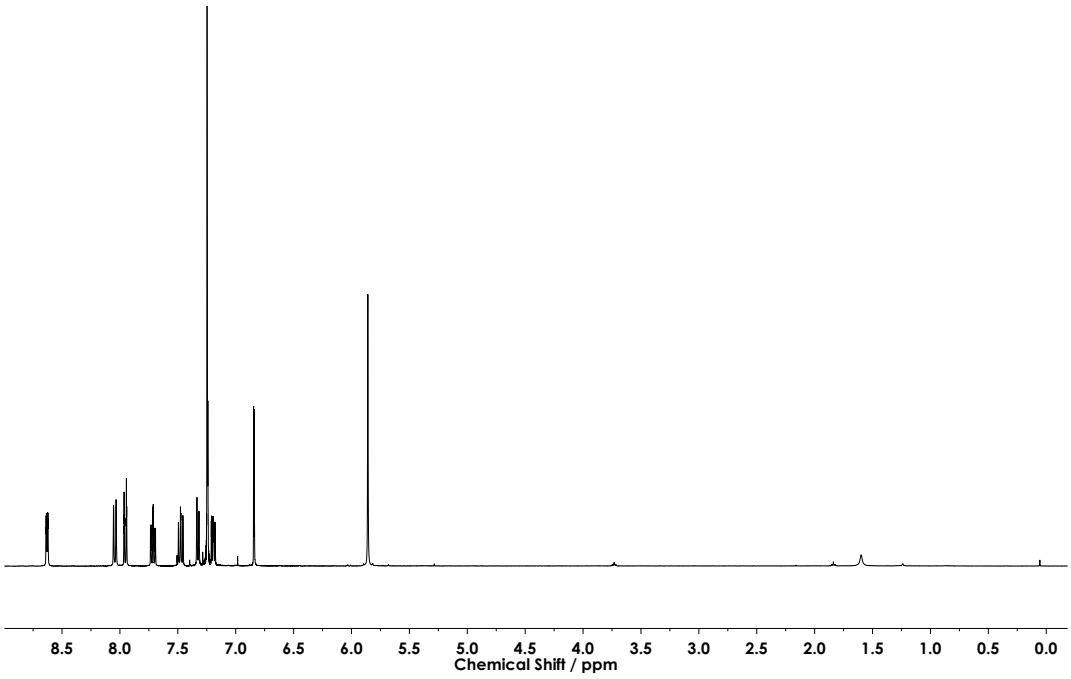

*Figure 78 - ^{1}H NMR ($CDCl_3$, 400 MHz) of **L1**.*

7.1.3 $[Cd_8L_{12}][ClO_4]_{16}$ (**C1**)

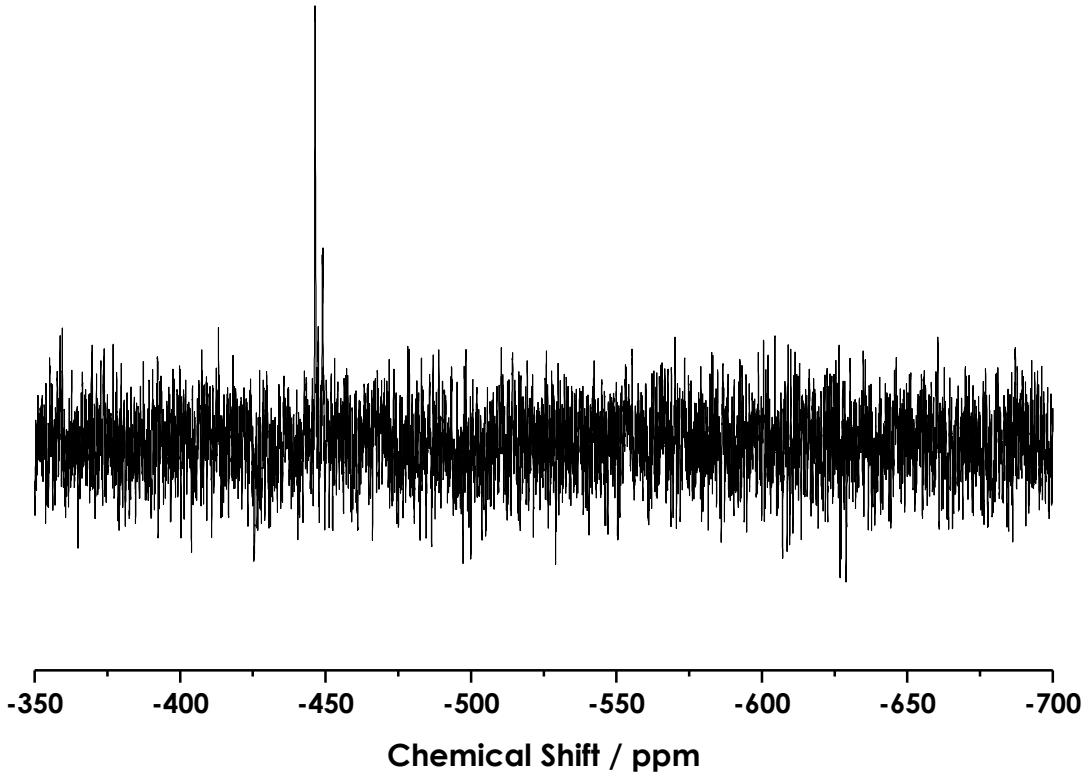

*Figure 79 - ^{113}Cd NMR spectrum of **C1**. The spectrum is noisy, but two peaks may be identified at -446.5 and -449.0 ppm in a 2.32:1 ratio.*

7.1.4 $[Co_8L_{12}][ClO_4]_{16}$ (**C2**)

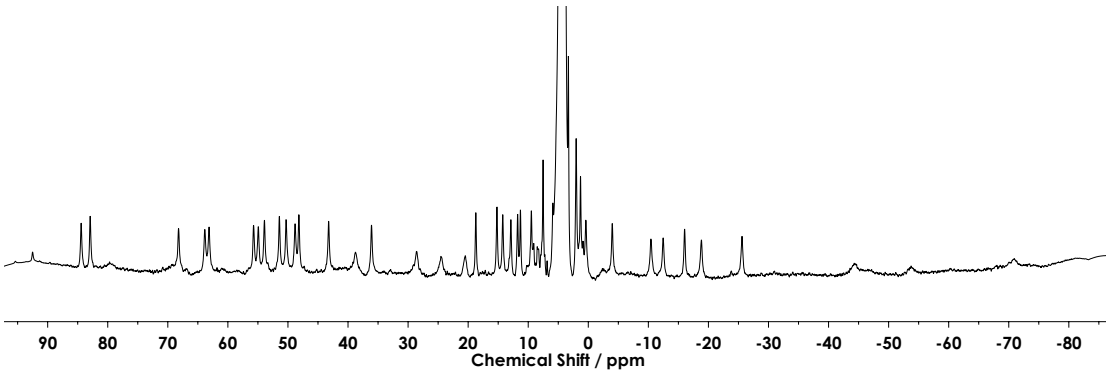

*Figure 80 - ^1H NMR (CD_3NO_2, 400 MHz) of **C2**. The signals are spread over a large range of chemical shifts due to pseudocontact shift effects arising from the presence of the paramagnetic Co^{2+} atoms.*

7.1.5 $[Co_8L_{12}][Cl]_{16}$ (**C3**)

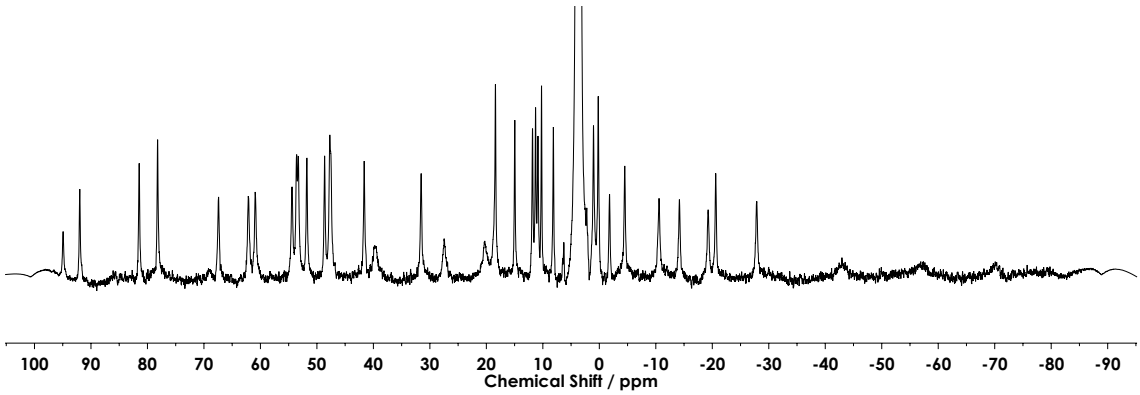

*Figure 81 - ^1H NMR (D_2O, 400 MHz) of **C3**. The signals are spread over a large range of chemical shifts due to pseudocontact shift effects arising from the presence of the paramagnetic Co^{2+} atoms.*

7.1.6 $[Co_8L_{12}][Cl]_{16}$ (**C3**) – Literature Spectrum

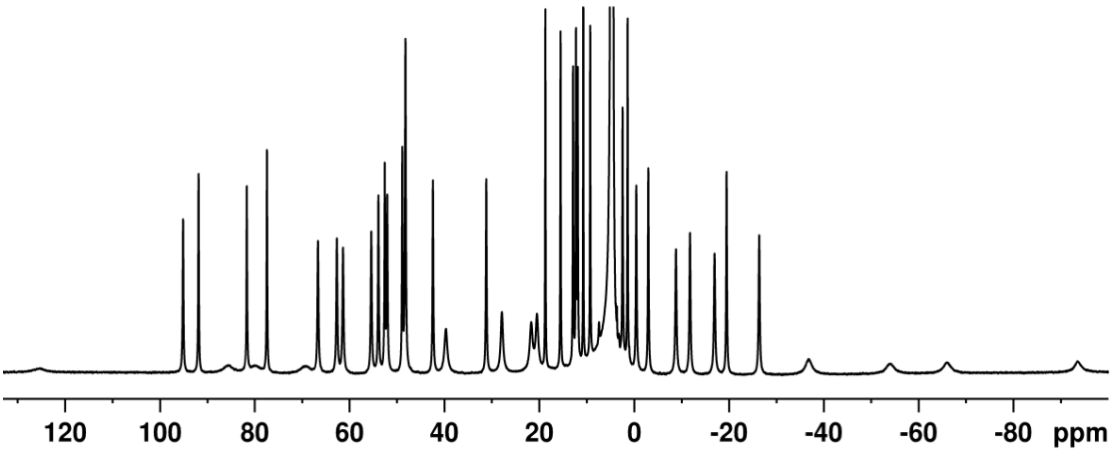

*Figure 82 - ^1H NMR (D_2O, 400 MHz) of **C3**, reported by Cullen et al. after conversion from $[Co_8L_{12}][BF_4]_{16}$. The signals are spread over a large range of chemical shifts due to pseudocontact shift effects arising from the presence of the paramagnetic Co^{2+} atoms. Reproduced from reference.[18]*

7.2 Mass Spectra

7.2.1 $C_{28}H_{22}N_6$ (**L1**)

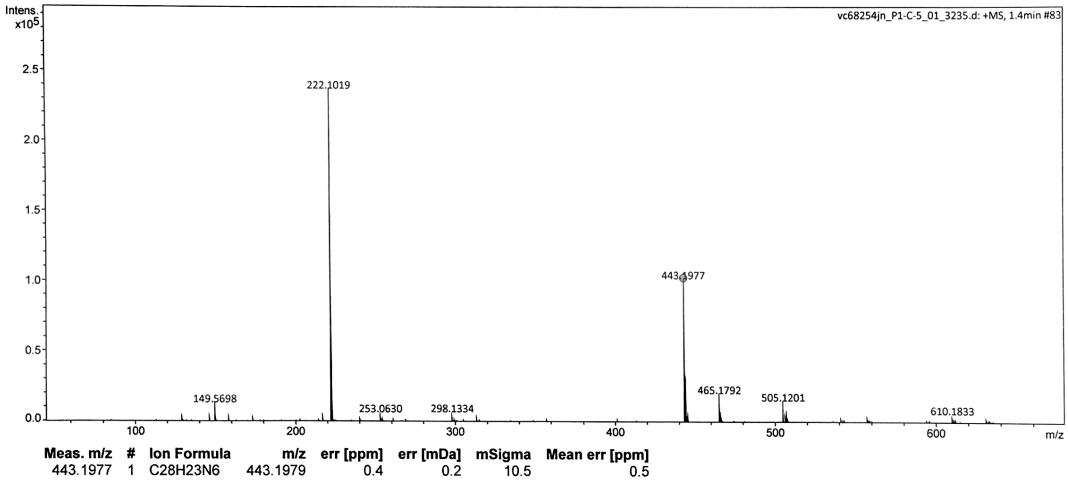

*Figure 83 - Mass spectrum of $C_{28}H_{22}N_6$ (**L1**). $(M+2H)^{2+}$calculated for $C_{28}H_{24}N_6$: 222.1026, found: 222.1019; $(M+H)^+$ calculated for $C_{28}H_{23}N_6$: 433.1979, found: 443.1977; $(M+Na)^+$ calculated for $C_{28}H_{22}N_6Na$: 465.1798, found: 465.1792.*

7.2.2 $[Cd_8L_{12}][ClO_4]_{16}$ (**C1**)

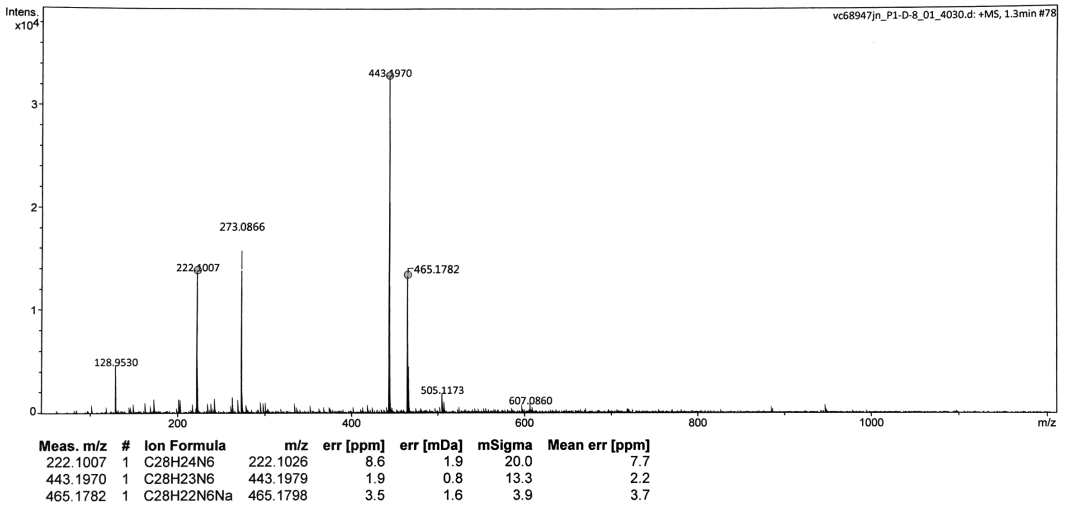

*Figure 84 - Mass spectrum of **C1** – low mass region, m/z 0 – 1200.*

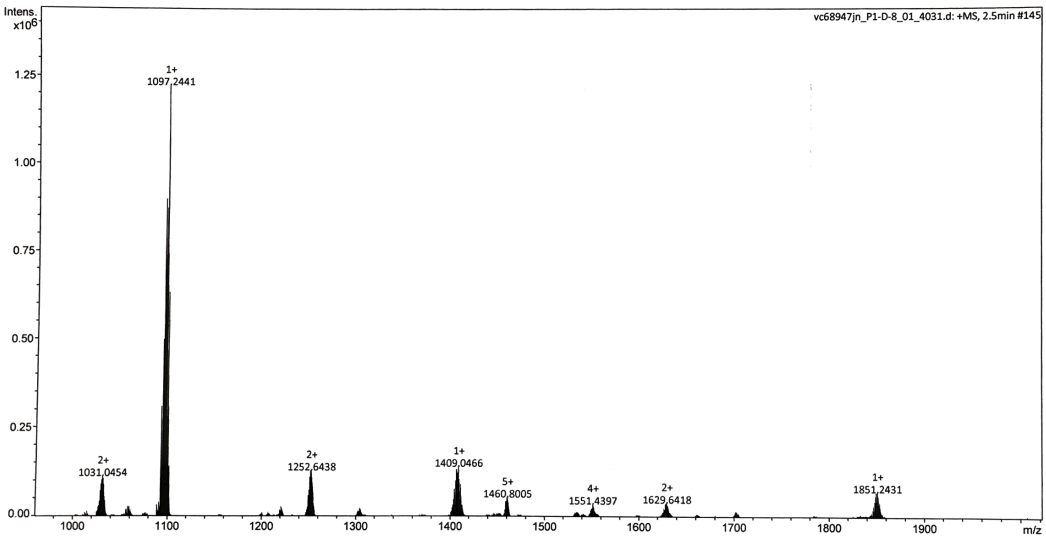

*Figure 85 - Mass spectrum of **C1** – high mass region, m/z 960 – 2020.*

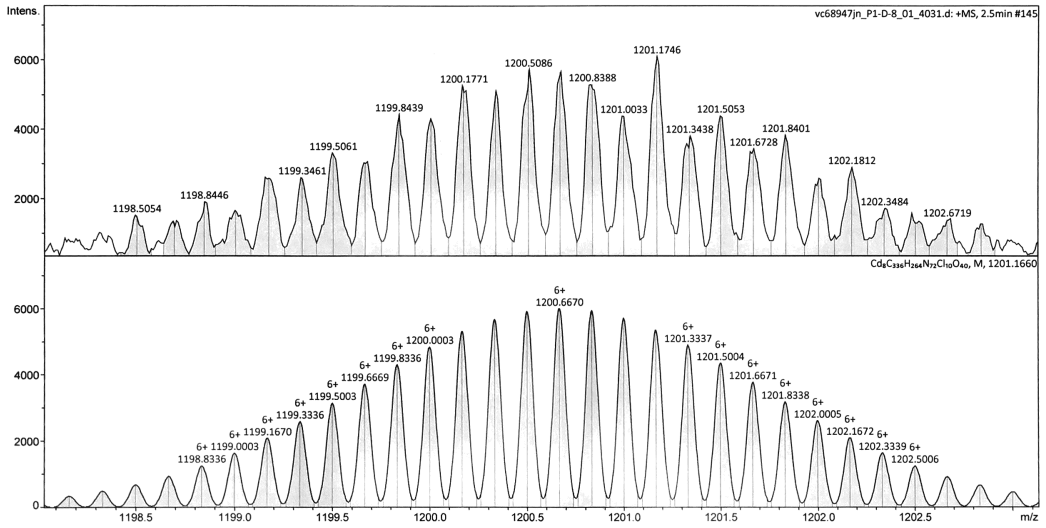

*Figure 86 - Top: Expansion of 6+ peak of experimental mass spectrum of **C1**, corresponding to loss of 6 ClO_4^- ions. Bottom: Predicted 6+ peak for $[Cd_8(L1)_{12}][ClO_4]_{10}^{6+}$*

7.2.3 $[Co_8L_{12}][ClO_4]_{16}$ (**C2**)

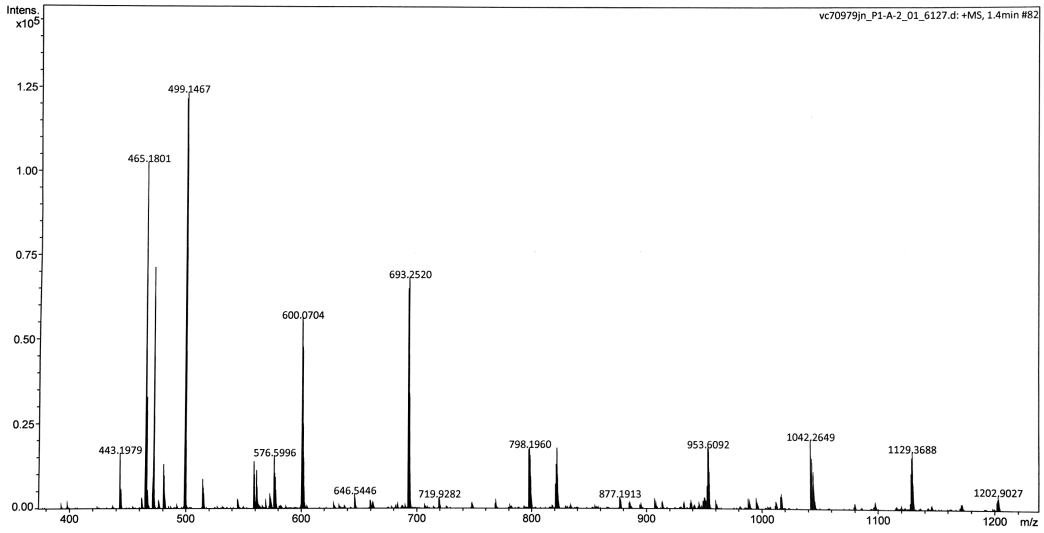

*Figure 87 - Mass spectrum of **C2** – low mass region, m/z 380 – 1240.*

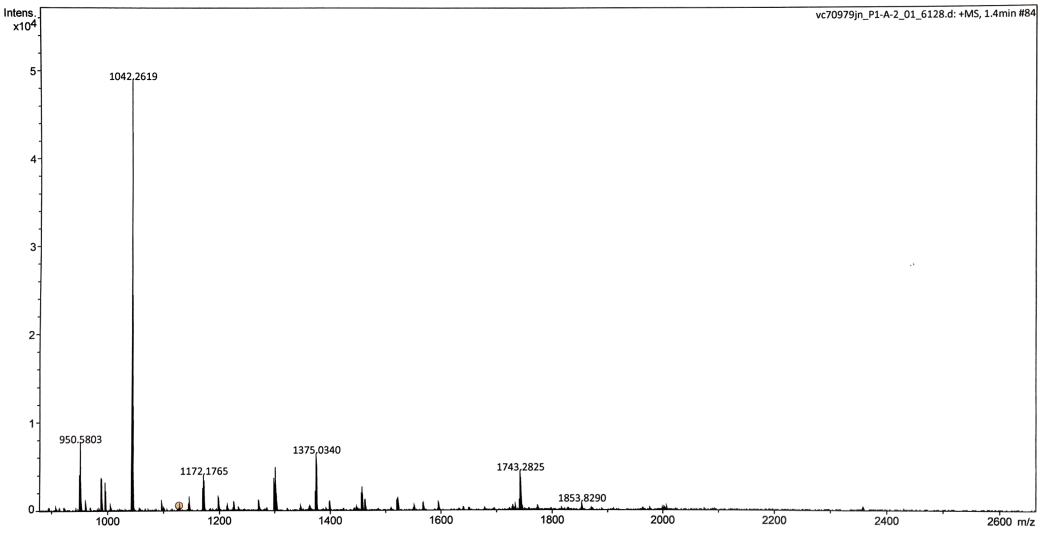

*Figure 88 - Mass spectrum of **C2** – high mass region, m/z 900 – 2600.*

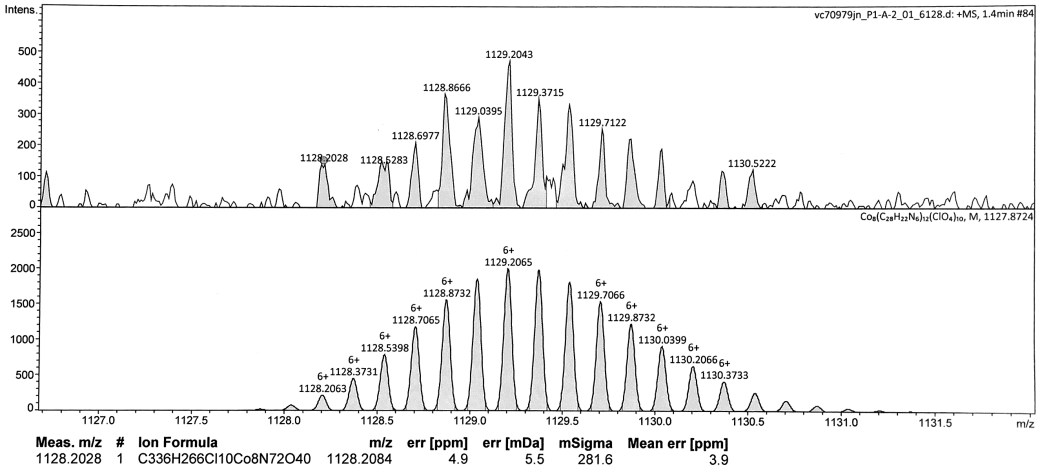

*Figure 89 - Top: Expansion of 6+ peak of experimental mass spectrum of **C2**, corresponding to loss of 6 ClO_4^- ions. Bottom: Predicted 6+ peak for $[Co_8(L1)_{12}][ClO_4]_{10}^{6+}$*

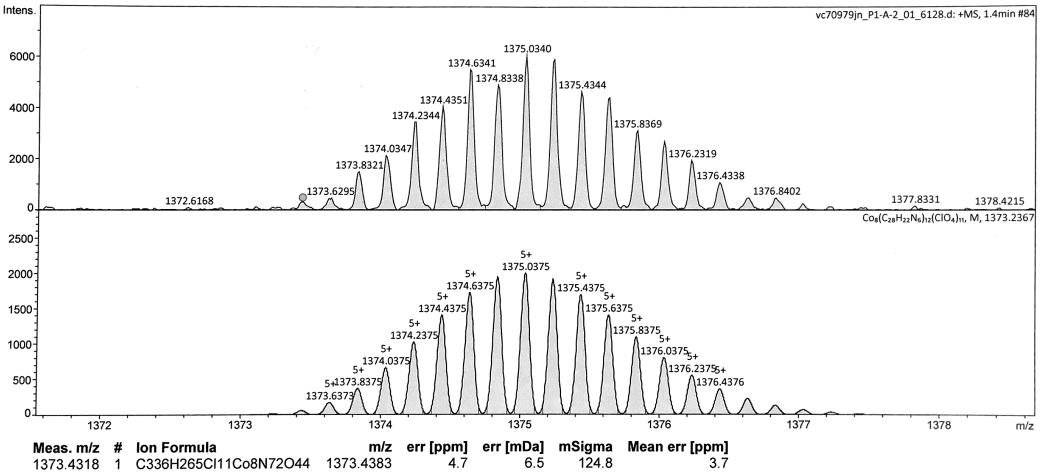

*Figure 90 - Top: Expansion of 5+ peak of experimental mass spectrum of **C2**, corresponding to loss of 5 ClO_4^- ions. Bottom: Predicted 6+ peak for $[Co_8(L1)_{12}][ClO_4]_{11}^{5+}$*

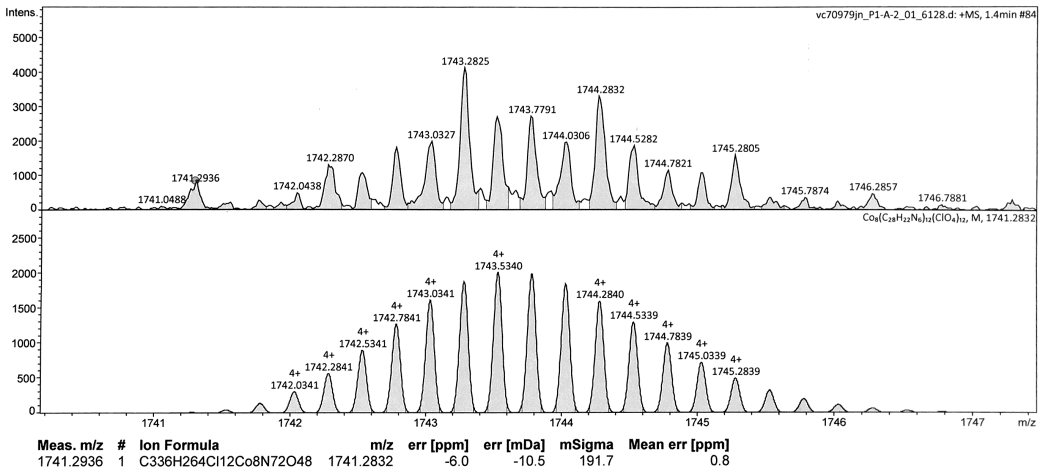

*Figure 91 - Top: Expansion of 4+ peak of experimental mass spectrum of **C2**, corresponding to loss of 4 ClO_4^- ions. Bottom: Predicted 6+ peak for $[Co_8(L1)_{12}][ClO_4]_{12}^{4+}$*

7.3 EPR Spectra

7.3.1 4-oxo-TEMPO (**R2**)

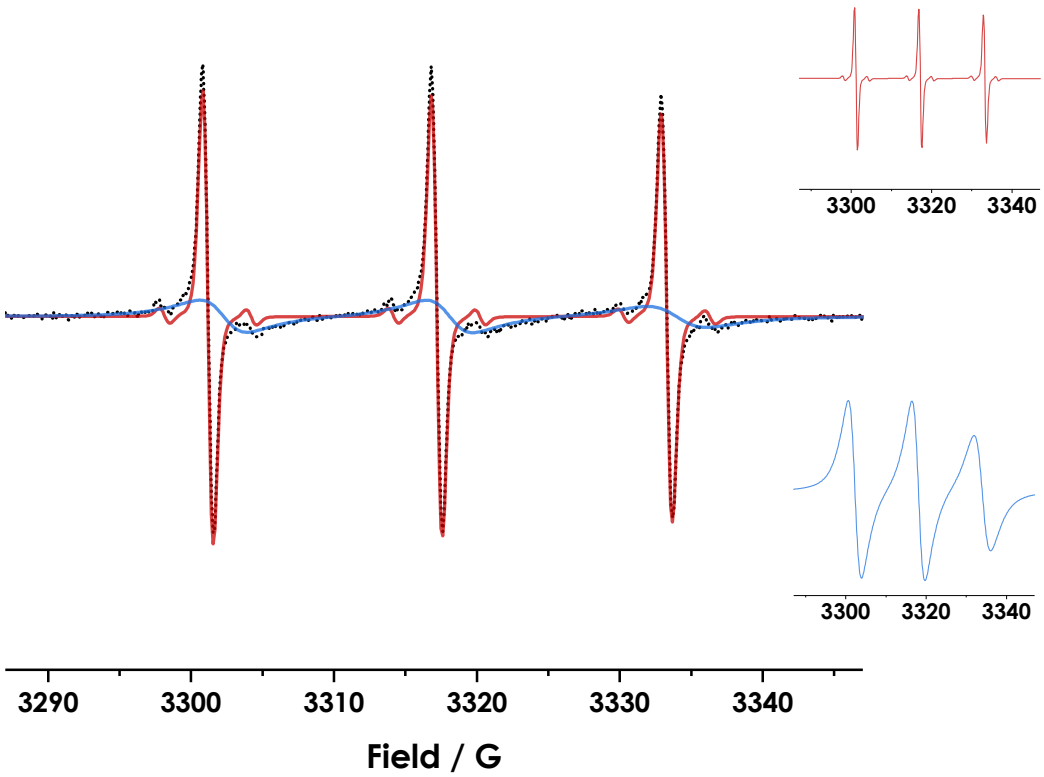

*Figure 92 - EPR spectrum of 1×10^{-5} M 4-oxo-TEMPO@**C3** in H_2O (black, dotted) overlaid with simulated components overlaid (red, unbound component; blue bound component). The two components are also inset to highlight the difference in lineshape.*

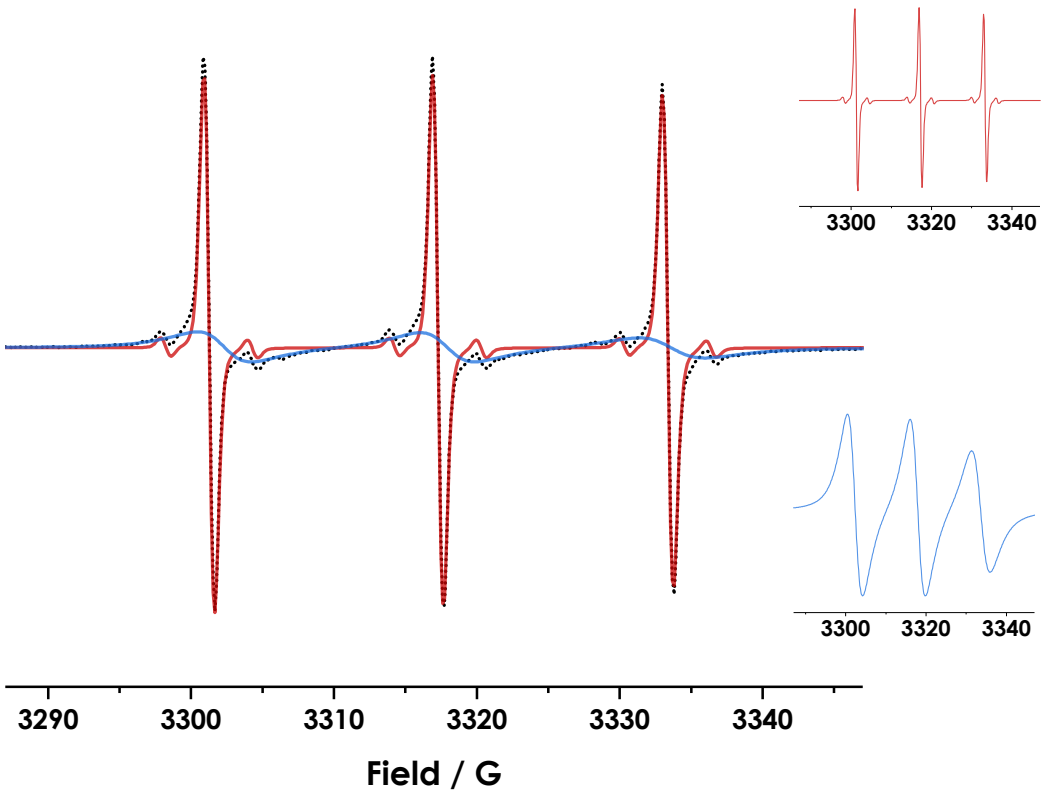

*Figure 93 - EPR spectrum of 4×10^{-5} M 4-oxo-TEMPO@**C3** in H_2O (black, dotted) overlaid with simulated components overlaid (red, unbound component; blue bound component). The two components are also inset to highlight the difference in lineshape.*

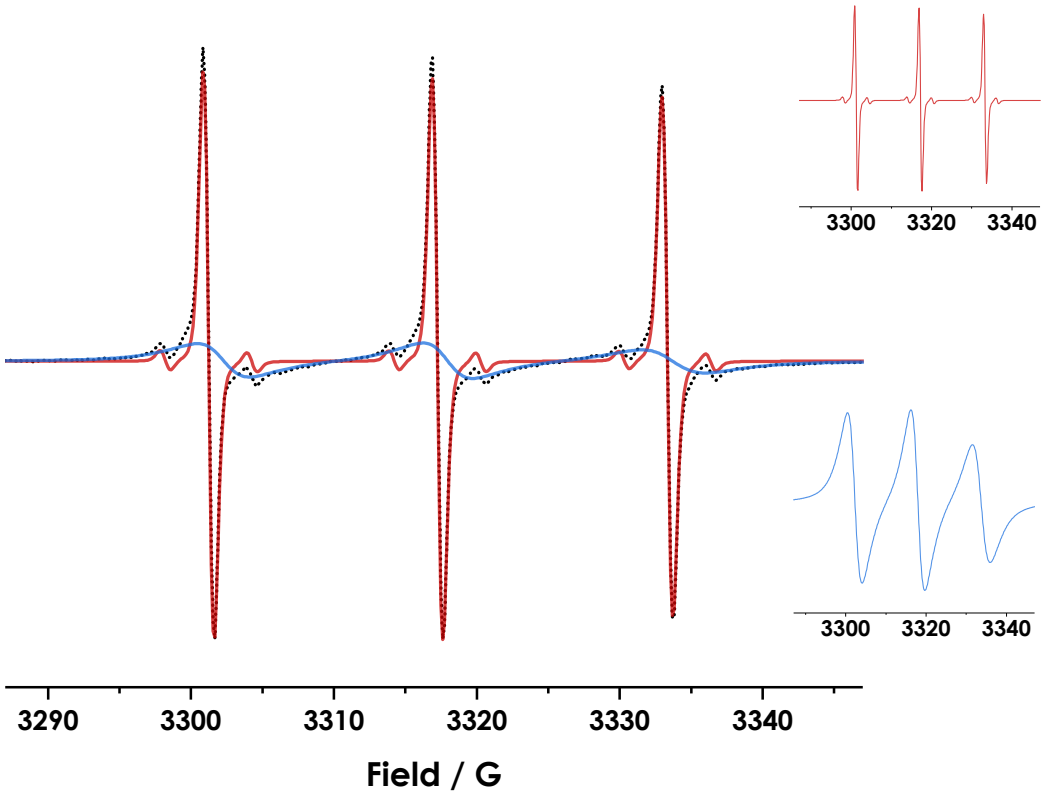

*Figure 94 - EPR spectrum of 5×10^{-5} M 4-oxo-TEMPO@**C3** in H_2O (black, dotted) overlaid with simulated components overlaid (red, unbound component; blue bound component). The two components are also inset to highlight the difference in lineshape.*

7.3.2 4-carboxy-TEMPO (**R3**)

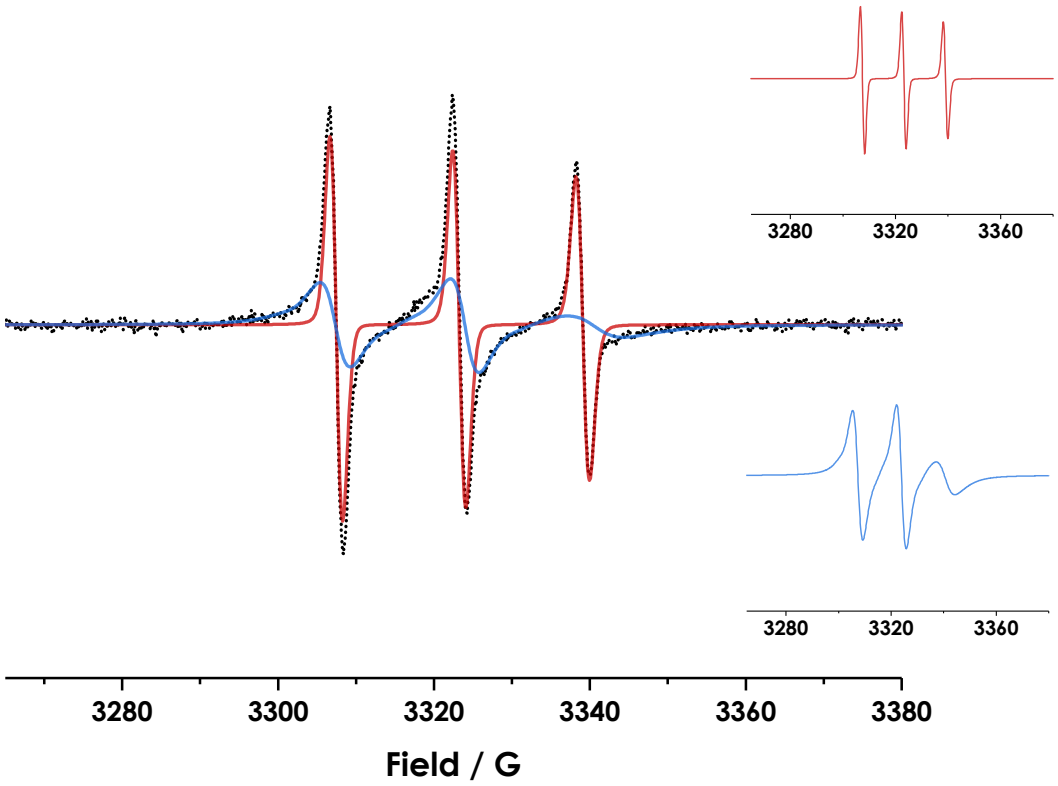

*Figure 95 - EPR spectrum of 1×10^{-5} M 4-carboxy-TEMPO@**C1** in MeCN (black, dotted) overlaid with simulated components overlaid (red, unbound component; blue bound component). The two components are also inset to highlight the difference in lineshape.*

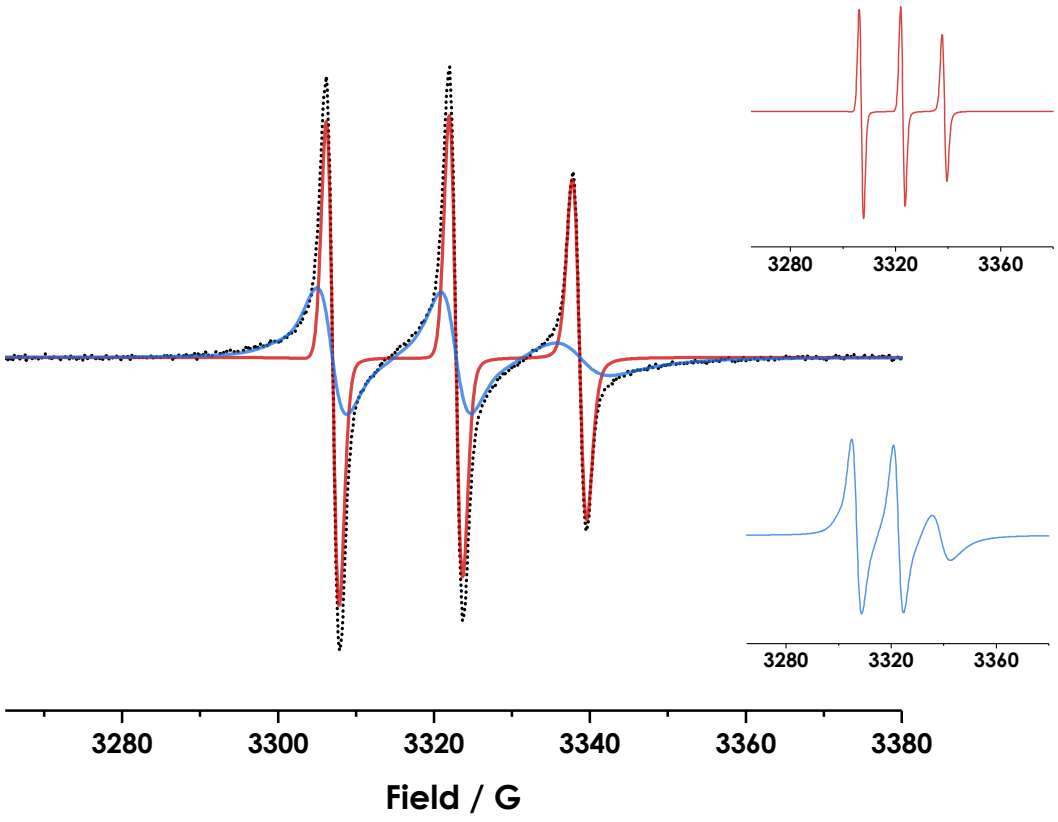

*Figure 96 - EPR spectrum of 4×10^{-5} M 4-carboxy-TEMPO@**C1** in MeCN (black, dotted) overlaid with simulated components overlaid (red, unbound component; blue bound component). The two components are also inset to highlight the difference in lineshape.*

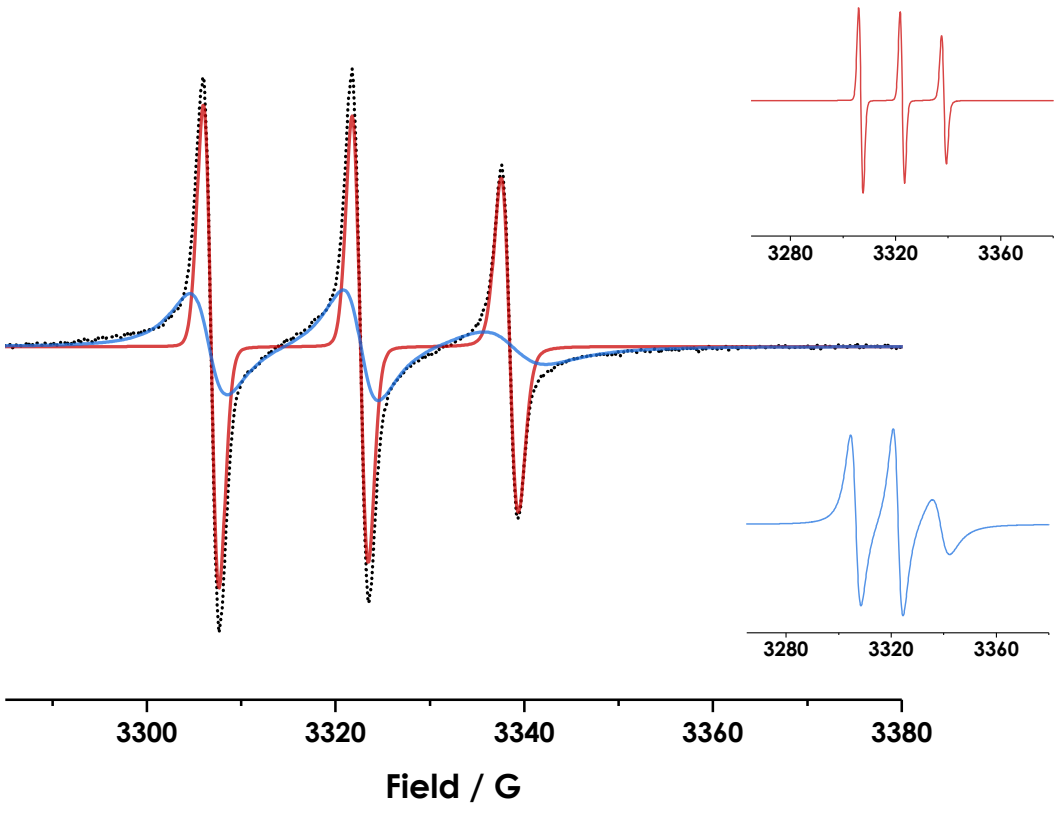

*Figure 97 - EPR spectrum of 5×10^{-5} M 4-carboxy-TEMPO@**C1** in MeCN (black, dotted) overlaid with simulated components overlaid (red, unbound component; blue bound component). The two components are also inset to highlight the difference in lineshape.*

7.3.3 3-carboxy-PROXYL (**R4**)

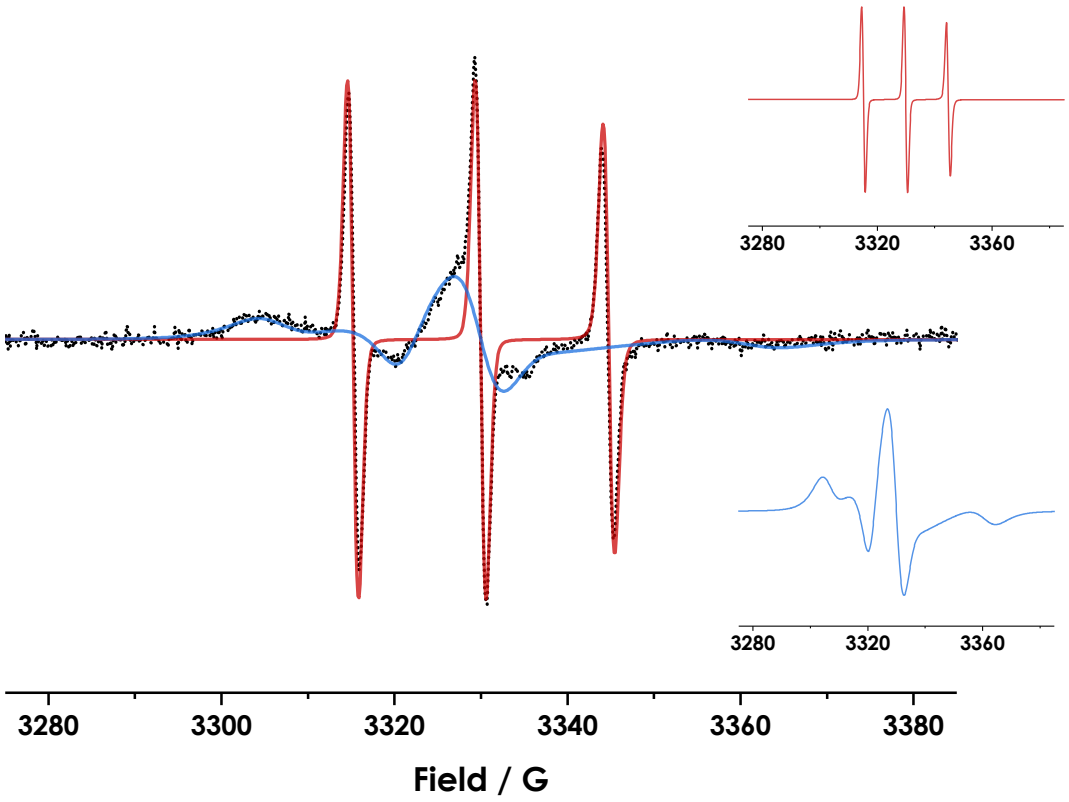

*Figure 98 - EPR spectrum of 1×10^{-5} M 3-carboxy-PROXYL@**C1** in MeCN (black, dotted) overlaid with simulated components overlaid (red, unbound component; blue bound component). The two components are also inset to highlight the difference in lineshape.*

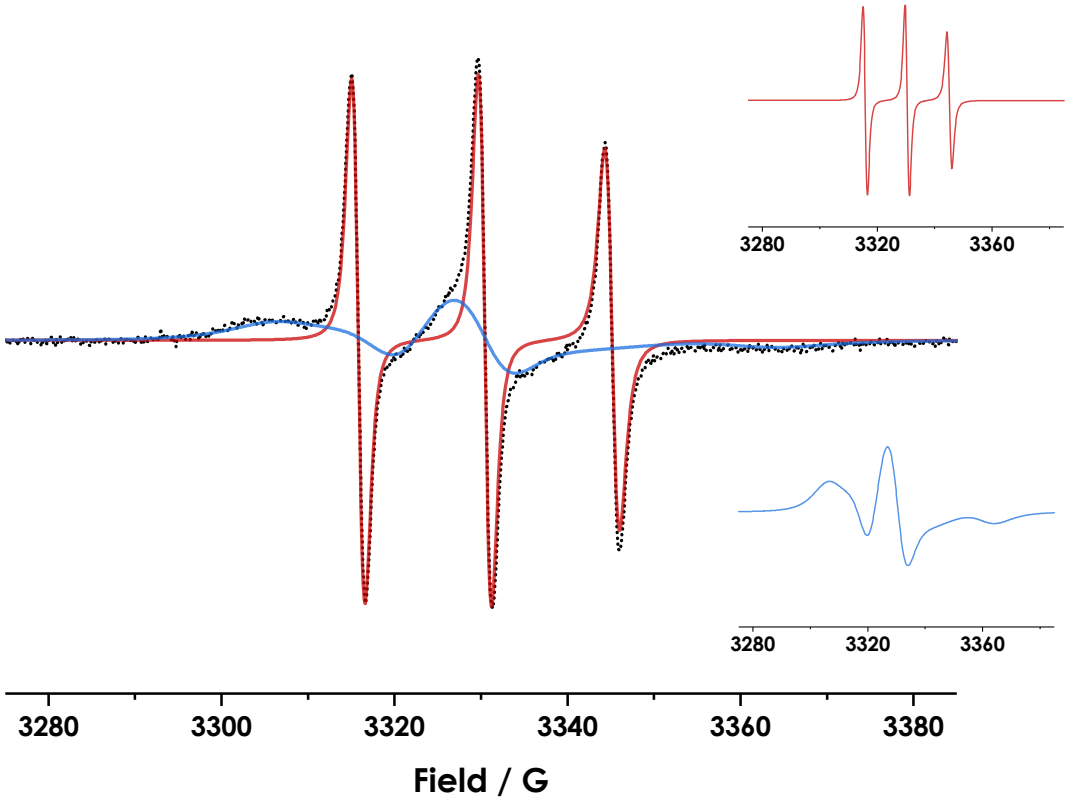

*Figure 99 - EPR spectrum of 4×10^{-5} M 3-carboxy-PROXYL@**C1** in MeCN (black, dotted) overlaid with simulated components overlaid (red, unbound component; blue bound component). The two components are also inset to highlight the difference in lineshape.*

8 References

1 J.-P. Sauvage, presented in part at the Nobel Lectures, Aula Magna, Stockholm University, December, 2016.

2 J.-P. Sauvage, J.-P. Collin, S. Durot, J. Frey, V. Heitz, A. Sour and C. Tock, *C. R. Chim.*, 2010, **13**, 315–328.

3 J. F. Stoddart, presented in part at the Nobel Lectures, Aula Magna, Stockholm University, December, 2016.

4 J. F. Stoddart, *Angew. Chem. Int. Ed.*, 2017, **56**, 11094–11125.

5 B. L. Feringa, presented in part at the Nobel Lectures, Aula Magna, Stockholm University, December, 2016.

6 B. L. Feringa, *J. Org. Chem.*, 2007, **72**, 6635–6652.

7 D. L. Caulder and K. N. Raymond, *Angew. Chem. Int. Ed. Engl.*, 1997, **36**, 1440–1442.

8 D. L. Caulder, C. Brückner, R. E. Powers, S. König, T. N. Parac, J. A. Leary and K. N. Raymond, *J. Am. Chem. Soc.*, 2001, **123**, 8923–8938.

9 S. König, C. Brückner, K. N. Raymond and J. A. Leary, *J. Am. Soc. Mass. Spectrom.*, 1998, **9**, 1099–1103.

10 S. R. Seidel and P. J. Stang, *Acc. Chem. Res.*, 2002, **35**, 972–983.

11 Z. R. Bell, J. A. Mc Cleverty and M. D. Ward, *Aust. J. Chem.*, 2003, **56**, 665–670.

12 J. S. Fleming, K. L. V. Mann, C.-A. Carraz, E. Psillakis, J. C. Jeffery, J. A. McCleverty and M. D. Ward, *Angew. Chem. Int. Ed.*, 1998, **37**, 1279–1281.

13 F. Li, N. F. Sciortino, J. K. Clegg, S. M. Neville and C. J. Kepert, *Aust. J. Chem.*, 2014, **67**, 1625–1628.

14 P. Mal, D. Schultz, K. Beyeh, K. Rissanen and J. R. Nitschke, *Angew. Chem. Int. Ed.*, 2008, **47**, 8297–8301.

15 T. K. Ronson, C. Giri, N. K. Beyeh, A. Minkkinen, F. Topić, J. J. Holstein, K. Rissanen and J. R. Nitschke, *Chem. - Eur. J.*, 2013, **19**, 3374–3382.

16 W. Meng, T. K. Ronson and J. R. Nitschke, *Proc. Natl. Acad. Sci. U. S. A.*, 2013, **110**, 10531–10535.

17 E. G. Percástegui, J. Mosquera and J. R. Nitschke, *Angew. Chem. Int. Ed.*, 2017, **56**, 9136–9140.

18 W. Cullen, A. J. Metherell, A. B. Wragg, C. G. P. Taylor, N. H. Williams and M. D. Ward, *J. Am. Chem. Soc.*, 2018, **140**, 2821–2828.

19 D. Fujita, Y. Ueda, S. Sato, H. Yokoyama, N. Mizuno, T. Kumasaka and M. Fujita, *Chem*, 2016, **1**, 91–101.

20 K. Suzuki, M. Tominaga, M. Kawano and M. Fujita, *Chem. Commun.*, 2009, 1638–1640.

21 M. Tominaga, K. Suzuki, M. Kawano, T. Kusukawa, T. Ozeki, S. Sakamoto, K. Yamaguchi and M. Fujita, *Angew. Chem. Int. Ed.*, 2004, **43**, 5621–5625.

22 Q.-F. Sun, J. Iwasa, D. Ogawa, Y. Ishido, S. Sato, T. Ozeki, Y. Sei, K. Yamaguchi and M. Fujita, *Science*, 2010, **328**, 1144–1147.

23 T. Y. Kim, R. A. S. Vasdev, D. Preston and J. D. Crowley, *Chem. - Eur. J.*, 2018, **24**, 14878–14890.

24 D. L. Caulder, R. E. Powers, T. N. Parac and K. N. Raymond, *Angew. Chem. Int. Ed.*, 1998, **37**, 1840–1843.

25 S. Turega, M. Whitehead, B. R. Hall, M. F. Haddow, C. A. Hunter and M. D. Ward, *Chem. Commun.*, 2012, **48**, 2752.

26 S. Turega, M. Whitehead, B. R. Hall, A. J. H. M. Meijer, C. A. Hunter and M. D. Ward, *Inorg. Chem.*, 2013, **52**, 1122–1132.

27 M. D. Ward, C. A. Hunter and N. H. Williams, *Chem. Lett.*, 2016, **46**, 2–9.

28 W. Cullen, M. C. Misuraca, C. A. Hunter, N. H. Williams and M. D. Ward, *Nat. Chem.*, 2016, **8**, 231–236.

29 P. Mal, B. Breiner, K. Rissanen and J. R. Nitschke, *Science*, 2009, **324**, 1697–1699.

30 M. M. J. Smulders and J. R. Nitschke, *Chem. Sci.*, 2012, **3**, 785–788.

31 E. Mezzina, F. Cruciani, G. F. Pedulli and M. Lucarini, *Chem. - Eur. J.*, 2007, **13**, 7223–7233.

32 G. Ionita, A. Caragheorgheopol, H. Caldararu, L. Jones and V. Chechik, *Org. Biomol. Chem.*, 2009, **7**, 598–602.

33 G. Ionita and V. Chechik, *Phys. Chem. Chem. Phys.*, 2010, **12**, 6956–6960.

34 Y. Kotake and E. G. Janzen, *J. Am. Chem. Soc.*, 1989, **111**, 7319–7323.

35 Y. Kotake and E. G. Janzen, *J. Am. Chem. Soc.*, 1992, **114**, 2872–2874.

36 M. M. Ayhan, G. Casano, H. Karoui, A. Rockenbauer, V. Monnier, M. Hardy, P. Tordo, D. Bardelang and O. Ouari, *Chem. - Eur. J.*, 2015, **21**, 16404–16410.

37 K.-D. Zhang, D. Ajami and J. Rebek, *J. Am. Chem. Soc.*, 2013, **135**, 18064–18066.

38 L. Garel, H. Vezin, J.-P. Dutasta and A. Collet, *Chem. Commun.*, 1996, 719–720.

39 M. Lucarini, B. Luppi, G. F. Pedulli and B. P. Roberts, *Chem. - Eur. J.*, 1999, **5**, 2048–2054.

40 K. Nakabayashi, M. Kawano, M. Yoshizawa, S.-I. Ohkoshi and M. Fujita, *J. Am. Chem. Soc.*, 2004, **126**, 16694–16695.

41 K. Nakabayashi, M. Kawano, T. Kato, K. Furukawa, S.-I. Ohkoshi, T. Hozumi and M. Fujita, *Chem. - Asian J.*, 2007, **2**, 164–170.

42 E. G. Janzen, G. A. Coulter, U. M. Oehler and J. P. Bergsma, *Can. J. Chem.*, 1982, **60**, 2725–2733.

43 E. G. Janzen and G. A. Coulter, *Tetrahedron Lett.*, 1981, **22**, 615–618.

44 M. J. F. Fernandez and H. Sato, *Theor. Chem. Acc.*, 2011, **130**, 299–304.

45 P. Mukerjee, C. Ramachandran and R. A. Pyter, *J. Phys. Chem.*, 1982, **86**, 3189–3197.

46 R. Improta and V. Barone, *Chem. Rev.*, 2004, **104**, 1231–1254.

47 C. P. Poole and H. A. Farach, *Bull. Magn. Reson.*, 1979, **1**, 162–194.

48 S. Stoll and A. Schweiger, in *ESR Spectroscopy in Membrane Biophysics*, eds. M. A. Hemminga and L. J. Berliner, Springer US, Boston, MA, 2007, vol. 27, pp. 299–321.

49 S. Stoll and A. Schweiger, *J. Magn. Reson.*, 2006, **178**, 42–55.

50 A. G. Redfield, in *Advances in Magnetic and Optical Resonance*, ed. J. S. Waugh, Academic Press, 1965, vol. 1, pp. 1–32.

51 G. Gescheidt, in *Electron Paramagnetic Resonance*, eds. M. Brustolon and E. Giamello, John Wiley & Sons, Inc., Hoboken, NJ, USA, 2009, pp. 109–158.

52 D. Gamliel and H. Levanon, *Stochastic Processes in Magnetic Resonance*, World Scientific, 1995.

53 D. J. Schneider and J. H. Freed, in *Spin Labeling: Theory and Applications*, eds. L. J. Berliner and J. Reuben, Springer US, Boston, MA, 1989, pp. 1–76.

54 T. I. Smirnova and A. I. Smirnov, in *ESR Spectroscopy in Membrane Biophysics*, eds. M. A. Hemminga and L. J. Berliner, Springer US, Boston, MA, 2007, vol. 27, pp. 165–251.

55 I. S. Tidmarsh, T. B. Faust, H. Adams, L. P. Harding, L. Russo, W. Clegg and M. D. Ward, *J. Am. Chem. Soc.*, 2008, **130**, 15167–15175.

56 S. Mecozzi and J. Rebek Jr, *Chem. - Eur. J.*, 1998, **4**, 1016–1022.

57 M. R. Ams, D. Ajami, S. L. Craig, J.-S. Yang and J. Rebek Jr, *J. Am. Chem. Soc.*, 2009, **131**, 13190–13191.

58 R. H. Fleming, F. H. Quina and G. S. Hammond, *J. Am. Chem. Soc.*, 1974, **96**, 7738–7741.

59 G. Koshkakaryan, D. Cao, L. M. Klivansky, S. J. Teat, J. L. Tran and Y. Liu, *Org. Lett.*, 2010, **12**, 1528–1531.

60 H. S. Brown, C. P. Muenchausen and L. R. Sousa, *J. Org. Chem.*, 1980, **45**, 1682–1686.

61 P. G. Jones and P. Kuś, *Z. Naturforsch., B: J. Chem. Sci.*, 2014, **65**, 433–444.

62 T. Higashi, K. Uemura, K. Inami and M. Mochizuki, *Bioorg. Med. Chem.*, 2009, **17**, 3568–3571.

63 H. Shimojo, K. Moriyama and H. Togo, *Synthesis*, 2015, **47**, 1280–1290.

64 A. Stephenson, PhD Thesis, University of Sheffield, 2012.

65 M. D. Ward, *Chem. Commun.*, 2009, 4487–4499.

66 M. Whitehead, S. Turega, A. Stephenson, C. A. Hunter and M. D. Ward, *Chem. Sci.*, 2013, **4**, 2744–2751.

67 C. G. P. Taylor, W. Cullen, O. M. Collier and M. D. Ward, *Chem. - Eur. J.*, 2017, **23**, 206–213.

68 J. H. Freed, *J. Phys. Chem.*, 1967, **71**, 38–51.

69 J. H. Marshall, *J. Chem. Phys.*, 1971, **54**, 2762–2763.

70 R. G. Kooser, *Macromolecules*, 1987, **20**, 435–436.

71 P. Franchi, G. F. Pedulli and M. Lucarini, *J. Phys. Chem. A*, 2008, **112**, 8706–8714.

72 J. A. Grant, Z. Lu, D. E. Tucker, B. M. Hockin, D. S. Yufit, M. A. Fox, R. Kataky, V. Chechik and A. C. O'Donoghue, *Nat. Commun.*, 2017, **8**, 15088.

73 W. Cullen, S. Turega, C. A. Hunter and M. D. Ward, *Chem. Sci.*, 2015, **6**, 625–631.

74 R. Owenius, M. Engström, M. Lindgren and M. Huber, *J. Phys. Chem. A*, 2001, **105**, 10967–10977.

75 I. Al-bala'a and R. D. Bates, *J. Magn. Reson.*, 1987, **73**, 78–89.

76 M. Azarkh and E. J. J. Groenen, *J. Phys. Chem. B*, 2015, **119**, 13416–13421.

77 E. Mileo, S. Yi, P. Bhattacharya and A. E. Kaifer, *Angew. Chem. Int. Ed.*, 2009, **48**, 5337–5340.

78 W. Cullen, K. A. Thomas, C. A. Hunter and M. D. Ward, *Chem. Sci.*, 2015, **6**, 4025–4028.

79 D. Bardelang, K. Banaszak, H. Karoui, A. Rockenbauer, M. Waite, K. Udachin, J. A. Ripmeester, C. I. Ratcliffe, O. Ouari and P. Tordo, *J. Am. Chem. Soc.*, 2009, **131**, 5402–5404.